Quantifying the effect of helical cell shape on *Helicobacter pylori's* motility and niche acquisition

Laura Elizabeth Martínez

A dissertation
submitted in partial fulfillment of the
requirements for the degree of

Doctor of Philosophy

University of Washington
2016

Reading Committee:
Nina R. Salama, Chair
David Sherman
Sheila A. Lukehart

Program Authorized to Offer Degree:
Pathobiology

University of Washington

Abstract

Quantifying the effect of helical cell shape on *Helicobacter pylori's* motility and niche acquisition

Laura Elizabeth Martínez

Chair of the Supervisory Committee:

Professor Nina R. Salama, Ph.D.

Interdisciplinary Graduate Program in Pathobiology, University of Washington

Division of Human Biology, Fred Hutchinson Cancer Research Center

Half of all humans harbor the extracellular pathogen *Helicobacter pylori* in their stomachs. Successful colonization by *H. pylori* requires flagellar-based motility for the bacterium to traverse the thick gastric mucus layer and reach its preferred niche, close to the gastric epithelium. Helical cell shape is thought to facilitate *H. pylori*'s ability to bore into the mucus layer in a corkscrew-like motion, thus enhancing colonization of the stomach. In a mouse model of infection, *H. pylori* cell shape mutants show impaired stomach colonization highlighting the importance of cell shape in infection and motility. To investigate how cell shape impacts *H. pylori's* motility *in vitro*, I modeled the viscous environment of the human gastric mucosa with physiologic concentrations of purified porcine gastric mucin (PGM). Using single-cell microscopic tracking and quantitative morphology analysis, I document marked variation in both cell body helical parameters and flagellum number among *H. pylori* strains leading to distinct and broad swimming speed distributions that reflect both temporal variation in swimming speed and morphologic variation within the population. Isogenic mutants with straight rod morphology showed reduced swimming speeds (7-21%) and a higher fraction of immobilized bacteria. Mutational perturbation of flagellum number revealed a 19% increase in swimming speed for *H. pylori* with 4 vs. 3 median flagellum number. Resistive force theory (RFT)-modeling incorporating both cell morphology and flagellum number variation predicts quantitative speed differences of 10-30% among strains. However, quantitative comparisons suggest RFT underestimates the effect of helical shape on speed.

To gain a deeper understanding of how helical cell morphology promotes host colonization by *H. pylori*, I then performed a time course of single-strain infections with wild-type bacteria, a curved rod mutant (Δ*csd1*), and a straight rod mutant (Δ*csd6*). Cell shape mutants show significant attenuation during initial colonization (1 day and 1 week). After persistent infection (1-4 months), a subset of mice infected with Δ*csd1 or* Δ*csd6* mutant bacteria show enhanced infection, while others maintain low or no infection. I used confocal microscopy and 3-D reconstructions of thick tissue sections, and performed volumetric analysis to quantify the number of bacteria within different regions of the stomach. Localization of *H. pylori* reveals multiple gastric niches and specific deficits for cell shape mutants in colonization of the antral glands early after infection, and altered progression of inflammation and gland hyperplasia after chronic infection.

Our studies are elucidating the mechanisms by which helical cell morphology promotes motility and sustains host colonization by *H. pylori*, which may impact human health and disease.

Portions of this dissertation were adapted from the following publication:

Molecular Microbiology, Vol. 99, No. 1, Jan. 2016, p. 88-110.

Table of Contents

Chapter 2: The helical cell shape of *H. pylori* promotes robust motility in viscous environments

Chapter 3: *H. pylori* varies flagellum number to maintain robust motility in viscous environments

Chapter 4: Implementation of a mathematical model to probe the contribution of both morphology and flagellar number variation on speed

Chapter 5: Visualization of *H. pylori* during initial colonization reveals multiple gastric niches and specific deficits for cell shape mutants

List of Figures

List of Tables

List of Videos

ACKNOWLEDGEMENTS I

I am very fortunate to have had Nina Salama as my mentor and advisor. "Nina, I greatly appreciate your support, patience, and guidance over the years. I have great admiration and respect for your brilliance, hard work, and dedication. Thank you for helping me find my voice and helping me grow as a scientist".

I am very thankful to members of my doctoral committee David Sherman, Sheila A. Lukehart, Jessica Hamerman, and Arturo Centurion-Lara who have provided essential advice and guidance during the course of my dissertation research.

Biophysicists Joseph Hardcastle and Dr. Rama Bansil at Boston University have been instrumental to the development and implementation of my research studies on the effect of helical cell shape on *Helicobacter pylori's* motility in different viscous environments. They provided a rich learning environment during my dissertation work.

The Pathobiology Graduate Program and its administrators Mary Conrad, Rachel Reichert, and Ashley Zigler have provided essential support. I would like to acknowledge Dr. Lee Ann Campbell, our program director, for her support and guidance over the years and even before starting the program. Michele Karantsavelos, Maia Low, Luna Yu, and Karen Peterson have provided me amazing support and mentorship while at the Fred Hutchinson Cancer Research Center. I would also like to acknowledge all of our Pathobiology students and faculty, including my rotation project advisors: Drs. Steve Polyak, Joseph Smith, and Paul Lampe, and mentors: Drs. Gael Kurath, Jaisri Lingappa, Don Sodora, Lorenzo Giacani, Rhea Coler, Marilyn Parsons, and Julie Overbaugh.

My deepest gratitude goes to current and former Salama Lab colleagues and friends, which have been incredibly supportive and have provided a great learning environment: Jutta Fero, Jenny Taylor, Christina Tull, Christina K. Leverich, Sarah E. Talarico, Tina Gall, Desirée C. Yang, Kris Blair, Sean Schneider, Ilana Cohen, Tate H. Sessler, Marion Dorer, and Laura K. Sycuro. Thank you to all Fred Hutch high school interns, undergraduate and graduate students that have helped on many aspects of my project.

I am very thankful to all my past mentors: Drs. Otoniel Martinez-Maza and Elizabeth C. Breen at UC Los Angeles; Drs. Douglas Richman and Celsa A Spina at UC San Diego; Dr. Laurence Brunton at UC San Diego; Dr. Robert Pozos at the San Diego State University; and Drs. Sandra B. Sharp and Carlos Gutierrez at the California State University, Los Angeles.

A special acknowledgement goes to friends and colleagues I have made by volunteer work and outreach opportunities through the Graduate Opportunities Minority Achievement Program (GO-MAP), especially Cynthia Morales (Director) and Anthony Salazar (Graduate Diversity Program Specialist); the UW Chapter of the Society for the Advancement of Chicano/as and Native Americans in Science (SACNAS); the School of Public Health Diversity Committee, especially Dr. India Ornelas; Mentors at the Pacific Science Center; and all Hutch United members at the Fred Hutch.

To my Seattle, Los Angeles, San Diego friends and friends and family around the world – Thank you for your incredible friendship, love, and support, always.

DEDICATION (S)

For my parents Maria Guadalupe Maldonado and Jose Carlos Martínez and my siblings
Claudia Veronica, Hector Eduardo, and Ricardo Alberto Martínez -
Por su fortaleza, apoyo, y amor incondicional. Gracias.

For my aunts, uncles, cousins, and late grandparents Jesus and Margarita Maldonado.

For my ancestors.

For my Boyle Heights, East Los Angeles, South Central, Compton, and Watts
communities in Los Angeles, California.

For our migrant workers and their families, and our DREAMers.

For all students of the world.

For access and educational equity.

CHAPTER 1

Background

The human stomach is home to the Gram-negative, bacterial pathogen, *Helicobacter pylori* (Fig. 1.1). *H. pylori* persistently colonizes the stomach of over 50% of the world's population. Long-term infection increases the risk of developing a diverse spectrum of gastro-duodenal diseases, including chronic gastritis, peptic ulcers, and gastric cancer (Kusters *et al.*, 2006; Cover, 2016). Despite the strong association between *H. pylori* infection and stomach disease, most infected individuals remain asymptomatic. Approximately 10% of infected persons will develop peptic ulcer disease, and only a small subset of individuals will develop gastric adenocarcinoma (1-3%) or mucosa associated lymphoid tissue (MALT) lymphoma (<0.1%) (Peek and Crabtree, 2006; Wroblewski and Peek, 2013). As a consequence, the International Agency for Research on Cancer (World Health Organization) classifies *H. pylori* as a group I carcinogen (IARC, 2012). Gastric cancer is the fifth most commonly diagnosed cancer and the third most common cause of cancer-related death worldwide (IARC, 2012; Ferlay *et al.*, 2013).

Transmission and epidemiology of *H. pylori*

The estimated prevalence of *H. pylori* is approximately 70% in developing countries and 30-40% in the United States and other industrialized countries (Chey and Wong, 2007). Despite the global incidence and spread of *H. pylori* infection, the route of transmission is not clearly understood. Transmission is thought to occur by an oral – oral, gastro - oral, or fecal - oral route (Desai *et al.*, 1991; Thomas *et al.*, 1992; Luzza *et al.*, 2000; García *et al.*, 2014). Epidemiological studies support that *H. pylori* infection occurs early in childhood (Rothenbacher *et al.*, 2000;

Urita *et al*., 2013; Ertem *et al*., 2013) and through intrafamilial and extrafamilial transmission (Kivi *et al*., 2005; Schwarz *et al*., 2008; Yücel *et al*., 2009; Weyermann *et al*., 2009).

***H. pylori's* initial colonization of the gastric mucosa**

Escape from the acidic lumen

The stomach is an unfavorable environment for many bacterial organisms due to its acidity and active digestive enzymes, and for a long time is was thought to be sterile. However, *H. pylori* thrives in the human stomach. Helical cell shape is thought to facilitate *H. pylori*'s ability to bore into the mucus layer in a corkscrew-like motion, thus enhancing motility through the highly viscous mucus overlying the gastric epithelium to which it adheres. Once having traversed the thick gastric mucus layer, *H. pylori* may localize to a narrow band of gastric mucus immediately overlying the gastric epithelium and/or attach to gastric epithelial cells, and may also penetrate deeper to colonize gastric glands (Fig. 1.2D) (Howitt *et al*., 2011; Sigal *et al*., 2015). While *H. pylori* actively adheres to gastric epithelial cells, it remains extracellular and is only rarely observed within cells (Amieva *et al*., 2002; Kwok *et al*., 2002; Chu *et al*., 2010).

As a neutrophile, *H. pylori* can survive only minutes in the stomach lumen (Schreiber *et al*., 2004) and overcomes this acidic environment using urease (Fig. 1.2D), an enzyme that hydrolyzes urea to produce NH_3, locally elevating the pH to near neutral. Flagellar-mediated motility is essential for infection in several species of pathogenic bacteria (Duan *et al*., 2013). Successful colonization of the stomach by *H. pylori* requires both urease (Eaton *et al*., 1994; Eaton *et al*., 1991; Tsuda *et al*., 1994a; Tsuda *et al*., 1994b; Nakamura *et al*., 1998), and flagellar-mediated, chemosensory-directed motility (Eaton *et al*., 1996; Terry *et al*., 2005; Howitt *et al*., 2011; Rolig *et al*., 2012).

Gastric mucus: A safe haven for H. pylori

Gastric mucus protects the stomach from acid and potential insults from the environment, and is continuously sloughed off by peristaltic movement. The gastric mucus layer is approximately 200 - 400 μm in thickness, and consists of a thin adherent inner layer that covers the epithelial surface, and a thicker loosely attached layer on the luminal side (Allen *et al.*, 1993; Johansson *et al.*, 2013). *H. pylori* preferentially colonizes a narrow mucus layer immediately overlying the gastric epithelium, that is approximately 25 μm thick (Schreiber *et al.*, 2004).

The mucus layer maintains a pH gradient ranging from pH 2 at the lumen and pH 7 at the epithelial surface (Fig. 1.2D). Gastric mucus is a viscoelastic substance mainly composed of water (95%), and consists of mucin glycoprotein (3%) produced by epithelial mucus-producing cells, and other small molecules (2%) such as lipids, electrolytes, lectins, and amino acids (Allen and Garner 1980; Allen, 1981). The two gastric mucus layers differ in mucin glycoprotein concentration. The thin firmly adherent inner layer that covers the epithelial surface is approximately 30 mg mL^{-1}, while the overlying thicker loosely attached layer of mucus is approximately 15 mg mL^{-1} (Fig. 1.3) (Taylor *et al.*, 2004). Gastric mucin exhibits a reversible pH-dependent phase transition. At low pH (acidic), the viscoelastic properties of mucus become more gel-like, whereas the mucus becomes more solution-like as the pH increases (neutral) (Celli *et al.*, 2007; Bansil *et al.*, 2013).

Purified porcine gastric mucin (PGM) is homologous to the human glycoprotein MUC5AC, the major secreted mucin expressed in the stomach mucosa by surface epithelial cells (Sellers *et al.*, 1987; Bansil *et al.*, 2013). Thus, PGM has been shown to exhibit similar rheological properties to human mucus scraped from the surface of the gastric mucosa, making it an ideal model for *H. pylori's* niche environment (Schrager *et al.*, 1974; Pearson *et al.*, 1980;

Bell *et al.*, 1984; Bell *et al.*, 1985). Early studies showed that *H. pylori* is immobile in a PGM gel at low pH, although flagella could be seen rotating (Celli *et al.*, 2009). Upon addition of urea, the bacteria became motile (Celli *et al.*, 2009) because the hydrolysis of urea elevates the pH triggering a transition of PGM from a soft viscoelastic gel to a viscous solution (Celli *et al.*, 2005; Celli *et al.*, 2007). These experiments suggest that the helical shape of *H. pylori* does not help it bore its way like a corkscrew through the gel-like mucus layer of the stomach, as had been previously proposed (Yoshiyama and Nakazawa, 2000; Montecucco and Rappuoli, 2001). However, helical cell shape may enhance propulsion and swimming through viscous solutions of PGM, and I tested this directly in Chapter 2.

Current understanding on the effect of cell shape on *H. pylori* motility

From a hydrodynamics viewpoint, the shape of a swimmer is known to alter translational and rotational drag on the cell body, which can affect swimming speed and the bacterium's ability to sense chemotactic gradients in different environments (Dusenbery, 1998). Berg and Turner suggested that a helical cell shape would result in additional corkscrew-like propulsion for bacteria moving in viscous environments (Berg & Turner, 1979). Ferrero and Lee observed that in highly viscous methylcellulose (MC) solutions of varying viscosity (>100 centipoise (cP)), different clinical strains of helical-shaped *Campylobacter jejuni* were more motile than rod-shaped bacteria from several different species, *Vibrio cholerae*, *Salmonella enteritidis*, and *Escherichia coli* (Ferrero and Lee, 1988). Karim *et al.* showed that *H. pylori* and *C. jejuni* swim faster in liquid broth as compared to *E. coli,* presumably due to their helical cell body shape (Karim *et al.*, 1998). However, both these studies compare different species of bacteria, which have differences in flagellum morphology, flagellum number and arrangement, and possibly motor output, making conclusions on the influence of cell body shape difficult to interpret.

Cell shape mutants show altered motility and stomach colonization defects

Our lab and others have approached the role of *H. pylori's* cell shape in stomach colonization using genetic screens to identify cell shape determining (*csd*) genes. Several *csd* genes encode peptidases that modify the bacterial cell wall, composed of peptidoglycan (PG), which is responsible for rigidity and cell shape in most bacteria (Cabeen and Jacobs-Wagner, 2005). Loss of function mutations in the *csd* genes (*csd1, csd2, csd3, csd4, csd5, or csd6*) result in *H. pylori* mutants perturbed for normal helical cell morphology (Fig. 1.4) (Sycuro *et al.*, 2010; Bonis *et al.*, 2010; Sycuro *et al.*, 2012; Sycuro *et al.* 2013). *H. pylori* cell shape mutants show impaired stomach colonization in a mouse infection model, suggesting helical cell shape is important for initial colonization and/or persistence in the stomach (Sycuro *et al.*, 2010; Bonis *et al.*, 2010; Sycuro *et al.*, 2012).

Elimination of the PG peptidases Csd4 or Csd6 yielded bacteria with straight rod morphology, but the mutants show normal flagellation and cell growth properties (Sycuro *et al.*, 2012; Sycuro *et al.* 2013). While we had previously shown a semi-solid agar motility defect for *csd4* straight rod mutants (Sycuro *et al.*, 2012), another group suggested that *csd6* mutants (*H. pylori* strain G27) show enhanced motility in semi-solid agar as compared to wild-type (Asakura *et al.*, 2010), but the morphology of the *csd6* mutant was not assessed. In *Campylobacter jejuni*, deletion of *pgp2,* a homolog to *H. pylori csd6*, results in straight rod morphology and mutants show motility defects in semi-solid agar, defects in biofilm formation, and reduced fitness in a chick colonization model (Frirdich *et al.*, 2014).

Anatomy of the human stomach and gastric glands

The human stomach is subdivided into the following regions: the cardia (where contents of the esophagus empty into the stomach), the fundus (formed by the upper curvature of the stomach), the corpus (largest portion of the stomach where acid is produced), the antrum (distal part of the stomach), and the pylorus (a narrowing where the stomach joins the duodenum) (Fig. 1.2A). *H. pylori* shows tropism for the upper part of the stomach (corpus) or the less acidic lower part of the stomach (antrum), and may establish a home within these two different stomach niches (Fig. 1.2A). Although the majority of bacteria colonize the surface mucus, *H. pylori* may penetrate deeper to colonize and form microcolonies within corpus or antral gastric glands (Fig. 1.2D) (Howitt *et al*., 2011; Sigal *et al*., 2015).

The gastric epithelium is comprised of numerous glands that are approximately 200-500 μm deep and that extend into the lamina propia. Corpus or antral glands contain different differentiated cell types and glands are organized into four distinct zones: the surface/pit, isthmus, neck, and base (Fig. 1.2B,C). In corpus glands, the region closest to the gastric lumen is the pit where surface mucous cells reside and produce and secrete mucus in glands and at the surface. Gastric stem and progenitor cells reside in the isthmus. Mucous neck cells populate the neck. Parietal cells, which secrete acid and intrinsic factor, and endocrine cells are dispersed in all four regions of glands. The base of glands are composed of zymogenic or chief cells, which produce digestive enzymes such as pepsinogen and gastric lipase; enterochromaffin-like cells, which release histamine and stimulate acid release from parietal cells; D-cells that produce somatostatin, which inhibits acid; and enterochromaffin cells which produce hormones such as serotonin (Fig. 1.2B,C).

Antral glands have less specialized cell types and lack parietal cells, differentiated zymogenic cells, and enterochromaffin-like cells (Fig. 1.2B,C). Mucus producing cells reside at the surface pit and neck. Gastrin secreting G-cells reside in the middle portion of gastric glands, and stimulate the release of histamine and acid in the corpus. D-cells, enterochromaffin cells, and adult stem cells reside at the base of glands. Stem cells can differentiate into any of the cell types described above and are constantly renewed as cells are shed into the lumen.

***H. pylori* virulence factors that mediate persistence in the stomach**

H. pylori strains have a high level of intraspecies genetic diversity (Blaser and Berg, 2001; Suerbaum and Josenhans, 2007) and strain-specific variation in virulence factors may affect host cell signaling pathways. The risk of developing overt disease differs among *H. pylori* infected individuals.

Cytotoxin-associated gene A (CagA)

Unrelated *H. pylori* strains vary in the presence or absence of the chromosomal region known as the *cag* pathogenicity island (PAI). Infected individuals may contain an intact or incomplete *cag*PAI, while others may have a *cag*PAI that has undergone chromosomal rearrangements (Olbermann *et al.*, 2010). The *cag*PAI encodes an antigenic effector protein known as CagA. CagA is delivered into host cells through a Type IV Secretion System (T4SS)-mediated process also encoded within *cag*PAI (Tegtmeyer *et al.*, 2011). Upon delivery, CagA undergoes tyrosine phosphorylation by Src and Abl family kinases (Odenbreit *et al.*, 2000; Tegtmeyer *et al.*, 2011). This phosphorylated form can interact with multiple host cell components to cause many host cell changes, such as changes in epithelial cell shape and polarity (Segal *et al*., 1999; Saadat *et al*., 2007), and disruption of apical epithelial junctions (Amieva *et al*., 2003). CagA causes altered epithelial cell differentiation, which may result in an epithelial to mesenchymal phenotype change (Bagnoli *et al*., 2005). In addition, CagA may enhance cell proliferation or inhibit apoptosis (Suzuki *et al*., 2009), and activate gastric stem cells (Sigal *et al*., 2015). Individuals infected with *cagA*-positive *H. pylori* strains have a higher risk of developing gastric cancer.

Vacuolating cytotoxin A (VacA)

All *H. pylori* strains contain a *vacA* gene, which encodes a pore-forming toxin (VacA) that may cause vacuolation of epithelial cells (Cover and Blanke, 2005; Kim and Blanke, 2012). However, *H. pylori* shows allelic diversity of *vacA* and different strains produce and secrete varying levels of VacA. In addition, VacA may cause alterations in endosomal function (Willhite and Blanke, 2004; Gauthier *et al*., 2007), alter mitochondrial membrane permeability (Calore *et al*., 2010), induce autophagy (Terebiznik, 2009) and accumulation of reactive oxygen species (Tsugawa *et al*., 2012), and may also inhibit T-lymphocyte activation (Gebert *et al*., 2003; Sundrud *et al*., 2004).

H. pylori adhesins

H. pylori adhesive factors help mediate *H. pylori* adherence to gastric epithelial cells. Most adhesins belong to the largest outer membrane protein (OMP) family, the Hop family, which consists of the well-known adhesins BabA, SabA, AlpA/B, HopZ, and OipA (Backert *et al*., 2011). *H. pylori* strains vary in the expression of OMPs, but the different adhesins show functional redundancy for binding to the gastric epithelium. Host receptors for some of these adhesins have been defined. BabA binds to fucosylated Lewis^b antigen on surfaces of gastric epithelial cells, and SabA binds to the carbohydrate structure sialyl-Lewis^x antigen expressed on gastric cells (Gerhard *et al*., 1999; Ilver *et al*., 1998; Backert *et al*., 2011). SabA is associated with an increased gastric cancer risk, but a reduced risk for duodenal ulceration (Yamaoka *et al*., 2006).

Animal models of *H. pylori* infection

To date, many animal models of infection have been developed to investigate the pathogenesis of acute and chronic *H. pylori* infection and gastric cancer pathogenesis (Peek and Blaser, 2002). These include the mouse model (Tomb *et al*., 1997, Alm *et al*., 1999, Censini *et al*., 1996, Karita *et al*., 1991, Karita *et al*., 1994, Marchetti *et al*., 1995); the piglet model (Poutahidis *et al*., 2001); the germ-free piglet model (Krakowka *et al*., 1987, Lambert *et al*., 1987); the mongolian gerbil model (Hirayama *et al*., 1999, Ikeno *et al*., 1999, Zheng *et al*., 2004, Ogura *et al*., 2000; Yokota *et al*., 1991); cat model (Fox *et al*., 1996); and non-human primates (Bronsdon *et al*., 1988; Dubois *et al*., 1999).

The mouse and mongolian gerbil models have been gold standards for research investigating *H. pylori* bacterial virulence factors and host response to chronic infection. However, the mouse model of infection is the most convenient due to its cost and availability.

Comparative anatomy of human and mouse stomachs

As discussed earlier, the human stomach consists of the stomach regions: the cardia, glandular regions: fundus, corpus, and antrum, and the pylorus (Fig. 1.2A). Humans have a "Z-line" at the gastroesophageal junction, right above the cardia. The mouse stomach, in contrast, lacks a "Z-line" and contains two grossly distinct regions, a non-glandular (forestomach) region and a glandular region (corpus and antrum), and the pylorus (Fig. 1.5). The forestomach is lined with keratinized squamous epithelium, and is separated from the glandular corpus region by a raised mucosal fold called the limiting ridge, often referred to as the squamocolumnar junction. The glandular mucosa immediately adjacent to the forestomach parallels the morphology of the human cardia. The cellular composition of mouse corpus and antral glands resemble that of human corpus and antral glands.

Mouse model of H. pylori infection

As in the human stomach, *H. pylori* may colonize both the corpus and antrum during initial colonization of the mouse gastric mucosa (Akada *et al*., 2003), and can be detected within 14 hours of infection by *H. pylori* isolation from the mouse stomach (Rolig *et al*., 2012). Little is known about the localization pattern of *H. pylori* and its distribution within corpus or antral glands after chronic infection. Host selective pressures and bacterial genetics may influence the distribution of bacteria within these two stomach regions (Akada *et al*., 2003; Rolig *et al*., 2012). Humans display varying patterns of gastritis due to *H. pylori* infection, and this may subsequently impact acid secretion in the stomach. Studies have shown that an antral predominant gastritis, with increased acid production, is a risk factor for duodenal ulcers, and a corpus-predominant pattern of gastritis, with resulting loss of parietal cells and acid production, increases the risk for gastric cancer (Blaser and Atherton, 2004; Cover, 2016). Studies seeking to understand *H. pylori* stomach tropism and its localization within the gastric mucosa are warranted.

Different mouse strains have been used to study *H. pylori* acute and chronic infection. For the purpose of this dissertation, I will focus discussion on the C57BL/6 mouse strain and on *H. pylori* strains commonly used to investigate gastric disease.

The C57BL/6 mouse strain has been extensively used to study *H. pylori's* role in gastric carcinogenesis. Mouse colonizing *H. pylori* isolates may induce gastritis and gland atrophy in C57BL/6 mice, but they do not induce neoplasia (Sakagami *et al*., 1996; Ferrero *et al*., 1998). Finding a reproducible animal model of persistent and chronic infection that resembles the *H. pylori*-associated gastritis observed in humans had been challenging until Lee *et al.* adapted a Cag A-positive and Vac A-expressing *H. pylori* strain in the mouse stomach (Lee *et al*., 1997). This *H. pylori* strain, known as Sydney strain 1 (SS1), is a mouse-adapted strain and has been used for long-term infection studies (Lee *et al.*, 1997; Thompson *et al*., 2004). Long-term infection with SS1 produces disease-like symptoms as observed in human disease, such as chronic active gastritis and chronic inflammation (Lee *et al*. 1997; Dey *et al*., 1998; van Doorn *et al*., 1999; Kamradt *et al.*, 2000; Day *et al*., 2001; Thompson *et al*., 2004). While SS1 contains the *cag*PAI, it is defective for T4SS function and does not translocate *cag*A into host gastric epithelial cells, presumably due to uncharacterized mutation(s). The precursor strain to SS1, pre-mouse SS1 (PMSS1), maintains an active *cag*PAI T4SS and persistently colonizes the stomachs of mice, leading to the development of gastritis, gastric atrophy, epithelial hyperplasia, and metaplasia (Arnold *et al*., 2011).

Unique approaches in the field to study *H. pylori* localization within the stomach

Several methods are used for the identification of *H. pylori* infection in gastric tissue and for histological examination. Routinely, gastric tissue samples are fixed in formalin and embedded in paraffin wax to generate sections (4-5 μm thick) that can be used to visualize *H. pylori* using different staining methods. These include modified Giemsa, Warthin-Starry, Genta, Silver stain, and imunohistochemical *H. pylori* antibody stains (Ashton-Key *et al*., 1996; Genta *et al*., 1994; Iwaki *et al*., 1998). This method is practical for a clinical or research laboratory setting intended to identify *H. pylori* in human gastric biopsies or in animal tissue sections, but is limiting for studying *H. pylori's* localization within the stomach and/or bacterial-host interactions. This method relies on random sampling of thin tissue sections that do not fully capture the complex 3-dimensional (3-D) microanatomies of host cells and the anatomical localization of *H. pylori* to distinct sites of the surface epithelium and within the gastric gland lumen.

More recently, confocal laser scanning microscopy, scanning electron microscopy (SEM), and optical tomography have been used to study 3-D tissue structures and to assess bacterial localization within tissue (Tan *et al*., 2009; Smith *et al*., 2010). Advances in high resolution confocal microscopy and 3D-imaging technologies have provided new insights on the localization of extracellular bacteria within tissue samples. 3D-imaging has been used to study the temporal localization of *Pseudomonas aeruginosa* within the mouse corneal epithelium and subsequent innate immune defense responses (Tam *et al*., 2011). Recently, Amieva and colleagues have used confocal microscopy and SEM to visualize *H. pylori* and determine its localization within gastric glands of human tissue or infected mice (Howitt *et al*., 2011; Sigal *et al*., 2015; Noto *et al*., 2015). These studies are providing insight on how *H. pylori* colonization of gastric glands directly impact host gastric epithelial cells by interacting with progenitor cells and by activating stem cells (Sigal *et al*., 2015). In addition, new tools have been used to quantify the invasion depth of *H. pylori* in the glands, further revealing that *H. pylori* gland colonization influences mitotic progenitor cell division in the stomach (Earle *et al*., 2015).

Three-dimensional imaging methods will provide important contributions to the field of microbiology. This system may be used to study bacterial localization to different tissue compartments, bacteria-host interactions, inter-bacterial interactions, and bacterial behavior on different spatial and temporal time scales. Furthermore, studying the 3-D landscape of infected tissue samples may provide additional insight on host cellular processes in response to infection, and may help decipher contributing factors to disease progression and/or control of disease (Bumann, 2015).

This dissertation work uses confocal microscopy and 3-D reconstruction of the mouse stomach to characterize the effect of helical cell morphology on *H. pylori's* niche acquisition in the stomach.

PROJECT AIMS

The goals of my dissertation are to investigate how cell shape impacts *H. pylori's* motility and niche acquisition in the stomach. Chapter 2 characterizes the effect of cell shape on *H. pylori*'s motility in different viscous environments, including physiologically relevant solutions of purified porcine gastric mucin (PGM). Different wild-type *H. pylori* strains vary cell shape and flagellum morphologies, and show diverse swimming speeds in broth and gastric mucin media that reflect both temporal variation in speed and morphological variation in the population. To directly test the effect of helical cell shape on *H. pylori's* motility, I tested straight rod mutants in different viscous environments. Straight rods show reduced swimming speeds and a higher fraction of immobilized bacteria in PGM. As described in chapter 3, I tested the effect of flagellum number on *H. pylori's* swimming speed in viscous mucin media. A flagellar mutant skewed to lower number of flagella showed decreased swimming speeds, and a mutant with increased flagellation provides a swimming speed advantage. Chapter 4 describes the implementation of a mathematical model to describe the concerted effects of both cell shape parameters and flagellum number on *H. pylori's* swimming speed. The work described in Chapters 2-4 has been published in *Molecular Microbiology*. Portions of the introduction in the manuscript have been used in Chapter 1 (background). The results, discussion, and experimental procedures sections of the manuscript have been used in Chapters 2-4.

Shape mutants perturbed in normal helical cell morphology show stomach colonization defects in a mouse model of infection (Sycuro *et al*., 2010, 2012). I hypothesized that helical cell shape is important for motility *in vivo* and facilitates *H. pylori's* ability to penetrate the gastric mucosa for efficient colonization and localization to specific niches within the stomach. To elucidate the role of cell shape on stomach colonization, I conducted a time course of single-strain infection studies on mice with wild-type helical bacteria, a curved rod mutant (Δ*csd1*), and a straight rod mutant (Δ*csd6*). Chapter 5 describes how cell shape impacts *H. pylori* niche acquisition early after infection (1 day and 1 week) and after persistent and chronic infection (1, 2, and 4 months). Chapter 6 describes conclusions and proposes future experiments based on the work summarized in this dissertation.

FIGURES

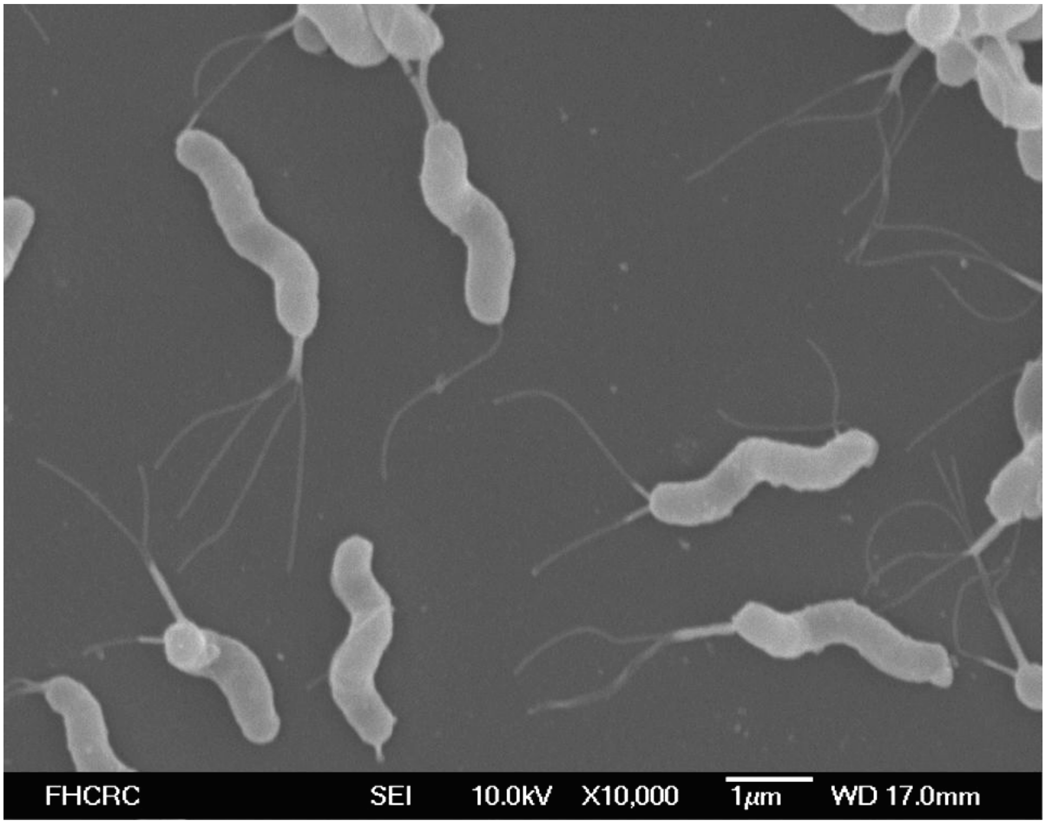

Figure 1.1. Scanning Electron Micrograph (SEM) of *H. pylori* showing its characteristic helical cell morphology and polar flagella. Strain used: LSH100.

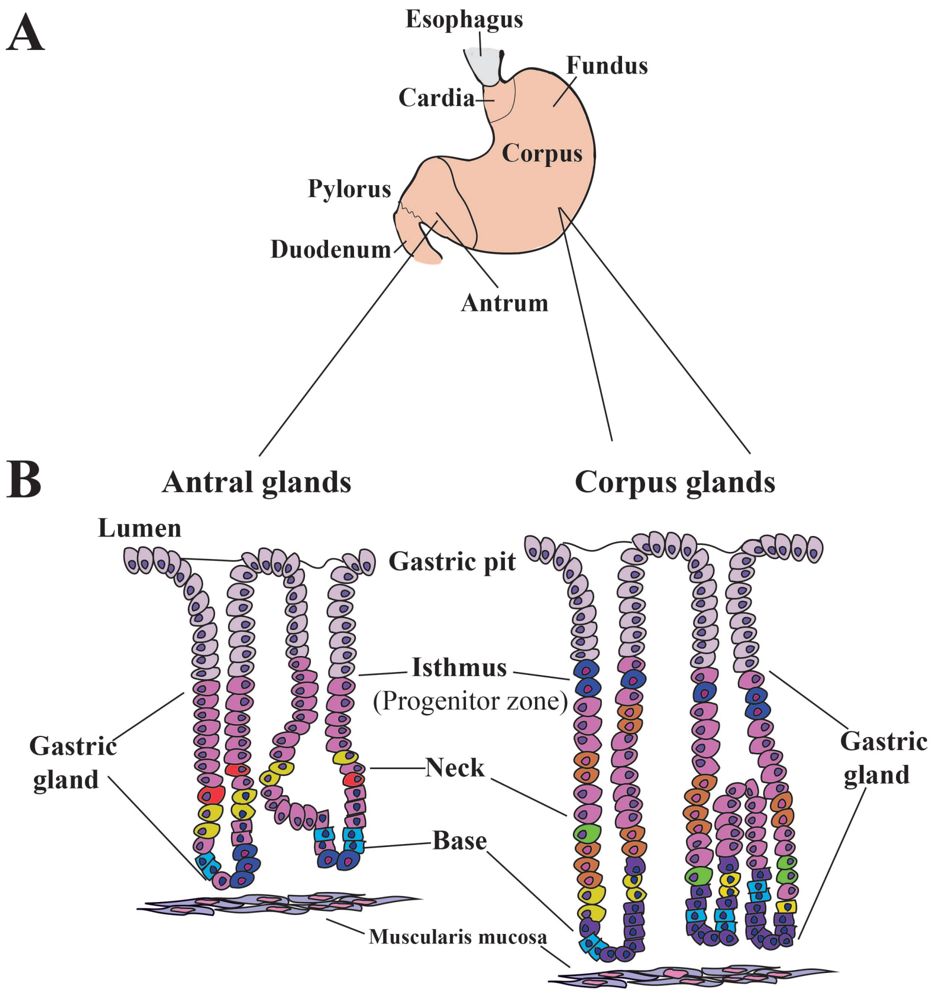

C

Location	Cell type	Substance secreted
Corpus & Antrum	⚪ Surface mucous cell 🟣 Mucous neck cell	Mucus; Bicarbonate
	🟦 Enterochromaffin cell	Serotonin
	🟡 D cell	Somatostatin (inhibits acid)
	🔵 Stem cell	
Corpus	🟢 Enterochromaffin-like cell	Histamine (stimulates acid)
	🟠 Parietal cell	Acid (HCL); Intrinsic factor
	🟪 Chief cell	Pepsinogen; Gastric lipase
Antrum	🔴 G cell	Gastrin (stimulates acid)

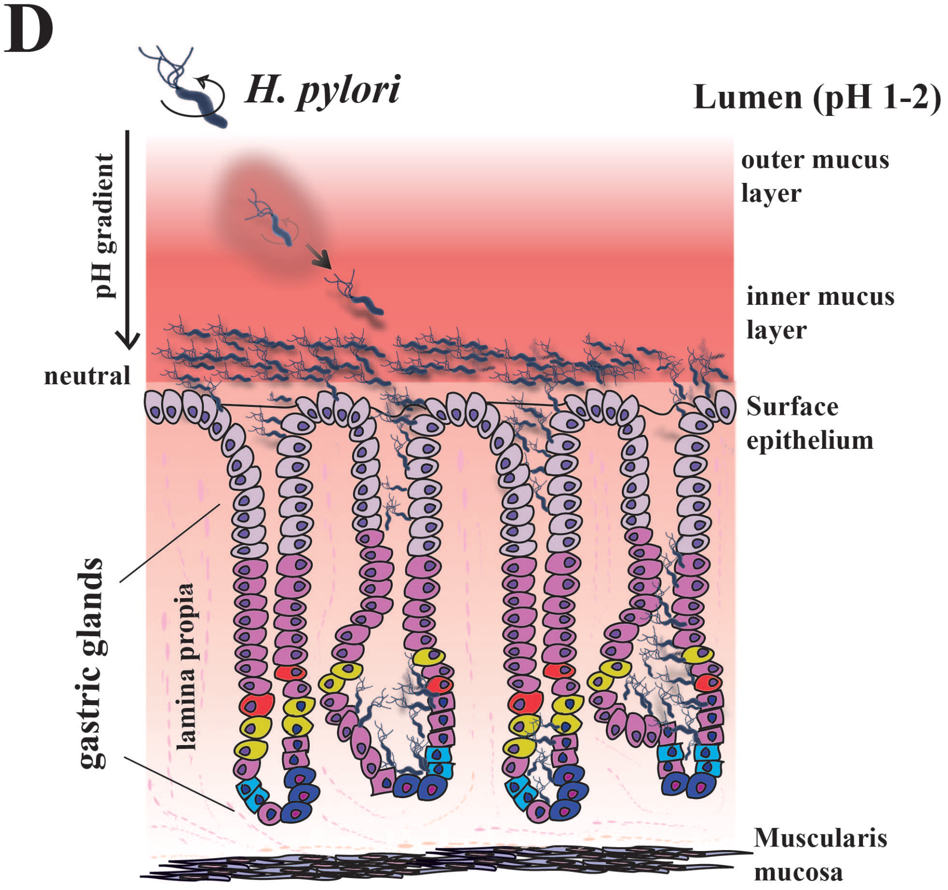

Figure 1.2. Human stomach anatomy and *H. pylori*'s colonization of the human gastric mucosa. (A) Schematic showing the different stomach regions: the cardia (surrounds the opening of the esophagus into the stomach), fundus (the area above the level of the cardial orifice), corpus (the largest region of the stomach and where acid is produced), and the antrum (located at the distal end of the stomach). (B) Representative corpus and antral glands showing the different cell types that comprise glands and their locations at the pit, isthmus, neck, or base of glands. (C) A table summarizing the cell types that comprise corpus and antral glands, and the substances they secrete. (D) A schematic showing *H. pylori's* colonization of the human gastric mucosa. The image shows a model for *H. pylori's* corkscrew motion as it first penetrates the outer mucus layer. The localized production of urease is shown in pink, surrounding the cell. Urease locally raises the pH to promote bacterial survival and solubilizes the mucus gel to facilitate *H. pylori*'s motility. Flagellar-based motility and chemotaxis are required for *H. pylori* to reach its preferred niche, at the surface mucus layer immediately overlying the gastric epithelium. *H. pylori* also penetrates deeper to colonize gastric glands, as shown in this image of infected antral glands. Also shown is the lamina propia, a thin layer of loose connective tissue that lies beneath the epithelium and is the site of infiltrating immune cells; and the muscularis mucosa, a thin muscle layer separating the lamina propia from the submucosa. Note: Bacteria are not drawn to scale.

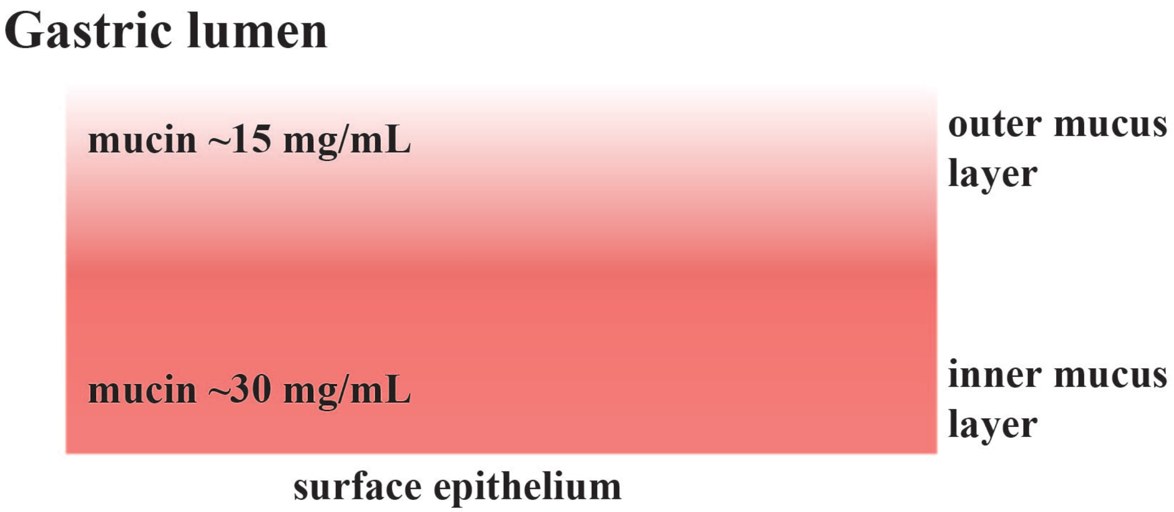

Figure 1.3. Gastric mucus layers differ in mucin glycoprotein concentration.

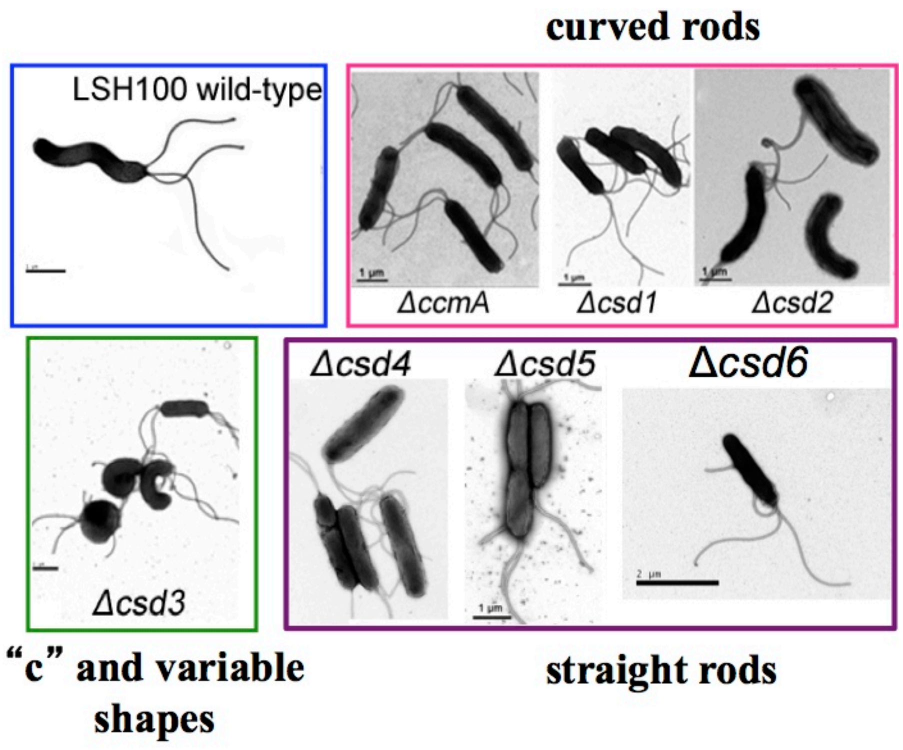

Figure 1.4. ***H. pylori*** **cell shape mutants show altered helical cell morphology.** Transmission Electron Micrographs of a wild-type *H. pylori* strain (LSH100) and isogenic cell shape mutants: curved rod mutants (Δ*ccmA*, Δ*csd1*, and Δ*csd2*); a mutant with "c"-shape and variable morphologies; and straight rod mutants (Δ*csd4*, Δ*csd5*, and Δ*csd6*). Scale bar = 1 μm for all except for Δ*csd6* where the scale bar = 2 μm. Figure adapted from Sycuro *et al*. (2010, 2012, 2013).

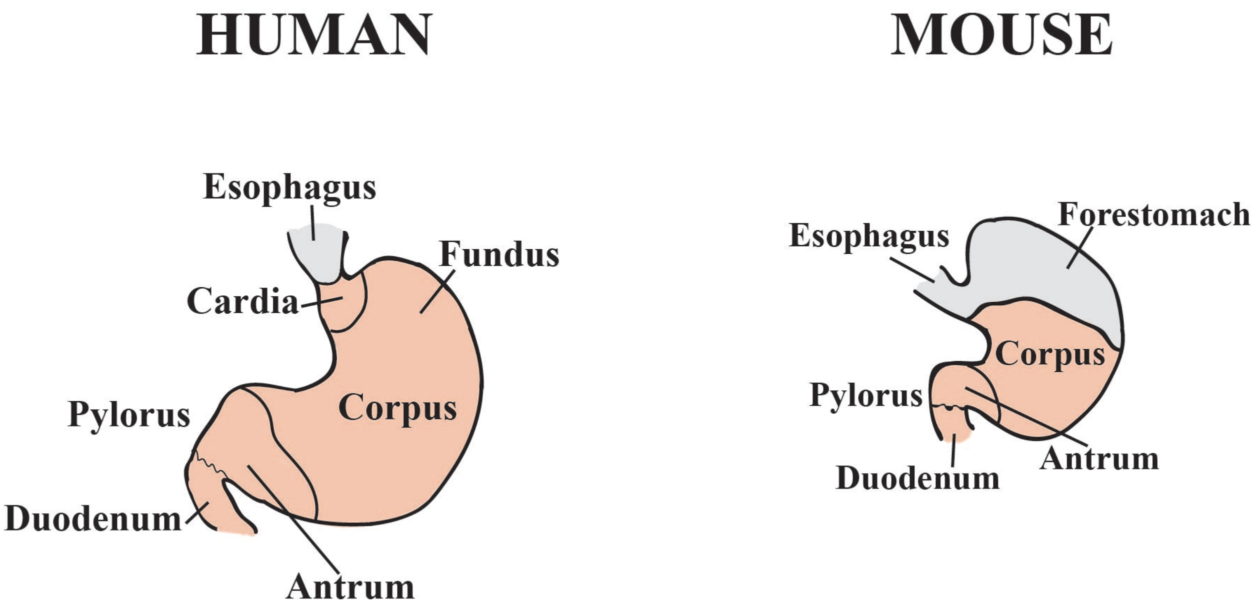

HUMAN

MOUSE

Figure 1.5. Comparative anatomy of the human and mouse stomach. The human stomach is lined with glandular mucosa (cardia, fundus, corpus, and antrum), whereas the mouse stomach is divided into two regions: a non-glandular (forestomach, grey) and glandular stomach region (nude color) that includes the corpus and antrum.

CHAPTER 2

The helical cell shape of *H. pylori* promotes robust motility in viscous environments

INTRODUCTION

In this chapter, we present a detailed study relating morphology and motility using optical and electron microscopy to measure cell shape and flagellum parameters, and live-cell imaging to track individual bacteria to examine *H. pylori's* swimming behavior in several polymer solutions, including the physiologically relevant porcine gastric mucin (PGM).

To probe the contribution of cell morphology to *H. pylori* motility in different viscous media, we analyzed three unrelated clinical *H. pylori* strains commonly used for genetic and animal infection studies, LSH100, B128, and PMSS1 (Table 2.1). To directly address whether helical cell shape impacts *H. pylori's* motility, we analyzed the motility of two isogenic straight rod mutants that show similar flagellum parameters to their respective parental strains, LSH100 or PMSS1.

RESULTS

Gastric mucin shows physiologically relevant solution and gel-like properties

To examine the micro-rheological properties of the environment in which *H. pylori* motility is to be measured, we used microscopic single particle tracking. This technique probes the Brownian motion of particles (Cicuta and Donald, 2007) and has been previously applied to investigate the microrheology of PGM (Lieleg *et al.*, 2010; Bansil *et al.*, 2013; Georgiades *et al.*, 2014). To model the viscous environment of the human gastric mucosa where *H. pylori* resides, we used physiologically relevant concentrations of PGM of 15 and 30 mg mL^{-1}. For comparison to previous work on *H. pylori* motility in viscous solutions (Hazell *et al.*, 1986; Worku *et al.*, 1999), we also examined methylcellulose (MC) solutions at concentrations of 10 and 15 mg mL^{-1}. Fig. 2.1A shows the averaged mean squared displacement (MSD =$\langle r(t)^2 \rangle$, μm^2) of 1μm diameter fluorescent polystyrene particles calculated from the measured position ($r(t)$) as a function of time (t). To confirm that bacteria experience a similar environment, we also tracked Δ*motB* mutants, which retain wild-type flagellum structure but have non-functional flagellum motors (Ottemann & Lowenthal, 2002) (Fig. 2.1B). We found that the MSD values of non-motile bacteria were smaller relative to those acquired for diffusing particles (Fig. 2.1A,B). This reflects the increased drag due to the larger size and anisotropic shape of bacteria compared to spherical particles. The time dependence of the MSD is usually described using the relation $\langle r(t)^2 \rangle = At^{\alpha}$. In a viscous fluid, particles exhibit normal Brownian diffusion with the exponent $\alpha = 1$ and $A = 4D$, where A is the constant of proportionality and D is the diffusion constant of the particle (Cicuta & Donald, 2007). In complex fluids, such as viscoelastic gels, particles exhibit sub-diffusive behavior with an exponent of $\alpha < 1$.

By fitting the ensemble averaged MSD, we obtained the exponent α and A. For each solution, the values of α were the same for both polystyrene particles and Δ*motB* bacteria (Fig. 2.1C). Brownian diffusion ($\alpha = 1$) was observed in broth, PGM at 15 mg mL^{-1}, and MC solutions of 10 and 15 mg mL^{-1}, implying these solutions behave as viscous liquids (Fig. 2.1C). The viscosities (η) (cP) of each solution were calculated from the measured bead diffusion constants via the Stokes Einstein relation ($\eta = kT/6\pi RD$), where T and R represent temperature and bead radius, respectively (Fig. 2.1C). Sub-diffusive behavior was observed for PGM at 30 mg mL^{-1} (α=0.65 +/- 0.10), implying that at this higher concentration, PGM is a gel-like viscoelastic polymer (Bansil *et al*., 2013). Our results are in agreement with the observations of Georgiades *et al.*, where a transition to viscoelastic behavior was observed in PGM at 25 mg mL^{-1} (Georgiades *et al*., 2014). Our results suggest that PGM at 30 mg mL^{-1} displays gel-like properties that resemble the rheological gel-like environment of mucus near the gastric epithelium, and PGM at 15 mg mL^{-1} displays solution-like properties that resemble the rheological environment that *H. pylori* encounters as it swims through the gastric mucus found near the acidic lumen of the stomach (Taylor *et al*., 2004). We used these PGM concentrations in our *in vitro* experiments to model the solution and gel-like environments of stomach mucus and to examine *H. pylori* motility.

Wild-type H. pylori strains display diverse and distinct cell body and flagellum morphologies

To address the impact of cell morphology on motility, we began by analyzing the morphology of three unrelated wild-type strains: LSH100, B128, and PMSS1 (Table 2.1). *Helicobacter pylori* clinical strains show a high degree of genetic and phenotypic variability and there is no consensus lab strain used by the *H. pylori* research community. These commonly used strains were all isolated from symptomatic human patients on three different continents (PMSS1-Australia, LSH100-Europe, B128-North America) and robustly colonize mice (LSH100, PMSS1, B128) or mongolian gerbils (B128), the major small animal models of *H. pylori* stomach infection. Cell morphology was characterized by analyzing phase contrast images using the CellTool software (Pincus and Theriot, 2007; Lacayo *et al*., 2007; Sycuro *et al*., 2010), which has been previously used to segregate *H. pylori* cells based on different shape parameters, including cell length, diameter, and side curvature (Sycuro *et al*., 2010; Sycuro *et al*., 2012; Sycuro *et al.,* 2013). Side curvature is the measure of the total curvature of a bacterial cell excluding its poles and the curvature itself is defined as the reciprocal of the radius of a circle that is tangent to a curve made at any point (Sycuro *et al.*, 2010). Wild-type *H. pylori* strains display heterogeneous morphologies ranging from straight to predominantly helical, and bacterial cells of different cell lengths were observed within each population (Fig. 2.2A). As summarized in Table 2.2, all three strains have similar values of cell diameter but distinct cell length and side curvature profiles.

To further characterize helical morphology, we obtained the helical radius (R) and pitch (P) (length of one complete helical turn) using centerline measurements provided by CellTool. For each bacterial cell, centerlines were fitted using a sine function $y = Rsin\,(\frac{2\pi}{P}x + \delta)$ (Fig. 2.2B). Figures 2.2C-E shows the distribution of each strain's cell length, helical radius, and helical pitch, and their average values are summarized in Table 2.2. All strains showed overlap in cell length distributions, but the B128 population shows a higher probability of shorter cells (Fig. 2.2C). PMSS1 showed an increased helical pitch as compared to both LSH100 and B128 (Fig. 2.2E), while LSH100 showed significantly increased helical radius as compared to both B128 and PMSS1 (Fig. 2.2D and Table 2.2). These observations correlated well with LSH100 having increased side curvature (Fig. 2.2A and Table 2.2), while B128 and PMSS1 showed smaller values consistent with a smaller radius.

We also examined flagellum morphologic parameters using transmission electron microscopy (TEM) and scanning electron microscopy (SEM) (see Experimental Procedures). The three wild-type strains showed a mixed population of cells with 0 to 6 uni-polar flagella (Fig. 2.2F). LSH100 and B128 shared a median flagellum number of 3 +/- 1 (+/- standard deviation), while PMSS1 had a median flagellum number of 4 +/- 1 and a higher proportion of bacteria with 4 to 6 flagella (55%) relative to LSH100 (34%) and B128 (36%) (Fig. 2.2F).

LSH100 had a median flagellum length of 3.4 +/- 0.3 μm, which was shorter than both PMSS1 (4.4 +/- 0.3 μm) and B128 (4.4 +/- 0.4 μm) (Fig. 2.2F).

In summary, the three wild-type *H. pylori* strains examined varied in multiple cell morphologic parameters expected to influence motility, including cell length (B128 shortest), helical radius (LSH100 highest), flagellum number (PMSS1 highest), and flagellum length (LSH100 shortest).

Wild-type H. pylori strains display a broad distribution of swimming speeds

To examine *H. pylori* motility, we used live-cell imaging and particle-tracking methods to automatically track hundreds of individual bacterial cells in broth and in viscous PGM or MC media. We collected videos of bacteria swimming at the mid-level plane between the coverslip and the glass slide. We tracked bacteria from ten second videos, which allowed us to capture bacteria swimming in the field of view and it provided sufficient time to acquire a broad sampling of each bacterium's instantaneous swimming speeds (Fig. 2.3). The recorded videos show that *H. pylori* exhibits a complex motion consisting of periods of straight swimming (runs), interrupted by short periods of directional reorientation and/or reversal in swimming direction (see Video 1). Figure 2.4A shows a representative bacterial trajectory and Fig. 2.4B shows its corresponding instantaneous speed as a function of time. The speed is observed to vary between high values (~ 10 - 15 μm/s) and low values of ~ 1 μm/s. The low speeds show a one to one correspondence with reorientation events represented by a large change in swimming direction ($\Delta\theta$) as shown in Fig. 2.4C. Using a similar method to Son *et al.* (Son *et al.*, 2013) we classified reorientations as any event where abrupt decreases in bacterial swimming speed ($v_{local\ min} < (v_{avg} / 2)$) happened or $\Delta\theta$ was significantly larger than angle changes resulting from rotational diffusion ($\Delta\theta > 25$ degrees was used exclusively in this study). Reversals were classified as any reorientation event for which the directional angle change $\Delta\theta > 110$ degrees (Fig. 2.4). In our analysis, the direction of swimming observed at the start of the video was considered "forward" solely as an annotation relevant to the video frame and not relative to bacterial polarity. Polarity could not be determined because bacterial flagella were not observable at the magnification and optical resolution of our experiments. After a reversal occurred, bacteria were assumed to swim in the reversed direction until another reversal event took place. Using these criteria, all trajectories were segmented into forward and reverse swimming directions and reorientation events. From the segmented trajectories, we calculated several motility parameters: instantaneous swimming speeds (the speed between two points of a track); reversal frequency (reversals per second) and speed measurements of both forward and reverse directions; and percent track linearity (%TL, the ratio of average straight line velocity (μm/s) to average swimming speed (μm/s) x 100%). Measurements acquired during reorientation events were excluded from our speed calculations.

As shown in Fig. 2.5A-C, the three wild-type *H. pylori* strains exhibited broad overlapping distributions of instantaneous swimming speeds in broth and PGM. These distributions are concatenations of instantaneous swimming speeds from all bacterial cells analyzed for each strain and in each solution tested. The shapes of these broad speed distributions depend on both strain and medium in a complex way, presumably reflecting the differences in cell shape, number of flagella, and flagellum length. To characterize such broad distributions it is not enough to use a single average. We therefore computed the average speed (v_{avg}), median speed (v_m), maximum speed (v_{max}), and standard deviation (σ) of the distribution of speeds (Table 2.3). The maximum swimming speed gives a measure of the fastest swimming speed, likely arising when all flagellar motors are firing in synchrony.

First considering LSH100 and PMSS1, Fig. 2.5A-C shows that LSH100 speed distributions are different from those of PMSS1, having lower speeds than PMSS1 in all three solutions. For example, in all three solutions v_{avg} and v_m are almost twice as large for PMSS1 compared to LSH100 and the standard deviation is approximately 30-40% larger (Table 2.3). Although v_{avg} of LSH100 and PMSS1 does not vary much between broth and PGM, these strains show increased proportions of higher swimming speeds in PGM compared to broth. This observation is also confirmed by the change in v_m. For LSH100 we find v_m = 5.7 μm/s in broth, which increases to 6.5 μm/s in PGM at 15 mg mL^{-1}, and exhibits a similar median swimming speed of 6.4 μm/s in PGM at 30 mg mL^{-1} (Table 2.3).

B128 shows similar speed distributions to LSH100 in broth and PGM at 30 mg mL^{-1} (Fig. 2.5A,C), while its speed distribution shifts to higher speeds in PGM at 15 mg mL^{-1}, becoming more similar to PMSS1 (Fig. 2.5B). This may be attributed to that fact that the shape of B128 is similar to PMSS1 but its flagellum parameters are closer to those of LSH100 (Fig. 2.2F). B128 also exhibits the non-monotonic trend in PGM observed for LSH100 and PMSS1 (Table 2.3).

In addition to monitoring the speed of swimming bacteria, we also recorded the number of bacteria that appeared immobilized (bacteria stuck in the medium) for LSH100 and PMSS1 in broth and PGM. Bacteria that exhibited displacements < 0.3 μm were classified as immobile. The percentage of immobilized bacteria in all solutions (10–50%) exceeded the percentage of bacteria with zero flagella (4-9%), and increased with increasing viscosity of the media (Table 2.4). PMSS1 had the fewest percent-immobilized bacteria and the highest v_m in all solutions.

Thus, the tendency to not be immobilized in the viscoelastic PGM gel correlates with swimming speed.

Speed distributions also reflect temporal variation of individual bacteria

The speed distributions shown in Fig. 2.5 arise from two unrelated factors: (i) variation in bacterial cell shape and size in the population, and (ii) variation in the swimming speed of individual bacteria over time. As seen in Fig. 2.4B, individual bacteria alter their swimming speed by an order of magnitude over the time of tracking (typically 1-10 seconds). This temporal variation cannot result from variation in cell morphology, which should remain constant during the track time (*H. pylori* doubling time is 2.5 - 4 hours, depending on the strain, under these growth conditions). In order to separately assess the temporal variation we processed the trajectories of each bacterium and obtained the standard deviation of each bacterium's speed, σ_{bac}. Figure 2.5D shows the distribution of speed standard deviations, σ_{bac}, for the three different *H. pylori* strains in PGM at 15 mg mL^{-1}. The breadth of the σ_{bac} distributions (Fig. 2.5D) indicate that population level speed variation (Fig. 2.5B) is largely due to speed variation within individual bacterial trajectories (as illustrated for an example bacterium in Fig. 2.4B). LSH100, B128, and PMSS1 showed slightly different distributions (K-S statistics, $p < 0.05$ for all comparisons) suggesting they may have different swimming dynamics in PGM (Fig. 2.5D). We obtained similar results when comparing LSH100 to B128 and PMSS1 to B128 in PGM at 30 mg mL^{-1}, although these differences were not observed when comparing LSH100 to PMSS1 in PGM at 30 mg mL^{-1} (K-S, $p = 0.89$) (Fig. 2.6B). Interestingly, all wild-type strains showed similar distributions in broth (K-S, $p > 0.05$) (Fig. 2.6A). These results indicate that the temporal variation in the swimming speeds of *H. pylori* depend on both the strain and swimming environment, and the breadth of the speed distribution is largely due to individual bacterial cells varying their swimming speed over time.

Helical cell shape promotes increased motility in broth and viscous media

To directly address whether the helical cell shape of *H. pylori* impacts its motility, we compared the motility of helical wild-type bacteria to isogenic straight rod mutants (Δ*csd6*) of LSH100 (see Videos 1 and 2). We first confirmed that the cell shape mutant did not show altered flagellum number or length (Table 2.5 and Fig. 2.7), as previously described (Sycuro *et al.*, 2012). We found that while the overall speed distribution of the LSH100 Δ*csd6* mutant was similar to wild-type LSH100 in broth (Fig. 2.8A), v_m decreased by 7% (Table 2.3). In addition, straight rods displayed an 11% reduction in v_m in PGM at 15 mg mL^{-1}, and an 8% reduction in v_m in PGM at 30 mg mL^{-1} (Table 2.3). While the reduction in speed between the Δ*csd6* mutant and wild-type is statistically significant in the PGM solutions (K-S, p <0.0005), it is not so in the broth solution (K-S, p =0.0955) (Table 2.3).

To further test the generality of this phenomenon, we generated a *csd6* deletion mutant in the PMSS1 strain background (Table 2.6). We first analyzed the cell shape of this strain and found that deletion of *csd6* resulted in straight rod morphology, measured as loss of cell curvature (Fig. 2.9), as previously shown in LSH100 (Sycuro *et al.*, 2013). The PMSS1 Δ*csd6* straight rod mutant also had normal flagellum number and length compared to wild-type (Table 2.5 and Fig. 2.7). In this case, we found significant differences between Δ*csd6* mutant and wild-type speed distributions in broth and in viscous PGM media (Fig. 2.8B), with a slightly larger reduction in median swimming speed compared to LSH100 (Table 2.3). For example, straight rods displayed an 11% reduction in v_m in broth and in PGM at 15 mg mL^{-1}, and a 13% reduction in median swimming speed in a gel-like PGM environment at 30 mg mL^{-1} (Table 2.3).

To investigate whether straight rods exhibited reduced swimming speeds in a different viscous polymer solution, we analyzed their swimming speeds in viscous MC media. In agreement with our results in PGM, we found significant differences in swimming speed distributions (Fig. 2.8C,D) and reduced median swimming speeds for straight rods as compared to their respective wild-type strains (Table 2.3). Both straight rod mutants also showed a higher fraction of immobilized bacteria relative to their respective wild-type parental strains. This effect was most pronounced in PGM at 15 mg mL^{-1} where a 25 and 40% increase in % immobilized bacteria was observed for LSH100 Δ*csd6* and PMSS1 Δ*csd6*, respectively (Table 2.4 and Fig. 2.10). Our results indicate that helical morphology enhances the fraction of motile *H. pylori* and its swimming speed. Motility enhancement was seen in all solutions but did not show an obvious dependence on viscosity. In addition, high-magnification phase contrast video microscopy (100 X) of wild-type bacteria (PMSS1) in a gel-like solution of PGM at 30 mg mL^{-1} shows that a helical bacterium may generate sufficient propulsion to escape its gel-like environment (see Video 3). In contrast, a representative video of the straight rod mutant (PMSS1 Δ*csd6*) suspended in a gel-like solution of PGM at 30 mg mL^{-1}, shows a straight rod cell wiggling its body attempting to escape its viscous environment, but does not succeed (see Video 4). Thus, helical cell shape may enhance *H. pylori's* propulsion through different viscous environments.

Loss of helical morphology does not alter temporal speed variation, cell reversals, or track linearity

We utilized the cell trajectory data of the two wild-type and isogenic Δ*csd6* straight rod mutant strains to investigate whether other motility parameters were affected by perturbation of helical cell morphology. Analysis of the speed standard deviations of individual bacterial cells, σ_{bac}, indicated that the variation in swimming speed over time was similar between the Δ*csd6* mutants and their respective wild-type parental strains in PGM at 15 mg mL^{-1} (Fig. 2.8E,F) and in broth or PGM at 30 mg mL^{-1} (Fig. 2.11). We did not observe differences in reversal frequency between wild-type strains and their respective isogenic straight rod mutants in broth or viscous PGM or MC media (Fig. 2.12A,B). We also calculated the ratios of median forward swimming speed to median reversal swimming speed for individual bacterial cells that reversed and maintained at least 3 instantaneous forward or reversal speed values while swimming. We did not observe any significant differences in the ratios acquired for wild-type strains and their respective isogenic straight rod mutants in any of the solutions tested (Fig. 2.12C and data not shown). All strains exhibited relatively similar median ratios, close to 1 (Fig. 2.12C).

Finally, we examined percent track linearity (%TL) as a measure of cell path trajectory. Wild-type *H. pylori* strains showed more continuous straight runs in viscous solutions of PGM compared to broth (Fig. 2.13A), as previously described (Celli *et al.*, 2009). We did not observe any differences in %TL between wild-type strains and their respective isogenic straight rod mutants in broth and in viscous PGM or MC media (Fig. 2.13B,C, and Table 2.7). Thus, while wild-type *H. pylori* strains show increased %TL in their swimming trajectories in viscous solutions of PGM, this increase in % TL does not require helical cell shape. Our results indicate that while loss of helical cell shape reduces the swimming speed of *H. pylori*, helicity does not influence any other measured aspect of motility.

DISCUSSION

While variation in cell morphologic parameters among strains and between species have long been noted, our studies provide an in-depth, quantitative analysis of *H. pylori's* natural variation in helical cell and flagellum morphology, and how these parameters impact *H. pylori's* motility in viscous environments. Most of the previous studies of *H. pylori* motility provide numbers for only the average or maximum speed. Given the wide distribution of speeds we suggest that conclusions based only on the variation of a single speed parameter with varying external conditions could be misleading as the shape of these broad, asymmetric distributions is not fully described by a single parameter such as the average, thus higher moments of the distribution are required to describe the shape of an asymmetric distribution. Our motility studies of three unrelated wild-type *H. pylori* strains in broth and viscous solutions of PGM reveal that swimming speed distributions reflect both temporal variation in the speed of individual bacteria (Fig. 2.5) and morphological variation within the population (Fig. 2.2).

The observed broad distribution of swimming speeds was found to be largely due to temporal variation in swimming speed, which we characterized using the distribution of individual bacterium's standard deviation in speed, σ_{bac} (Fig. 2.5D and Fig. 2.6). Wild-type strains exhibited temporal variation that was dependent on their swimming environment, however loss of helical cell shape did not affect how individual bacteria vary their swimming speed with time. Our data suggest temporal speed variation is not influenced by morphology, but can be influenced by bacterium-medium interactions, and may reflect speed fluctuations due to flagellar bundling-unbundling events and/or the stochastic behavior in motor activity.

The speed distributions also vary depending on which polymer solution (and at what concentration) the bacteria swims in. Of particular interest is the observation that compared to broth, *H. pylori's* swimming speeds are slightly higher in PGM at both physiologically relevant concentrations; the higher mucin concentration corresponding to that in the mucus close to the epithelial surface, and the lower mucin concentration similar to that in the luminal layer. We observed a non-monotonic variation in *H. pylori* swimming speed and increased proportions of immobile bacteria as the viscosity of PGM increased (Table 2.4 and Fig. 2.10). Caldara *et al*. observed a similar behavior in *Pseudomonas aeruginosa*, where bacteria displayed increased swimming speeds in PGM (although at lower PGM concentrations) (Caldara *et al.*, 2012). Yeung *et al.* found that addition of mucin at physiological concentrations promoted the ability of *P. aeruginosa* to exhibit rapid motility across the surface of agar (Yeung *et al.*, 2012). The physical mechanism responsible for the increase in motility of *H. pylori* in viscous PGM solutions is unclear. Possible factors may relate to molecular interactions of bacteria with mucin and the viscoelastic nature of mucin solutions. Recent studies suggest *H. pylori* may directly bind mucins and glycolipids in gastric mucus (Naughton *et al.*, 2013), and there is a growing body of theoretical work exploring how polymer viscoelasticity alters bacterial swimming (Lauga & Powers, 2009).

In methylcellulose, we observed an increase in swimming speed, at a viscosity of 26 cP, followed by a decrease at a higher viscosity of 76 cP (Table 2.3). This non-monotonic behavior agrees with previous *H. pylori* motility studies in methylcellulose (Worku *et al.*, 1999), along with other studies of bacteria in viscous polymer solutions (Shoesmith 1960; Schneider and

Doetsch, 1974; Greenberg and Canale-Parola, 1977b; Ferrero and Lee, 1988). Recent work by Martinez *et al.* suggests that non-monotonic behavior may be caused by non-Newtonian shear thinning effects at the flagellum, thus causing flagella to experience a lower effective viscosity than the cell body (Martinez *et al.*, 2014). We did not probe the length and time scales at which flagella interact with the polymer environment in this study and leave quantifying the shear thinning effects of gastric mucin and methylcellulose on *H. pylori* motility for future work.

To directly address the impact of *H. pylori's* helical cell body shape on motility, we examined the swimming speeds of isogenic straight rod mutants that had similar flagellum length and number to wild-type bacteria. In PGM solutions, which best mimic the different rheological environments *H. pylori* experiences in the stomach, we observed an 8-13% increase in speed of helical bacteria compared to straight rods (Table 2.3). We also observed that helical cell shape increased the fraction of motile bacteria (Fig. 2.10). This effect was most pronounced in PGM concentrations that resemble the mucin concentrations found in the outer mucus layer which *H. pylori* must quickly penetrate to escape from the acidic lumen.

The effect of helical shape on motility has been explored in Spirochete bacteria that have periplasmic flagella and utilize a running wave mode of translational motility distinct from that used by bacteria with external flagella (Dombrowski *et al.*, 2009; Charon *et al.*, 2012). Spontaneous mutants of *Spirochaeta halophila* that retain flagella but have lost helical cell morphology show decreases in maximal swimming velocity and a lower minimum immobilizing viscosity (MIV) (Greenberg and Canale-Parola, 1977a). Interestingly, this study also explored the behavior of related strains and species that varied in their helical parameters, characterized as having "tight" or "loose" coils. While they did not observe a correlation between helical pitch and maximum velocity or the viscosity at which maximum velocity occurred, they observed marked variation in the MIV (300-1,000 cP) among strains with "tight" coils having the highest MIV. While helical parameters were not precisely quantified, their results appear consistent with our observations that helical cell shape provides a similar increase in swimming speed regardless of the viscosity of the medium or the helical pitch angle of the parent strain, as well as a more pronounced effect of helical morphology on the percent of immobile bacteria.

Recently Liu *et al.* observed that *Caulobacter crescentus*, a bacteria with crescent cell shape and external flagella, enhances its motility by precessing its crescent cell body in a helical trajectory (Liu *et al.*, 2014). Although *C. crescentus* bacteria have a different cell body geometry compared to *H. pylori*, their findings are consistent with our observations that the shape of the cell body can enhance flagellar-mediated motility. Overall, our findings on the effect of helical cell shape on *H. pylori's* motility add to a growing consensus that bacterial cell shape may play a larger role in motility than previously thought.

EXPERIMENTAL PROCEDURES

Bacterial strains and culture conditions

Strains used in this study are described in Table 2.1. We used three unrelated wild-type *H. pylori* strains: LSH100, a derivative of the sequenced human clinical isolate G27 (Baltrus *et al.*, 2009; Lowenthal *et al.*, 2009); PMSS1, also called 10700 (Lee *et al.*, 1997, Arnold *et al.*, 2011); and B128 (McClain *et al.*, 2009) and mutant derivatives of these strains. Bacteria were cultured on horse blood plates or in liquid media containing 90% (v/v) Brucella broth (BD Biosciences) and 10% fetal bovine serum (GIBCO) (BB10) in the absence of antimicrobials as previously described (Sycuro *et al.*, 2010). Cells were maintained at 37^{o}C under microaerobic conditions in a tri-gas incubator equilibrated to 10% CO_2 and 10% O_2. Plates were incubated 24-72 hours and liquid cultures were incubated for 12-16 hours under constant agitation at 200 rpm. For resistance marker selection, horse blood plates were supplemented with chloramphenicol (15 μg mL^{-1}).

Morphology analysis

Wild-type *H. pylori* B128, LSH100, and PMSS1 were grown in liquid culture to an optical density at 600 nm ($O.D._{(600)}$) of 0.3-0.7. Bacteria were fixed (4% Paraformaldehyde, 1X PBS, and 25% Glycerol) and added to 0.1% poly-L-lysine (Sigma Aldrich) coated coverslips that were placed on a pre-cleaned microscope slide, and were then sealed with VaLP (1:1:1 Vaseline: Lanolin: Paraffin). Single focal plane images were collected using a 100 X ELWD Plan APO (NA 1.40 oil) objective mounted on a Nikon TE 200 microscope, equipped with a Nikon CoolSNAP HQ CCD camera controlled by MetaMorph software (MDS Analytical Technologies). Quantitative morphology analysis of manually thresholded phase-contrast images was performed as described in Sycuro *et al.* using the CellTool software program (Lacayo *et al.*, 2007; Pincus and Theriot, 2007; Sycuro *et al.*, 2010). Centerline data for each strain was obtained from CellTool, imported to MATLAB, and fitted to a generalized sine curve, $y = R\sin(\frac{2\pi}{P}x + \delta)$, where *R* and *P* represent the helical radius and helical pitch, respectively, and δ is a phase term added to allow for an arbitrary origin of the sine function. Cells with non-helical morphologies resulted in poor fitting, characterized by a large sum of squared error (SSE > 0.2), and were removed from our data sets. The number of cells used to generate cell shape models were LSH100, n=262; PMSS1, n=215; and B128; n=272.

Transmission Electron Microscopy (TEM) and Scanning Electron Microscopy (SEM) of H. pylori cells

TEM of *H. pylori* was performed as described in Lowenthal *et al*., 2009, and cells were visualized with a JEOL JEM 1400 transmission electron microscope. SEM of *H. pylori* was performed as described in Sycuro *et al*., 2013. Digital images were manipulated using Image J and Adobe Photoshop.

H. pylori flagellum length measurements and flagellum number counts

Flagellum number counts were acquired from SEM images of LSH100 and PMSS1 and their respective straight rod mutants. The number of flagellum was counted from 83 - 110 different bacteria per strain. Flagellum length measurements were acquired from TEM images collected from the same preparation for all strains. TEM images were uploaded to Image J and calibrated using the scale bar (1 µm) of images acquired at 2500 - 3000 X. Using the segmented line selection tool, flagellum length was measured for one flagellum per cell, four times each, from 15 different bacteria per strain to provide average lengths and standard deviations from the means.

Generation of knockout isogenic mutants

An isogenic mutant of *csd6* (HPG27_477) in the PMSS1 strain background was generated by transfer of the mutation constructed in the LSH100 strain background (Sycuro *et al*., 2013) using natural transformation (Wang *et al.*, 1993). Transformants were confirmed by PCR using primers homologous to upstream and downstream flanking regions for each gene using the primers indicated in Table 2.6. The mutation was then backcrossed into PMSS1 once by isolating genomic DNA from the resulting strain for natural transformation of PMSS1. The resulting backcrossed clones were evaluated by PCR to confirm replacement of the wild-type allele with the null allele (*csd6*). Clones were checked for urease activity and motility, and single clones were used for quantitative morphology analyses and the motility studies. An isogenic mutant of *motB* (HPG27_772) was constructed in the LSH100 strain background as described above. Genomic DNA of *motB* bearing a transposon insertion was acquired from the mutant library generated in *H. pylori* G27 (Salama *et al.*, 2004) and was used for natural transformation of LSH100.

Preparation of purified PGM

PGM was isolated from mucosal scrapings of pig stomach epithelium and purified by Sepharose CL-2B column chromatography followed by density gradient ultracentrifugation as described in (Celli *et al.*, 2009). Lyophilized PGM powder was allowed to reach room temperature before opening tubes to avoid condensation. The powder was weighed and 7.5 mg was dissolved in 400 μL of sterile H_2O to prepare a 15 mg mL^{-1} solution with bacteria, and 15 mg was dissolved in 800 μL of sterile H_2O to prepare a 30 mg mL^{-1} solution with bacteria. PGM was allowed to hydrate and equilibrate for 48 hours at 4^oC before use.

Preparation of methylcellulose

Stock solutions of methylcellulose (MC) from Sigma Aldrich (M0261) were prepared by making 20 mg mL^{-1} (wt/vol) solutions in sterile H_2O, where the mixture was slowly agitated overnight at room temperature using a tube rotator. The approximate viscosity of a 20 mg mL^{-1} MC solution was 400 cP (approximate molecular weight, 41,000, Sigma Aldrich, M 0262).

Measuring the viscosity of broth and viscous media by particle-tracking microrheology

Fluorescent polystyrene latex beads (1.001 +/- 0.01 μm diameter) (Polysciences Inc.) were added to broth or viscous PGM or MC sample to provide a final bead concentration of 0.05% beads by volume in a final volume of 1 mL. Flagellated but non-motile bacteria (LSH100 Δ*motB*) (bacteria that do not show motion and lack the ability to swim) were grown in liquid broth (BB10) at an O.D. $_{(600)}$ of 0.3 - 0.7. Bacteria was added to each solution to produce a 10% bacteria mixture by volume, and bacteria were examined after 45 min of incubation in each solution at 37°C under microaerobic conditions. A 10 μL volume of bead or bacteria solution was then pipetted onto a glass slide with a secure spacer (Secure-Seal, Sigma-Aldrich) and covered with a coverslip. Samples were imaged using an Olympus IX 70 microscope (40 X Plan N, 0.45 NA) with QCAM CCD camera (Qimaging) at 20 frames per second (fps) and 0.2312 μm pixel size. Fluorescent beads were excited using an Olympus BH2 Mercury arc source while bacteria were imaged using phase contrast with light from a halogen bulb. Focus was set to the center and middle Z-positions of the sample in order to minimize edge effects. Videos were captured at 30 second intervals using Micro-Manager open source acquisition software (Stuurman *et al.*, 2010) and were analyzed in MATLAB v7.12.0 using a particle-tracking routine that finds the center of intensity of each bead or bacterium using a polynomial Gaussian fit (Rogers *et al.*, 2007). Beads or bacterium that drifted were dedrifted using a custom MATLAB routine and superfluous tracked objects were removed.

Motility assay in purified PGM and methylcellulose solutions

Bacteria were grown in liquid culture broth to an O.D. $_{(600)}$ of 0.5 - 0.7 and kept warm at 37°C under microaerobic conditions until use. 10 μL of culture was added to 80 μL of PGM solution and 10 μL of pH 6 buffer (0.1 M phosphate-succinate) to produce a 10% bacteria mixture by volume and the final PGM concentrations used were 15 mg mL^{-1} and 30 mg mL^{-1}. For methylcellulose solutions, 10 μL of culture was added to a solution that consisted of 50 μL of MC stock solution (20 mg mL^{-1}) and 40 μL of pH 6 buffer (0.1 M phosphate-succinate), to produce a 10% bacteria mixture by volume and a final concentration of MC at 10 mg mL^{-1}. To produce a 10% bacteria mixture by volume and a final concentration of MC at 15 mg mL^{-1}, 10 μL of culture was added to 75 μL of MC solution (20 mg mL^{-1}) and 15 μL of pH 6 buffer (0.1 M phosphate-succinate). Bacteria were incubated for 45 min in their respective PGM or MC solutions at 37^{o}C under microaerobic conditions prior to imaging. After the incubation period, each cell suspension was mixed by gentle pipetting and 10 μL was applied to standard glass microscope slides with secure imaging spacers (9 mm in diameter × 0.12 mm depth, Secure-Seal, Sigma-Aldrich). A coverslip was placed over the sample and was securely sealed. Samples were immediately imaged at room temperature using a Nikon TE 200 inverted microscope (60 X ELWD Plan Fluor, 0.7 NA Phase lens, depth field of ~5 μm) and ten second videos were captured for bacteria swimming in the mid-level plane between the coverslip and glass slide, which is ~60 μm in depth, using a Nikon CoolSNAP HQ CCD camera (100 millisecond intervals over a 10 second period (10 frames per second (fps), 0.109 μm/pixel) and MetaMorph software (MDS Analytical Technologies). Bacteria were tracked using the Volocity software (v6.1) (Volocity, Improvision, Perkin Elmer, 2011). The supplemental videos (Videos 1 and 2) accompanying this thesis were collected using a 60 X objective lens at 100 millisecond intervals over a 10 second period (10 fps). Videos 3 and 4 were collected using an 100 X oil objective lens at 300 millisecond intervals over a 30 second period (10 fps).

Tracking of swimming bacteria using Volocity (v6.1)

Videos were processed and converted to 8-bit files using ImageJ (Rasband, W.S.; ImageJ, http://imagej.nih.gov/ij/) and uploaded to the particle-tracking program in Volocity v6.1 to generate tracks based on the centroid position of each object identified (area, 0.05 - 8.0 μm^2). Individual trajectories were obtained for at least 10 frames of the video (1 second) (see Fig. 2.3). Bacteria showing a displacement less than 0.3 μm or a mean squared displacement (MSD) less than 0.1 μm^2 were considered to be immobile and were removed. Individual trajectories of 100 bacteria were acquired, examined visually to ensure accuracy, and imported into MATLAB v7.12.0 for smoothing using a five point Savitsky-Golay filter to remove noise effects caused by wiggling trajectories (Hyon *et al.*, 2012) and finite tracking resolution (Son *et al.*, 2013). Stops, reorientations, swimming speeds, and reversal events were segmented and were used to describe *H. pylori* motion.

Analysis of the fraction of immobile bacteria in broth and viscous PGM media

Videos gathered for tracking individual bacterial cells for velocity analysis were used to determine the fraction of motile and immobilized bacteria in broth and viscous PGM media. We classified all bacteria with displacements less than 0.3 μm as immobile (bacteria stuck in the medium) and bacteria with displacements greater than 0.3 μm as motile. The percentage of immobilized bacteria was calculated by dividing the total number of immobilized cells by the total number of bacterial cells. The total bacterial population included immobilized bacteria and motile bacteria (bacteria with displacements between 0.3 – 1.5 μm, and bacteria with displacements > 1.5 μm that were processed through MATLAB and segmented to acquire swimming speeds after tracking by Volocity).

Statistical analysis

We used the Kolmogorov-Smirnov (K-S) statistics tool in CellTool to assay differences in cell shape morphology, including cell length and side curvature distributions, as described in detail in Sycuro *et al*., 2010 and 2012. Statistical comparisons between wild-type helical radius, helical pitch, and pitch angle distributions were done using unpaired nonparametric Kolmogorov-Smirnov (K-S) tests in MATLAB v7.12.0. To make statistical comparisons between wild-type vs. mutant instantaneous speed distributions; cell path trajectories; frequency of reversals; and the ratios of forward and reversal swimming speeds; unpaired nonparametric Kolmogorov-Smirnov (K-S) tests were performed using GraphPad Prism version 6.00 for Windows (GraphPad Software, La Jolla, CA USA). For each comparison, a K-S p-value < 0.05 was considered significant.

TABLES

Table 2.1. Bacterial strains used in this chapter.

Strain Name	Genotype or Description	Shape phenotype	Reference or Source
LSH100	Wild-type *H. pylori*, NSH57 *fliM* mutation repaired	helical	Lowenthal *et al*., 2009
B128	Wild-type *H. pylori*	helical	McClain *et al*., 2009
PMSS1	Wild-type *H. pylori*	helical	Lee *et al*., 1997; Arnold *et al*., 2011
TSH17	Δ*csd6::cat* in LSH100	straight	Sycuro *et al*., 2013
LMH6	Δ*csd6::cat* in PMSS1	straight	This study
LMH9	Δ*motB::tn* in LSH100	helical	Salama *et al*., 2004; This study

Table 2.2. Average cell body and helical parameters of wild-type *H. pylori* strains.

Strain	**Average cell body parameters from CellTool**[a]				**Average helical parameters**[b]		
	n	**Cell length (µm)**	**Side Curvature**	**Cell diameter (µm)**	**n**	**Helical radius (µm)**	**Helical pitch (µm)**
LSH100	282	3.17	5.26	0.55	262	0.22	2.3
B128	274	2.82	3.08	0.58	272	0.10	2.4
PMSS1	222	3.33	3.10	0.57	215	0.14	2.8

[a] Cell body parameters acquired from CellTool.

[b] Helical parameter measurements acquired from fitting centerlines to a sinusoid.

Table 2.3. Speeds for wild-type bacteria and straight rod mutants swimming in broth and viscous media.

Solution	Strain		n	Inst. values	v_{avg} (µm/s)	v_m (µm/s)	v_{max} (µm/s)	σ	K-S p-value[c]	% reduction to v_m relative to WT
BB10		**B128**	99	2105	6.6	5.5	28.0	4.3		
	LSH100	**WT**	100	2538	6.8	5.7	48.0	4.7	0.0955	7%
		Δ*csd6*	100	2058	6.5	5.3	30.1	4.1		
	PMSS1	**WT**	100	1975	11.6	10.8	49.2	6.3	<0.0001	11%
		Δ*csd6*	100	1930	10.5	9.6	38.8	6.0		
PGM[a] 15 mg mL^{-1}		**B128**	100	2112	11.7	12.5	36.6	5.5		
	LSH100	**WT**	100	3325	6.7	6.5	29.1	3.8	<0.0001	11%
		Δ*csd6*	100	3886	6.2	5.8	22.8	3.6		
	PMSS1	**WT**	100	2073	11.8	12.2	39.3	5.3	<0.0001	11%
		Δ*csd6*	100	2550	10.7	10.8	28.4	3.6		
PGM 30 mg mL^{-1}		**B128**	100	2752	6.7	6.5	41.9	3.7		
	LSH100	**WT**	100	2790	6.6	6.4	30.1	4.2	0.0005	8%
		Δ*csd6*	100	2951	6.3	5.9	33.3	4.2		
	PMSS1	**WT**	100	2224	11.3	11.8	34.8	4.7	<0.0001	13%
		Δ*csd6*	100	2276	9.7	10.3	24.8	4.4		
MC[b] 10 mg mL^{-1}	**LSH100**	**WT**	100	2076	9.5	8.8	46.1	5.2	<0.0001	10%
		Δ*csd6*	100	2151	8.6	7.9	39.4	5.0		
	PMSS1	**WT**	100	1874	13.2	14.2	32.2	5.8	<0.0001	21%
		Δ*csd6*	100	2251	10.6	11.2	24.2	4.6		
MC 15 mg mL^{-1}	**LSH100**	**WT**	100	3194	5.5	4.8	26.1	3.3	<0.0001	6%
		Δ*csd6*	100	3544	5.1	4.5	16.6	2.6		
	PMSS1	**WT**	48	965	6.9	6.4	20.6	3.3	0.0104	NR[d]
		Δ*csd6*	48	1201	6.8	6.8	17.9	3.4		

[a] PGM: Purified gastric mucin at pH 6.0.

[b] MC: Methylcellulose.

[c] For K-S tests used to compare WT to mutant cumulative distributions of swimming speeds, p-values < 0.05 are considered significant.

[d] NR: No reduction.

Table 2.4. Fraction of immobile bacteria in broth and viscous PGM media.

Strain		**BB10**		**PGM[a] 15mg mL^{-1}**		**PGM 30 mg mL^{-1}**	
		n	**% immobile[b]**	**n**	**% immobile**	**n**	**% immobile**
LSH100	**WT**	977	20	536	24	820	50
	Δ*csd6*	494	21	546	30	456	52
Increase in % immobile bacteria relative to WT			5%	25%		4%	
PMSS1	**WT**	558	10	330	15	456	38
	Δ*csd6*	371	13	328	21	504	51
Increase in % immobile bacteria relative to WT			30%	40%		34%	

[a] PGM: Purified gastric mucin at pH 6.0.
[b] Bacteria that exhibit displacements $< 0.3\ \mu m$ (MSD $< 0.1\ \mu m^2$).

Table 2.5. Median flagellum parameters of wild-type *H. pylori* and isogenic straight rod mutants.

Strains	**Median flagellum parameter[a] +/- SD[b]**			
	n	**Flagellum number**	**n**	**Flagellum length (µm)**
LSH100	110	3 +/- 1	15	3.4 +/- 0.3
LSH100 Δ*csd6*	109	3 +/- 1	15	3.3 +/- 0.4
PMSS1	104	4 +/- 1	15	4.4 +/- 0.3
PMSS1 Δ*csd6*	105	4 +/- 1	15	4.2 +/- 0.2

[a] Flagellum number counts were acquired from SEM images and flagellum length measurements were acquired from TEM images.
[b] Standard Deviation (SD).

Table 2.6. Primers used in this chapter.

Targeted disruption primers			
Gene name	***H. pylori* gene annotation**	**Primer**	**Sequence**
csd6	HPG27_477[a] (HP0518)[b]	476F	gcgcgctctagAAGGAAGAAAAGAGCTTGC[c]
		478R	GCTGGTAGGCTTTGTAATC
motB	HPG27_772[a] (HP0816)[b]	771F	TCATTATCATCGTGCCTA
		773R	AAATTGGTGCTCACTTCT

[a] Gene annotation in the human clinical isolate G27 (Baltrus *et al.*, 2009).

[b] Gene annotation in the human clinical isolate 26695 (Tomb *et al.*, 1997).

[c] Gene specific sequences are in uppercase and sequences added for cloning are in lower case.

Table 2.7. Percent track linearity for wild-type bacteria and straight rods swimming in broth and viscous media.

Solution	Strain		n	Average %TL	K-S p-value[c] for %TL
BB10		**B128**	99	59%	
	LSH100	**WT**	100	54%	0.468
		Δ*csd6*	100	57%	
	PMSS1	**WT**	100	67%	0.024
		Δ*csd6*	100	60%	
PGM[a] 15 mg mL^{-1}		**B128**	100	77%	
	LSH100	**WT**	100	81%	0.281
		Δ*csd6*	100	78%	
	PMSS1	**WT**	100	89%	0.367
		Δ*csd6*	100	87%	
PGM 30 mg mL^{-1}		**B128**	100	74%	
	LSH100	**WT**	100	82%	0.581
		Δ*csd6*	100	78%	
	PMSS1	**WT**	100	83%	0.367
		Δ*csd6*	100	81%	
MC[b] 10 mg mL^{-1}	**LSH100**	**WT**	100	68%	0.581
		Δ*csd6*	100	66%	
	PMSS1	**WT**	100	81%	0.699
		Δ*csd6*	100	77%	
MC 15 mg mL^{-1}	**LSH100**	**WT**	100	56%	0.010
		Δ*csd6*	100	69%	
	PMSS1	**WT**	48	81%	0.687
		Δ*csd6*	48	76%	

[a] PGM: Purified gastric mucin at pH 6.0.

[b] MC: Methylcellulose.

[c] K-S test used to compare WT to mutant percent track linearity (%TL), p-values < 0.05 are considered significant.

FIGURES

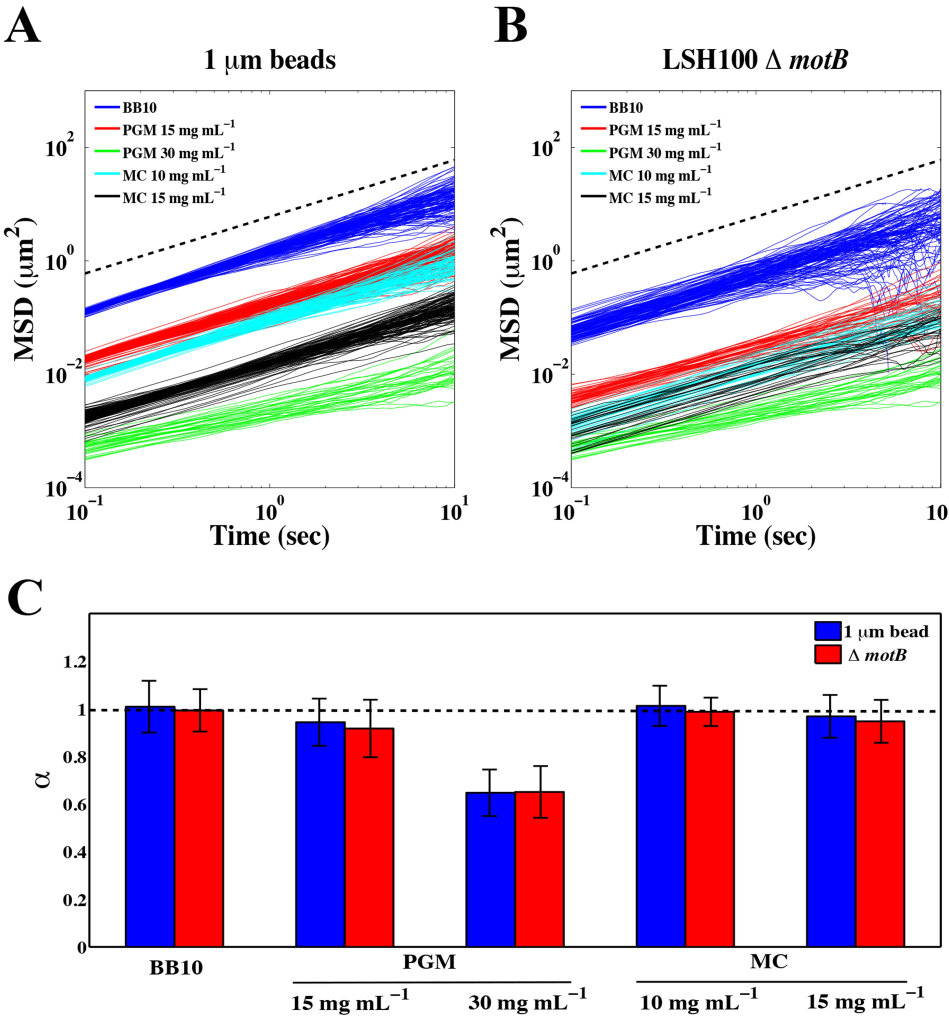

α	**1.0 +/- 0.11**	**0.94 +/- 0.1**	**0.65 +/- 0.10**	**1.01 +/- 0.09**	**0.97 +/- 0.09**
η (cP)	**1.1 +/- 0.3**	**9.0 +/- 2.0**	**1,400* +/- 210**	**26 .4 +/- 6.2**	**79 +/- 15**

Figure 2.1. Physiologic concentrations of gastric mucin exhibit solution and gel-like properties. Mean square displacement (MSD, μm^2) values as a function of time (sec) for 1 μm fluorescent particles (A) and LSH100 Δ*motB* bacteria (B) in broth (BB10), PGM (15 mg mL^{-1} and 30 mg mL^{-1}) and MC (10 mg mL^{-1} and 15 mg mL^{-1}) along with (C) Average power of law exponents (α). Average viscosity values (η, cP) and their standard deviations are summarized in the table above (see text for calculation details). All error bars represent standard error and dashed lines represent linear scaling of MSD over time (α=1). *This value is significantly larger compared to the others due to the gel-like nature of PGM at 30 mg mL^{-1}.

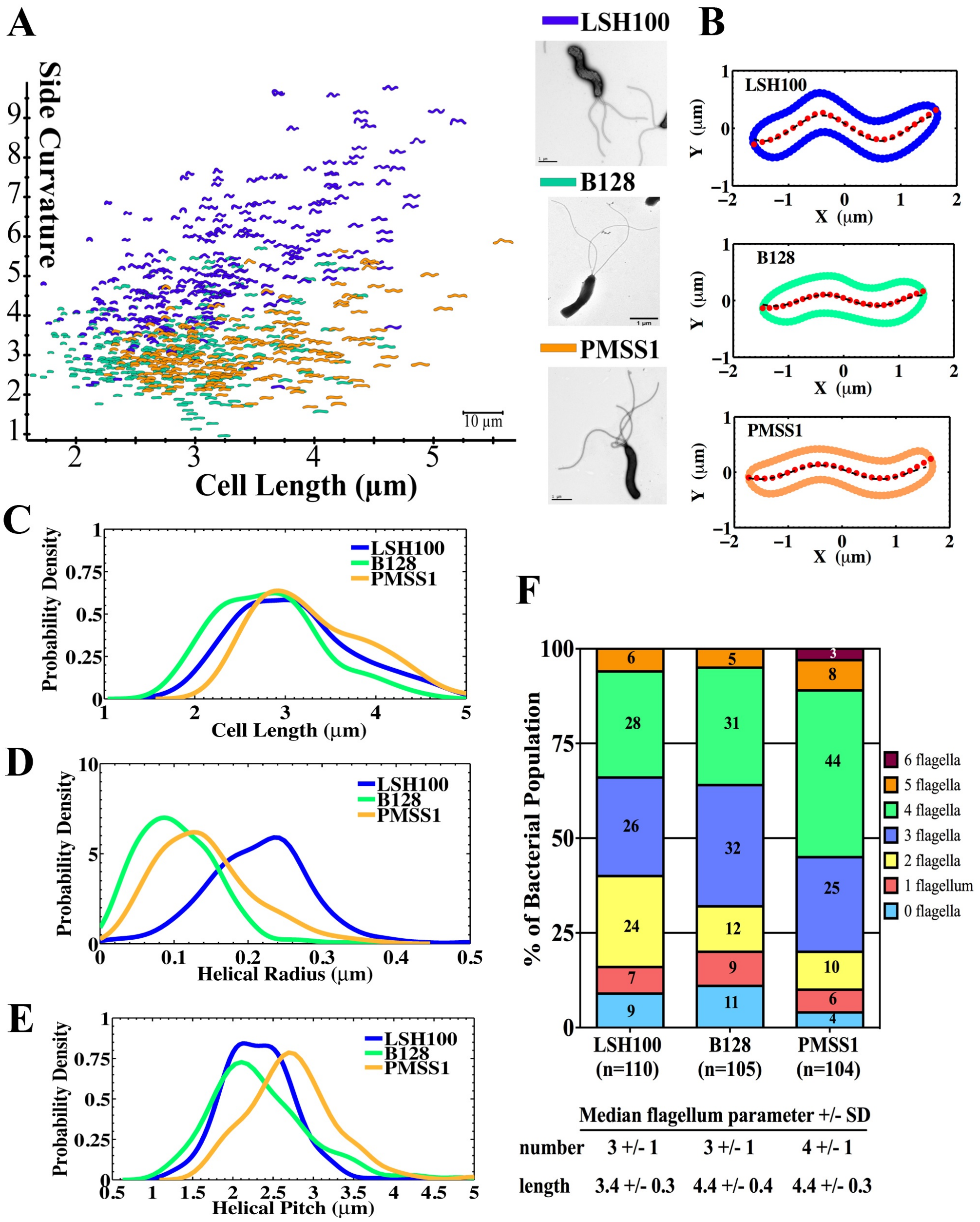

Median flagellum parameter +/- SD	LSH100	B128	PMSS1
number	3 +/- 1	3 +/- 1	4 +/- 1
length	3.4 +/- 0.3	4.4 +/- 0.4	4.4 +/- 0.3

Figure 2.2. Wild-type *H. pylori* strains display diverse cell shape and flagellum morphologies. (A) Side curvature vs. cell length (µm) for individual bacterial cells imaged using phase contrast microscopy of LSH100 (blue, n=282), B128 (green, n=274), and PMSS1 (orange, n=222) bacteria. Inset panel: TEM images of each. Scale bar = 1 µm. Data combined from two independent cultures for each strain. (B) Representative bacterial centerlines (red dots) for each wild-type strain fitted with a generalized sine function, $y = R\sin(\frac{2\pi}{P}x+\delta)$ (black dashed line); *R*, helical radius; *P,* helical pitch; δ, phase shift term (δ ≈ π for the bacteria shown). (C-E) Smooth histograms of probability density for cell length (µm) (C), helical radius (µm) (D), and helical pitch (µm) (E) of LSH100 (n=262), B128 (n=272), and PMSS1 (n=215) bacteria. (F) Flagellum number counts measured from SEM or TEM images reported as percent of the total bacterial population examined (n=104-110 bacteria).

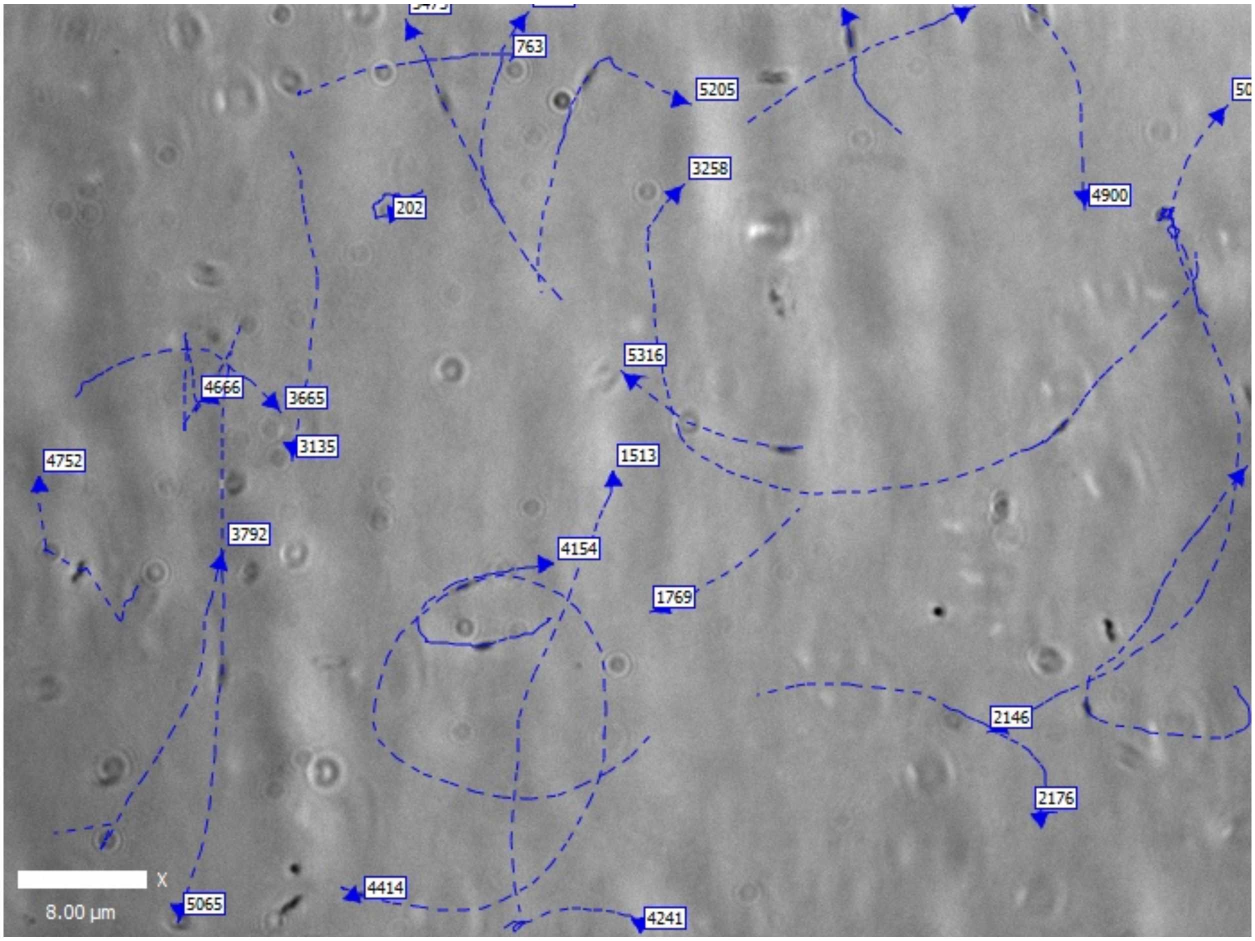

Figure 2.3. Individual cell trajectories of tracked bacteria show diverse swimming patterns. Shown is a snapshot image that was superimposed with the tracks (and track identification numbers) acquired from the entire video of individual wild-type bacteria (LSH100) tracked by live-cell video microscopy, swimming in a viscous solution of PGM at 15 mg mL^{-1}. The video was acquired at 60 X and recorded at 100 ms intervals over a 10 second period (10 frames per second). Scale bar = 8 µm. The video was then uploaded to Volocity (v6.1) to track individual bacterial cells according to size (area (µm^2)) and pixel intensity (see Experimental Procedures). Each single cell tracked was visually inspected to exclude bacteria that displayed less than 0.3 µm in displacement, and overlapping tracks for the same bacterial cell or joined tracks between bacteria were discarded. As shown, some bacteria swim in relatively straight lines, others in loose or tight curves, and some reverse direction.

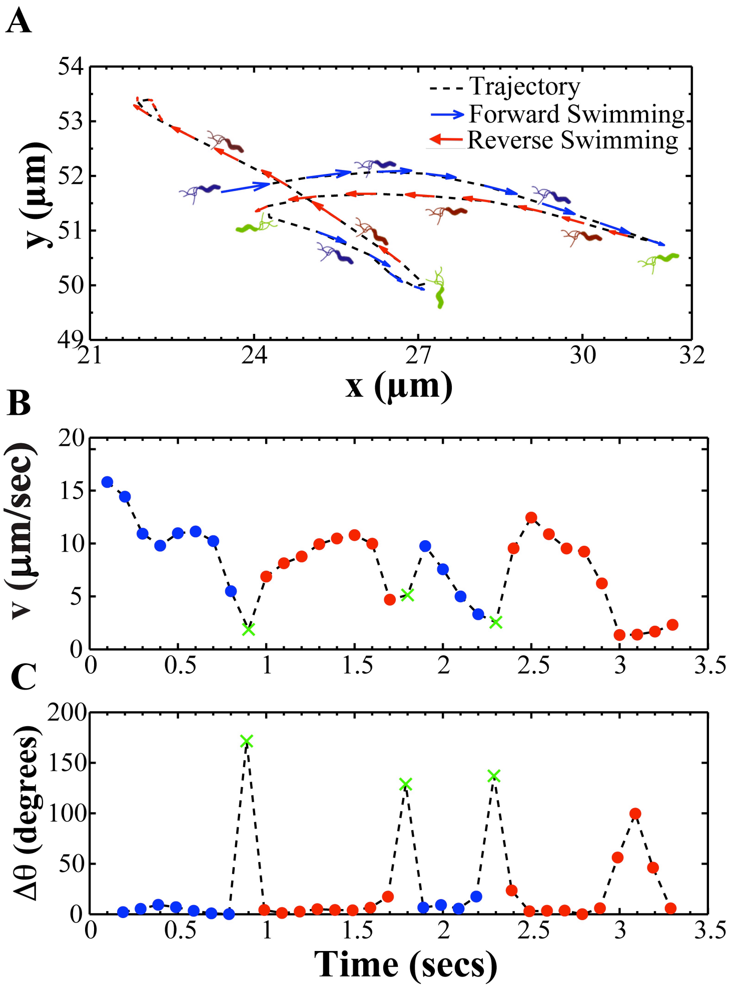

Figure 2.4. A representative bacterial trajectory depicting the swimming motion of *H. pylori.* (A) A representative bacterial trajectory of *H. pylori* is shown segmented into forward (blue) and reverse swimming directions (red). In our analysis, the direction of swimming observed at the start of the video was considered forward. A reversal in swimming direction (green) was identified when bacteria exhibited a large angle change ($\Delta\theta$) > 110 degrees. Upon a reversal, bacteria were assumed to continue swimming in the reversed direction (red) until another reversal took place. (B) Instantaneous forward and reversal swimming speeds and (C) change in swimming angle ($\Delta\theta$) of the bacterium in panel A over the course of time it was tracked (X (green) denotes reversals in swimming direction).

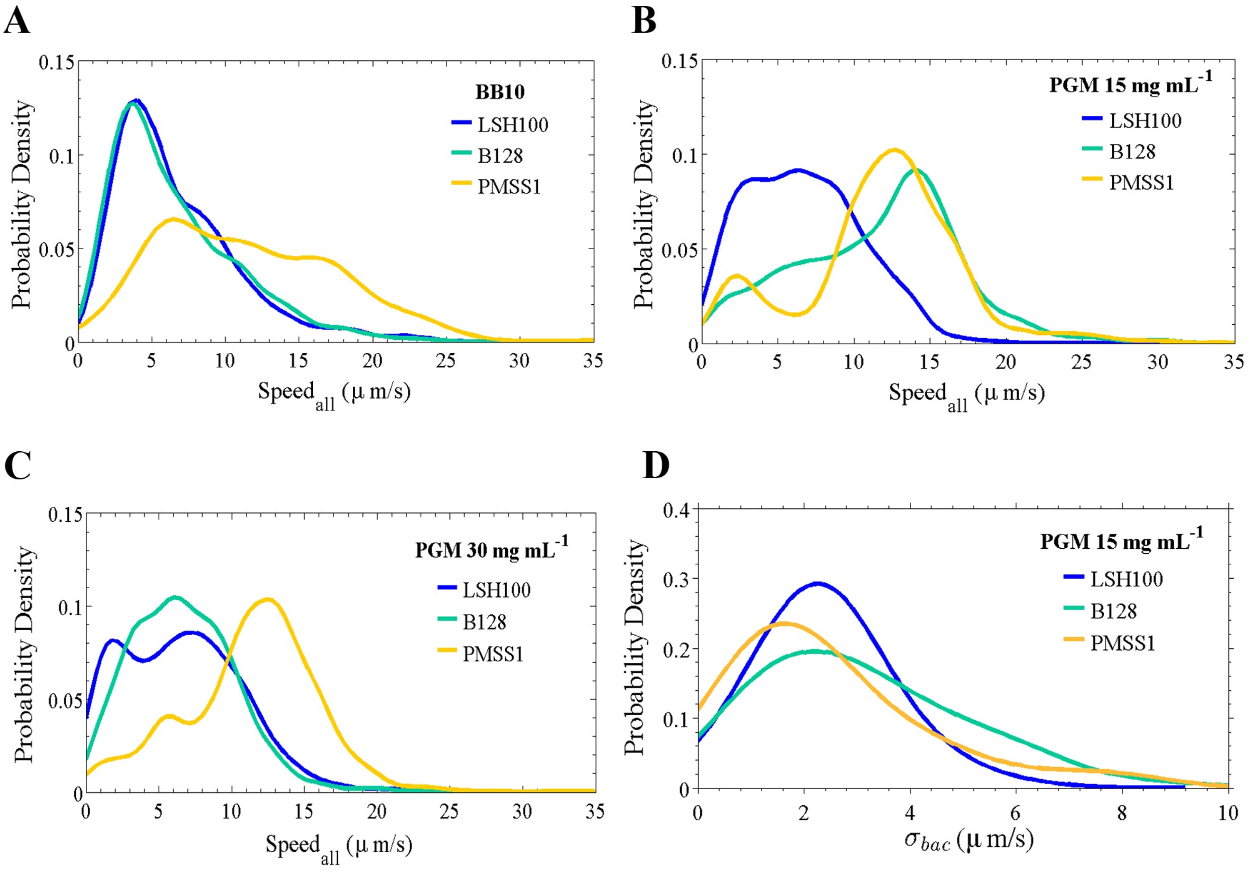

Figure 2.5. Wild-type *H. pylori* strains display diverse speed profiles and temporal variation in swimming speed. Smooth histograms summarizing speed distributions for LSH100, B128, and PMSS1 bacteria swimming in broth (BB10) (A), in viscous solutions of PGM (15 mg mL^{-1}) (B), and in gel-like PGM solutions (30 mg mL^{-1}) (C). Representative data is from one of two or three independent experiments for each strain and the median swimming speeds of each wild-type strain are summarized in Table 2.3. K-S statistics show a p-value = 0.1100 for LSH100 vs. B128 in BB10; $p < 0.0001$ for LSH100 vs. PMSS1 and B128 vs. PMSS1 in BB10; and $p < 0.0001$ for LSH100 vs. B128, LSH100 vs. PMSS1, and B128 vs. PMSS1 in viscous PGM media. (D) Smooth histograms summarizing speed standard deviation, σ_{bac}, distributions acquired for each bacterium's trajectory analyzed for LSH100, B128, and PMSS1 bacteria swimming in a viscous solution of PGM at 15 mg mL^{-1}. K-S statistics show a p-value = 0.0050 for LSH100 vs. B128; p =0.0314 for LSH100 vs. PMSS1, and p =0.0082 for B128 vs. PMSS1.

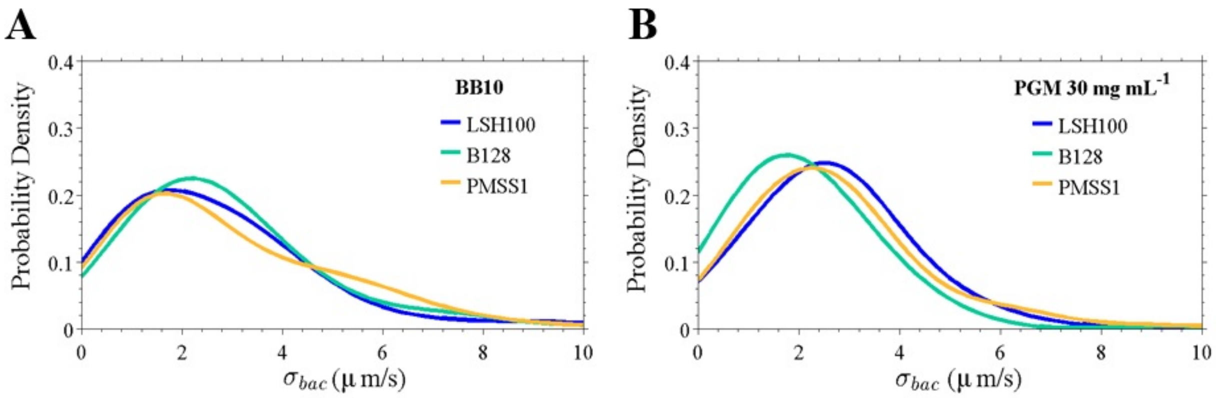

Figure 2.6. Wild-type *H. pylori* speed distributions reflect temporal variation of individual bacteria in broth and a gel-like PGM solution. (A) Smooth histograms summarizing speed standard deviation, σ_{bac}, distributions acquired for each bacterium's trajectory analyzed for LSH100, B128, and PMSS1 bacteria swimming in broth (BB10) (A) and in PGM solutions at 30 mg mL^{-1} (B). In BB10, all strains show similar distributions: LSH100 vs. B128 (K-S p=0.46), LSH100 vs. PMSS1 (K-S p=0.57), and B128 vs. PMSS1 (K-S p=0.28). In PGM at 30 mg mL^{-1}, LSH100 and PMSS1 show similar temporal speed distributions (K-S p=0.89), while B128 shows a significantly different temporal speed distribution from both strains ($p<0.05$).

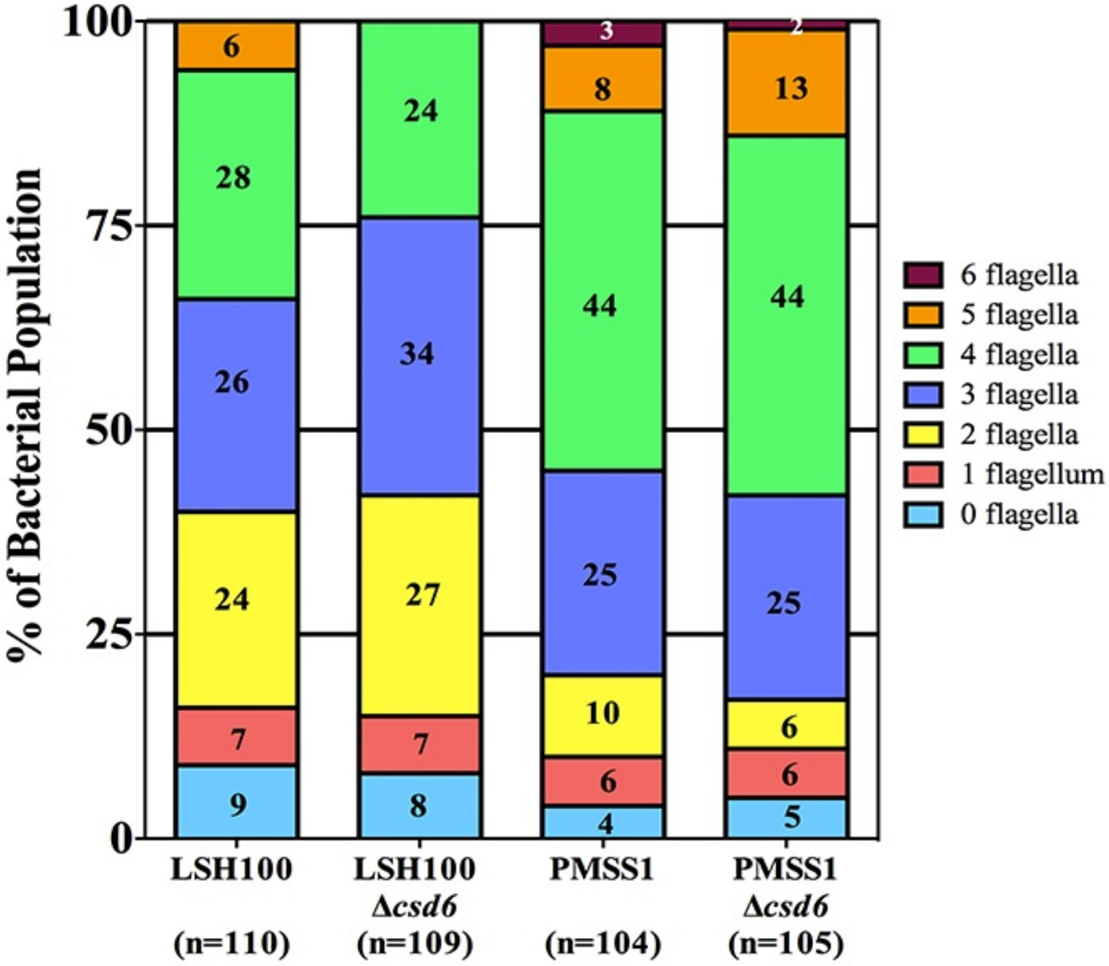

Figure 2.7. Straight rod mutants show similar flagellum parameters to wild-type *H. pylori*. Individual bacteria for wild-type LSH100 and PMSS1 and their respective isogenic straight rod mutants were analyzed for the number of flagella from TEM images and are reported as percent of the total bacterial population examined (n=104-110).

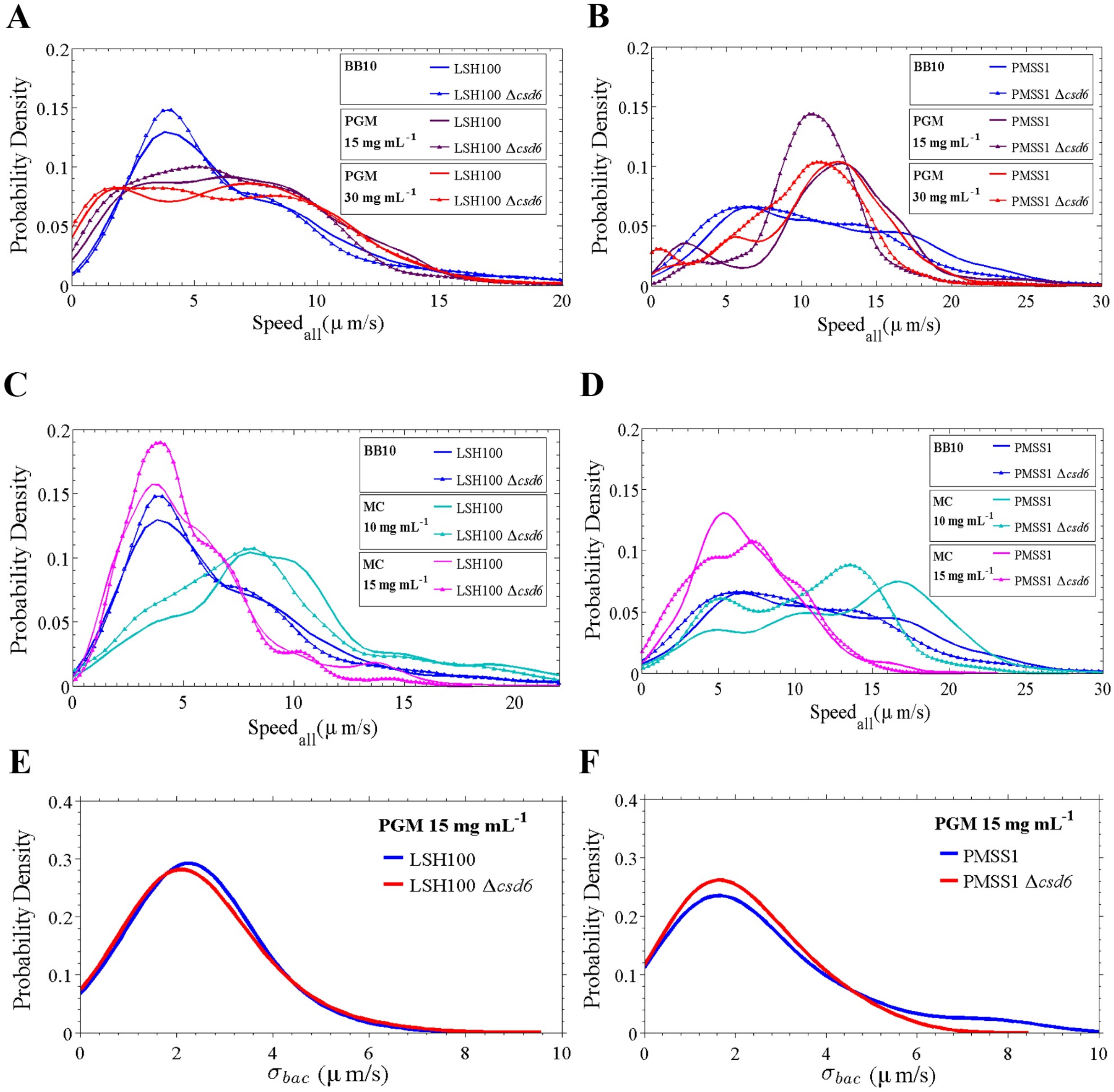

Figure 2.8. Straight rod mutants show decreased swimming speeds in broth and viscous media. Speed distributions for wild-type and Δ*csd6* isogenic straight rod mutants in broth (BB10) and viscous PGM media (15 and 30 mg mL^{-1}) (A, B), and in broth (BB10) and viscous MC media (10 and 15 mg mL^{-1}) (C, D). One of two or three independent experiments are shown. (E, F) Smooth histograms summarizing speed standard deviation, σ_{bac}, distributions acquired for each bacterium's trajectory of wild-type LSH100 (E) and PMSS1 bacteria (F) as compared to their respective isogenic straight rod mutants in viscous solutions of PGM at 15 mg mL^{-1}. The ensemble distributions show similar speed variation profiles between wild-type and straight rod mutants, where K-S p =0.44 for LSH100 vs. LSH100 Δ*csd6*, and p =0.57 for PMSS1 vs. PMSS1 Δ*csd6*.

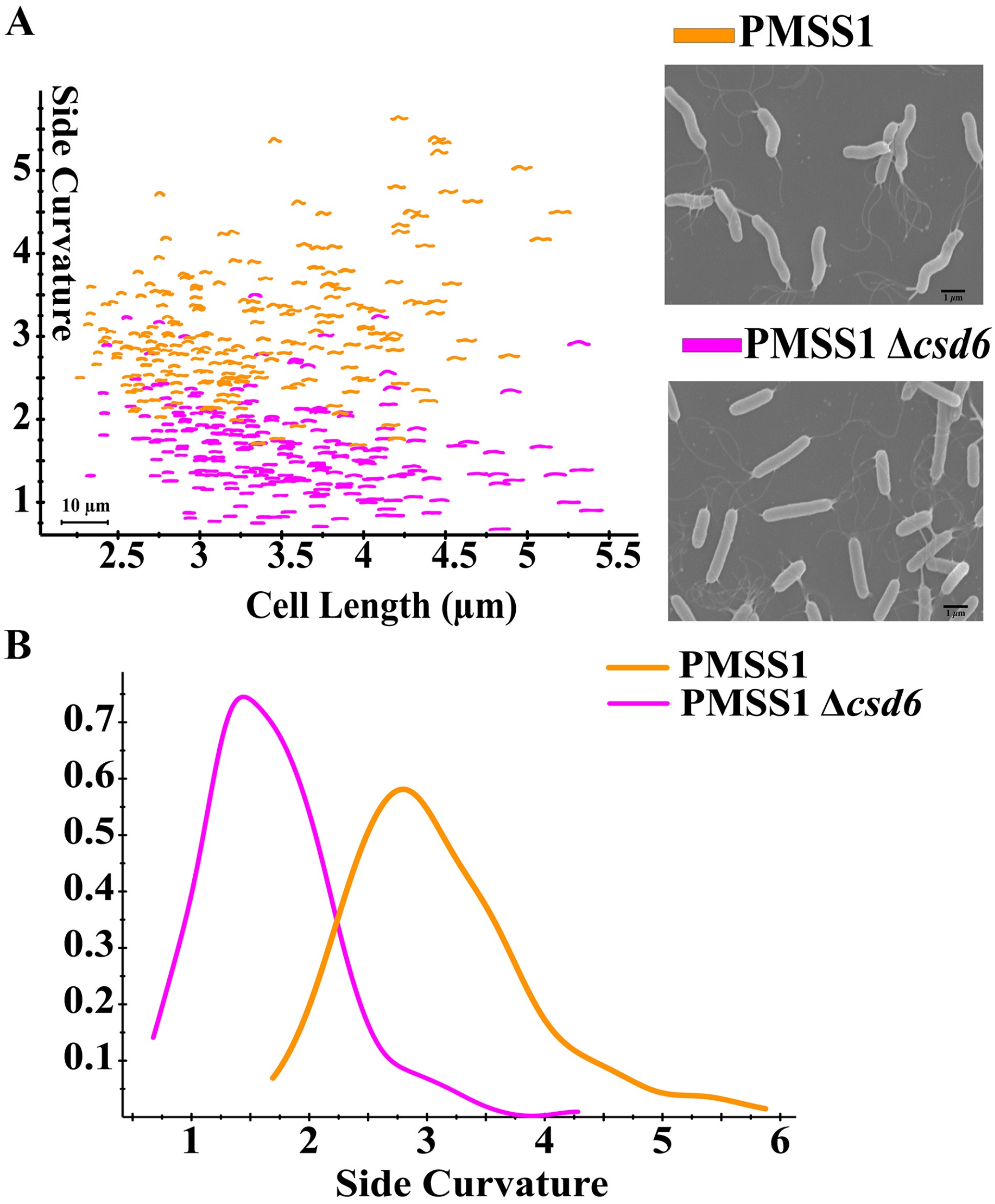

Figure 2.9. Deletion of *csd6* results in straight rod morphology in the PMSS1 strain background. (A) Scatter plot of side curvature vs. cell length (µm) for wild-type PMSS1 (n=222) and the *csd6* targeted deletion mutant generated in the PMSS1 strain background (n=228). Each point represents the outline of individual bacteria captured by phase contrast microscopy (100 X). Inset panel: SEM images of PMSS1 (top) and PMSS1 Δ*csd6* (bottom). Scale bar = 1 µm. (B) Smooth histogram of side curvature frequency distributions of the same populations shown in A. Statistical test of the Kolmogorov-Smirnov (K-S) distance shows p <0.00001 for side curvature distributions.

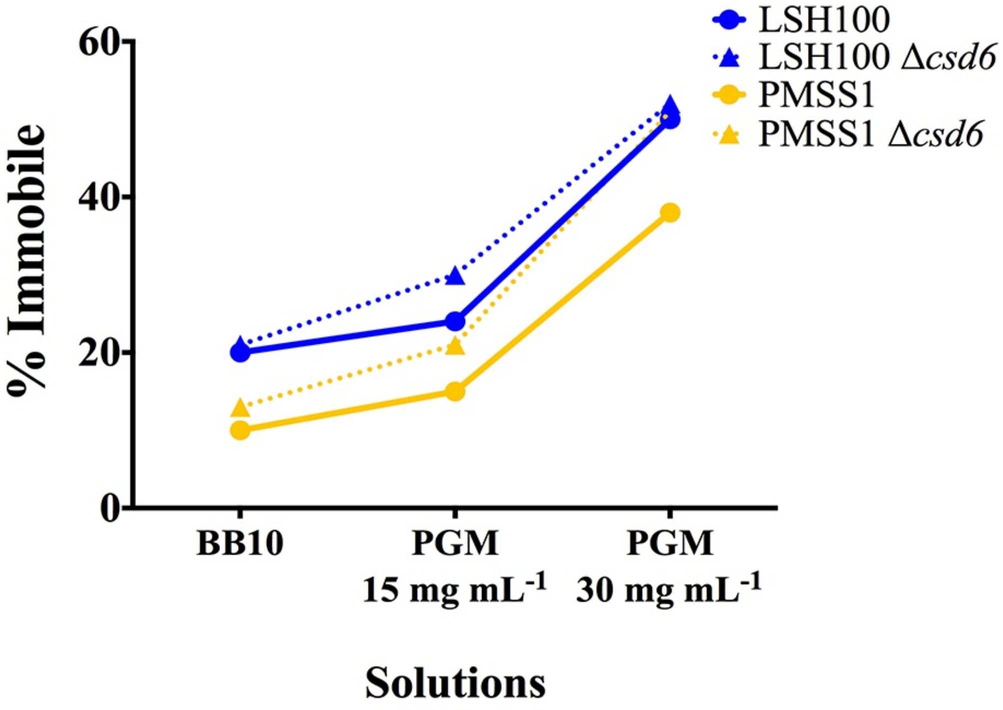

Figure 2.10. Straight rods show increased fractions of immobilized bacteria in viscous PGM media. The percentage of immobilized bacteria was calculated by dividing the total number of immobilized cells (bacteria that exhibit displacements < 0.3 μm) by the total bacterial population examined, as described in the Experimental Procedures. Data shown are from the same experiment in Figure 2.8. The percent immobilized fractions are also summarized in Table 2.4.

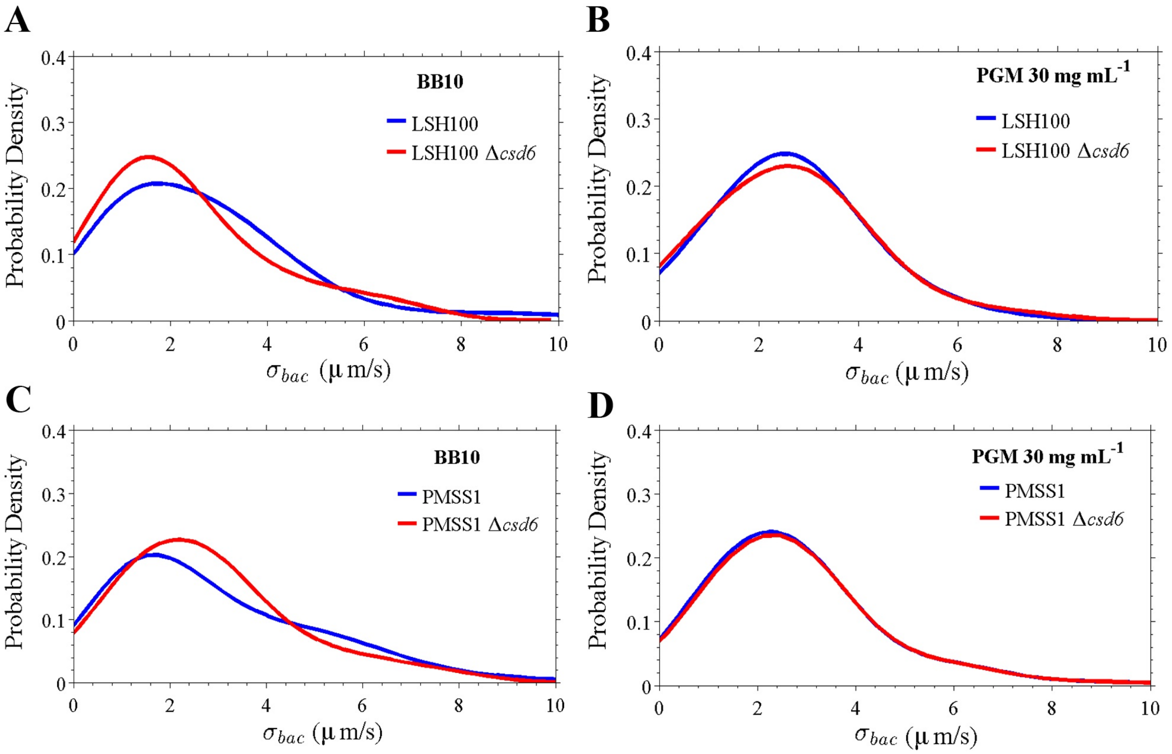

Figure 2.11. Straight rods show similar temporal variation in swimming speed to wild-type in broth and in gel-like PGM solutions. Smooth histograms summarizing speed standard deviation, σ_{bac}, distributions acquired for each bacterium's trajectory of wild-type *H. pylori* strains and isogenic Δ*csd6* straight rod mutants in LSH100 (A,B) and PMSS1 (C,D) strains in broth (BB10) and in gel-like PGM solutions at 30 mg mL^{-1}. The distributions show similar speed variation profiles between wild-type and straight rod mutants, where K-S statistics show a p-value = 0.14 (BB10) and p = 0.79 (PGM at 30 mg mL^{-1}) for LSH100 vs. LSH100 Δ*csd6*, and p = 0.34 (BB10) and p = 0.19 (PGM at 30 mg mL^{-1}) for PMSS1 vs. PMSS1 Δ*csd6*.

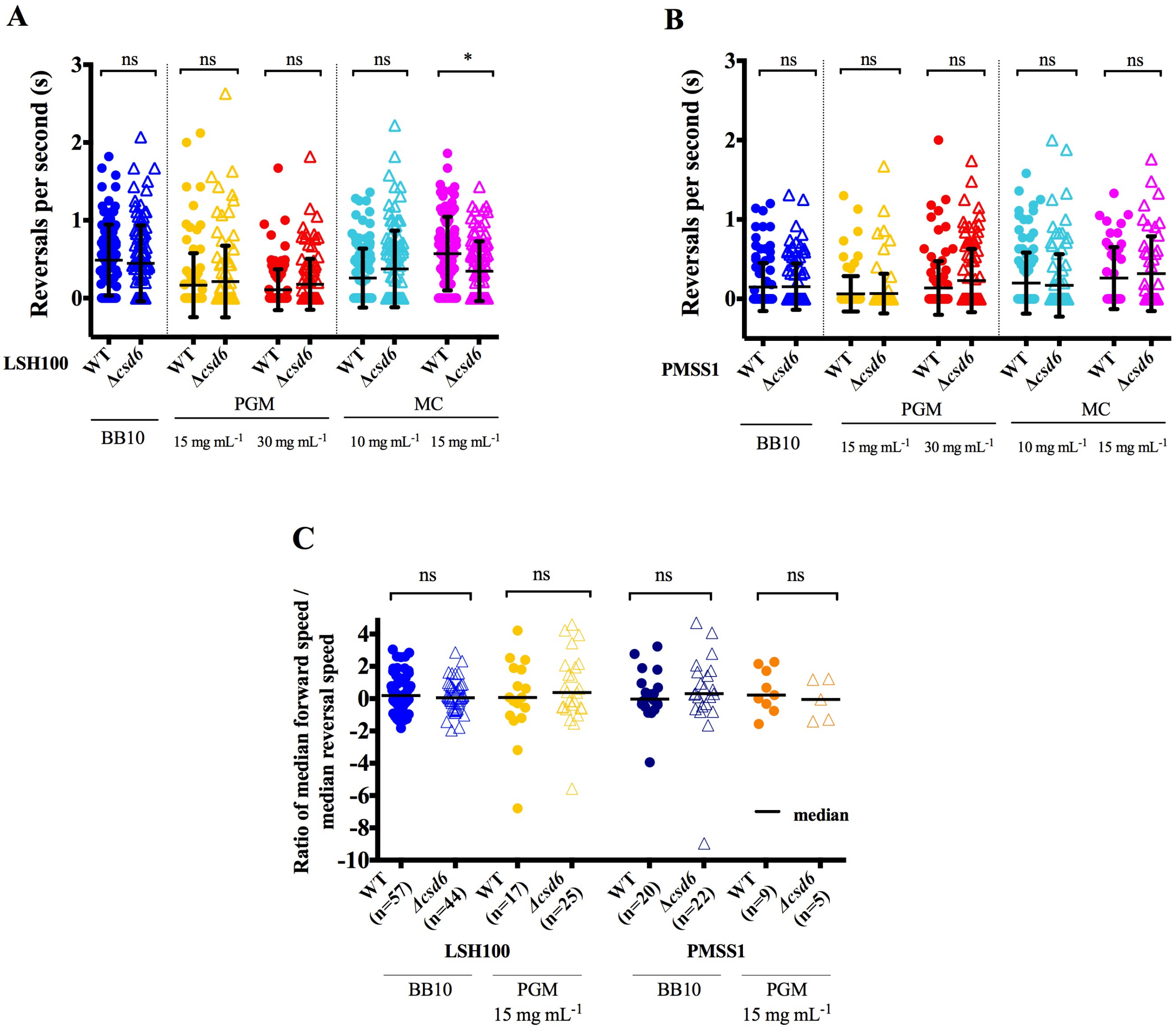

Figure 2.12. Reversal frequency and ratio of forward to reverse speed are similar across wild-type strains and shape mutants. (A, B) Dot plots summarizing the number of reversals per second of wild-type *H. pylori* strains and isogenic Δ*csd6* straight rod mutants in LSH100 (A) and PMSS1 (B) strains in broth (BB10) and in viscous PGM or MC media. Mean values of reversals per second are shown as bolded black lines and error bars indicate one standard deviation from the mean. Data shown is from one of two or three representative experiments for each strain. (C) Dot plots summarizing individual ratios of median forward swimming speed to median reversal swimming speed acquired for each bacterial cell that reversed and maintained at least 3 instantaneous forward or reversal speed values while swimming in broth or viscous PGM solutions at 15 mg mL^{-1}. Ratios are plotted on a log_2 scale and median values are shown as bolded black lines. All data shown is from the same experiment in Figure 2.8. *K-S statistics, p <0.05 was considered significant and ns = no significant difference.

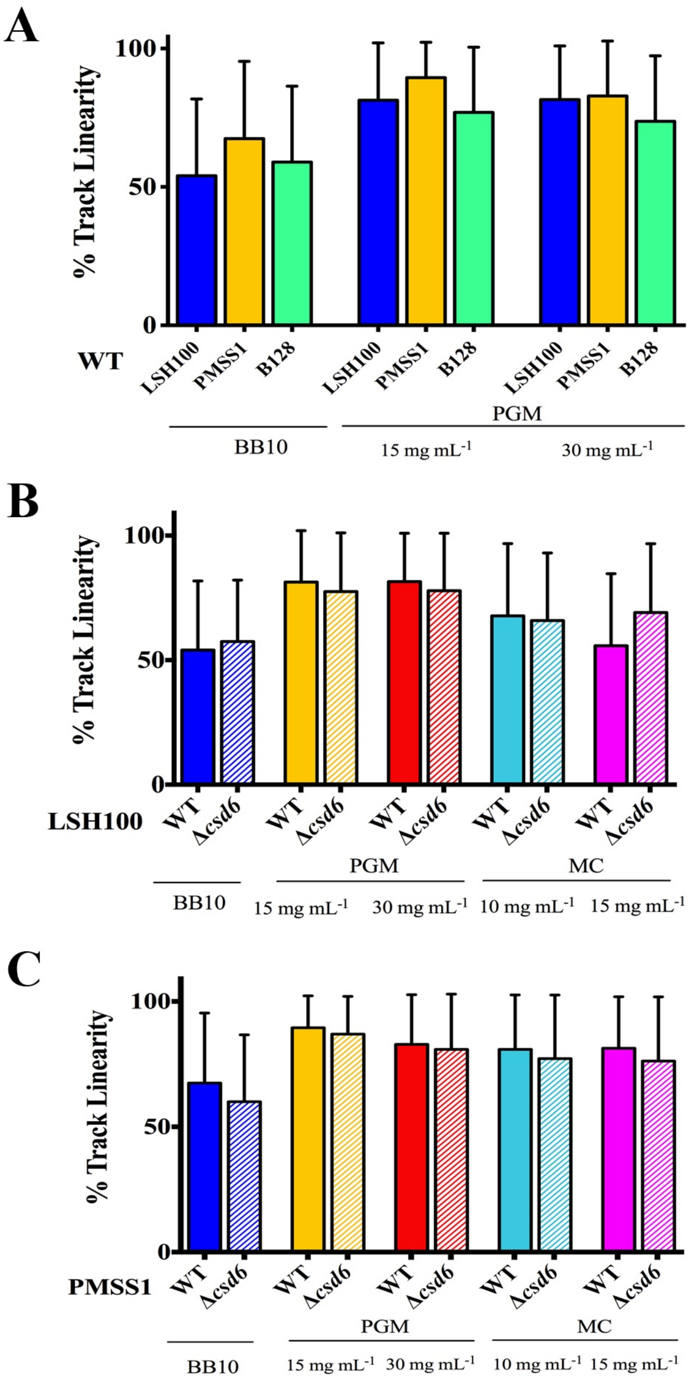

Figure 2.13. *H. pylori* show increased % track linearity in their swimming trajectories in viscous PGM media, irrespective of cell shape. Bar histograms show cell path trajectory as percent track linearity (%TL) between wild-type *H. pylori* strains (solid bars, A-C) and isogenic Δ*csd6* straight rod mutants (hashed bars, B-C) in LSH100 and PMSS1 strains, as calculated from the ratio of average straight-line velocity (μm/s) to average swimming speed (μm/s) x 100%, in broth (BB10) and in viscous PGM or MC media. Error bars represent SD and mean %TL values are summarized in Table 2.7. Data are from the same experiments shown in Figures 2.5 and 2.8.

CHAPTER 3

H. pylori varies flagellum number to maintain robust motility in viscous environments

INTRODUCTION

In Chapter 2, we characterized the effect of cell shape on *H. pylori's* motility in different viscous environments. Morphological analyses of three unrelated clinical *H. pylori* strains show inter- and intra-strain variation in helical cell morphology (cell length, helical radius, and helical pitch) (Fig. 2.2). Analysis of the three strains revealed broad swimming speed distributions that reflect both temporal variation in the speed of individual bacteria and morphological variation within the population. However, the spread in number of flagella (Fig. 2.2F) may also account for the diverse speed profiles and swimming speed differences observed between strains (Fig. 2.5). In this chapter, we elucidate the role of flagellum number on *H. pylori* swimming speed. *H. pylori* may express up to 6 flagella at one pole, and so we tested a flagellar mutant skewed to lower number of flagella (0-4) and a mutant with increased number of flagella (4-6) generated in the *H. pylori* B128 strain background. We used live-cell imaging to track individual bacteria and measured the swimming speeds of wild-type B128 and its isogenic flagellar mutants in viscous solutions of gastric mucin (see Videos 5 and 6).

RESULTS

H. pylori swimming speed correlates with flagellum number

Our studies suggest that multiple aspects of the cell body morphology of helical bacteria may influence *H. pylori* swimming speed. In addition, flagellation may contribute to the swimming speed differences observed between wild-type *H. pylori* strains, as suggested by the increased swimming speed profiles observed for PMSS1 in all media tested (Fig. 2.5). PMSS1 has a median flagellum number of 4 compared to 3 for B128 and LSH100 (Fig. 2.2F). To test the effect of flagellum number on *H. pylori* swimming speed, we utilized mutations that lead to altered flagellation in strain B128. For an isogenic strain with a reduced number of flagella, we used a $fliO_{\Delta\mathrm{C}}$ mutant which bears a C-terminal truncation in the flagella export apparatus protein FliO (Tsang & Hoover, 2014) (Table 3.1) and has a median flagellum number of 1 +/- 1 (Fig. 3.1A). For an isogenic strain with an increased number of flagella, we used a putative small non-coding RNA mutant (designated sRNA_T; locus tag HPnc7700 in *H. pylori* 26695), which has a median flagellum number of 4 +/- 1 (Fig. 3.1A). sRNA_T was identified from a transcriptome analysis of *H. pylori* 26695 and is predicted to be transcribed from a FliA-dependent promoter (Sharma *et al.*, 2010) (Table 3.1). HPnc7700 is located downstream of the 16s rRNA gene and downstream of HP1439 (Table 3.2), which encodes a hypothetical protein of unknown function. HP1439 and HPnc7700 are in the same orientation and in the opposite orientation of the 16s rRNA gene. The HP1439 homolog in strain B128 (HPB128_16g92) is predicted to be longer than HP1439 (155 versus 81 amino acid residues) and overlaps the sequence coding the putative sRNA_T, and so the sRNA_T mutant is potentially deficient for both sRNA_T and the product of HPB128_16g92.

The B128 sRNA_T mutant has a flagellation profile more similar to PMSS1 (Fig. 2.2F). In addition to perturbing flagellar number, we found that both these mutations altered other cell morphology parameters. Both the $fliO_{\Delta\mathrm{C}}$ and sRNA_T mutants displayed increased cell lengths (though similar to PMSS1), and increased cell curvature profiles (but still smaller than LSH100) relative to wild-type B128 (Table 3.3 and Fig. 3.2). These results suggest that perturbation of flagellar assembly may impact helical cell morphology and cell length in *H. pylori*.

We analyzed the swimming speeds of the different flagellar mutants in viscous PGM solutions (15 mg mL^{-1}) (see Video 6 for the sRNA_T flagellar mutant swimming in PGM at 15 mg mL^{-1}). We were only able to analyze speeds from a small bacterial population (n=23) for the $\mathit{fliO}_{\Delta \mathrm{C}}$ mutant because of difficulties finding fields of view with individual motile bacterial cells and because cells tended to clump (31%) as compared to wild-type (0.43%) (Table 3.4). A positive correlation between flagellum number and swimming speed was observed with significantly reduced swimming speeds (50% reduction in v_m) for $\mathit{fliO}_{\Delta \mathrm{C}}$ bacteria and increased swimming speeds (19% increase in v_m) for the sRNA_T mutant (Fig. 3.1B and Table 3.4). The B128 sRNA_T mutant also showed a higher v_m that was 18% faster than PMSS1 in this solution (14.9 μm/s vs. 12.2 μm/s) (Table 2.3 (Chapter 2) and Table 3.4). The standard deviation of swimming speeds, σ_{bac}, (Fig. 3.1C) suggest that sRNA_T displays similar swimming dynamics to wild-type B128 (K-S, p=0.29), $\mathit{fliO}_{\Delta \mathrm{C}}$ displays similar swimming dynamics to wild-type B128 (K-S, p=0.98), and $\mathit{fliO}_{\Delta \mathrm{C}}$ displays similar swimming dynamics to the sRNA_T mutant (K-S, p=0.57). Thus, altering flagellation does not impact temporal behavior in the swimming speed of individual bacteria. We observed a higher fraction of immobilized bacteria (82%) for $\mathit{fliO}_{\Delta \mathrm{C}}$, but saw a smaller fraction for the sRNA_T mutant compared to wild-type B128 (14% vs. 36%, respectively) (Table 3.4).

To explore whether variation in flagellum number influences other aspects of swimming, we analyzed reversals, ratio of forward and reversal swimming speeds, and cell path trajectory for wild-type bacteria and its isogenic flagellar mutants. We observed minimal effects of changing flagellum number on reversal frequency (Fig. 3.3A) and the ratio of forward to reversal swimming speeds (Fig. 3.3B). However, we observed differences in % track linearity between wild-type and its isogenic flagellar mutants (Fig. 3.3C). Reduced speeds and track linearity for the *fliO*$_{\Delta C}$ mutant may result from a combination of increased cell length, increased cell curvature, and decreased flagellum number. The sRNA_T showed increased % track linearity (Fig. 3.3C), suggesting that like PMSS1, sRNA_T may have increased directional persistence while swimming due to a higher proportion of bacteria with 4 or more flagella.

DISCUSSION

In addition to cell shape, we measured a significant contribution of flagellum number to *H. pylori* swimming speed. Increased flagellation (+1) of B128 through deletion of the sRNA_T gene resulted in an increase in median swimming speed (19%) (Fig. 3.1B), % track linearity (Fig. 3.3C), and a smaller fraction of bacteria immobilized in PGM (Table 3.4). The sRNA_T mutant bacteria were also longer than the parent strain B128 (Table 3.3), suggesting that an increase in flagellum number may enhance flagellar propulsion and overcome the propulsive drag provided by helical bacteria with increased cell length. Work by Mears *et al*. found an analogous finding for *E. coli*, as cells with increased flagellum number were observed to have increased cell length and a slight increase in swimming speed (Mears, 2014). In another *E.coli* study, Darnton *et al*. suggested that torque on a single flagellum and the flagella bundle are similar and an increase in flagellum number does not result in an increase in swimming speed (Darnton *et al*., 2007). They postulated that torque is dissipated when the peritrichous flagella of *E. coli* have to bend around the cell body to form the flagella bundle (Darnton *et al*., 2007). Perhaps consistent with this finding, induction of secondary lateral flagella in the single polar flagellated bacterium *Shewanella putrefaciens* resulted in higher directional persistence and spreading in soft agar, but lower swimming speeds (Bubendorfer *et al*., 2014). The lophotrichous flagella of *H. pylori* may lessen this effect, but as of now its flagella bundling behavior has not been explored. Future experiments imaging the flagella of swimming bacteria should shine light on the flagella bundling behavior and how altering flagellum number impacts bundling events.

EXPERIMENTAL PROCEDURES

Bacterial strains and culture conditions

Strains used in this study are described in Table 3.1. Wild-type *H. pylori* strain B128 (McClain *et al.*, 2009) and mutant derivatives (*fliO*$_{\Delta C}$ and sRNA_T) were cultured on horse blood plates or in liquid media containing 90% (v/v) Brucella broth (BD Biosciences) and 10% fetal bovine serum (GIBCO) (BB10) in the absence of antimicrobials as previously described (Sycuro *et al.*, 2010). Cells were maintained at 37^{o}C under microaerobic conditions in a tri-gas incubator equilibrated to 10% CO_2 and 10% O_2. Plates were incubated 24-72 hours and liquid cultures were incubated for 12-16 hours under constant agitation at 200 rpm.

Morphology analysis

Wild-type B128 and its respective isogenic flagellar mutants (*fliO*$_{\Delta C}$ and sRNA_T) were grown in liquid culture to an optical density at 600 nm (O.D. $_{(600)}$) of 0.3-0.7. Bacteria were fixed (4% Paraformaldehyde, 1X PBS, and 25% Glycerol) and added to 0.1% poly-L-lysine (Sigma Aldrich) coated coverslips that were placed on a pre-cleaned microscope slide, and were then sealed with VaLP (1:1:1 Vaseline: Lanolin: Paraffin). Single focal plane images were collected using a 100 X ELWD Plan APO (NA 1.40 oil) objective mounted on a Nikon TE 200 microscope, equipped with a Nikon CoolSNAP HQ CCD camera controlled by MetaMorph software (MDS Analytical Technologies). Quantitative morphology analysis of manually thresholded phase-contrast images was performed as described in Sycuro *et al.* using the CellTool software program (Lacayo *et al.*, 2007; Pincus and Theriot, 2007; Sycuro *et al.*, 2010). Centerline data for each strain was obtained from CellTool, imported to MATLAB, and fitted to a generalized sine curve, $y = R\sin(\frac{2\pi}{P}x + \delta)$, where R and P represent the helical radius and helical pitch, respectively, and δ is a phase term added to allow for an arbitrary origin of the sine function. Cells with non-helical morphologies resulted in poor fitting, characterized by a large sum of squared error (SSE > 0.2), and were removed from our data sets. The number of cells used to generate cell shape models were: wild-type B128, n=272; B128 *fliO*$_{\Delta\mathrm{C}}$, n=296; and B128 sRNA_T, n=305.

H. pylori flagellum length measurements and flagellum number counts

Flagellum number counts were acquired from TEM images for wild-type B128 and its isogenic flagellar mutants. The number of flagellum was counted from 83 - 105 different bacteria per strain. Flagellum length measurements were acquired from TEM images collected from the same preparation for all strains. TEM images were uploaded to Image J and calibrated using the scale bar (1 µm) of images acquired at 2500 - 3000 X. Using the segmented line selection tool, flagellum length was measured for one flagellum per cell, four times each, from 15 different bacteria per strain to provide average lengths and standard deviations from the means.

Generation of knockout isogenic flagellar mutants

Deletion of sRNA_T was generated in *H. pylori* B128 by the following procedure. Overlapping PCR was used to generate an amplicon that contained a kanamycin resistance cassette (*aphA3*) gene flanked by ~500 bp regions located upstream and downstream of the target sRNA. Primers used for PCR are listed in Table 3.2. The region upstream of sRNA_T was amplified using the upstream forward and the upstream reverse primers. The 5’-end of the upstream reverse primer contained sequence corresponding to one end of the *aphA3* cassette. The region downstream of sRNA_T was amplified using the downstream forward and the downstream reverse primers. The 5’-end of the downstream forward primer contained sequence corresponding to the other end of the *aphA3* cassette. The *aphA3* cassette was amplified using the kan forward and kan reverse primers. Overlapping PCR via the complementary regions of the amplified *aphA3* cassette and the amplicons of the regions flanking the target gene generated a PCR product with the *aphA3* cassette between the flanking regions. The resulting amplicon was introduced into *H. pylori* B128 by natural transformation. Replacement of sRNA_T with the *aphA3* cassette was confirmed by PCR using genomic DNA from kanamycin resistant transformants as a template, and was further verified by sequencing the resulting amplicons.

Motility assay in purified PGM

Same as the procedures described in Chapter 2.

Tracking of swimming bacteria using Volocity (v6.1)

Same as the procedures described in Chapter 2.

The supplemental videos (Videos 5 and 6) accompanying this thesis were collected using a 60 X objective lens at 100 millisecond intervals over a 10 second period (10 fps).

Analysis of the fraction of immobile bacteria in broth and viscous PGM solutions

The percentage of immobilized bacteria was determined as described in the Experimental Procedures of Chapter 2. The number of clumped bacteria (clusters of aggregated bacteria) was analyzed for B128 and the flagellar mutants in viscous PGM solutions (15 mg mL $^{-1}$). The percentage of clumped bacteria was calculated by dividing the total number of clumps by the total bacterial population. The total bacterial population consisted of the number of clumped bacteria, immobilized cells (individual cells with displacements < 0.3 μm), and motile cells (as described in the Experimental Procedures of Chapter 2).

TABLES

Table 3.1. Bacterial strains used in this chapter.

Strain Name	**Genotype or Description**	**Shape phenotype**	**Reference or Source**
B128	Wild-type *H. pylori*	helical	McClain *et al.*, 2009
fliO$_{\Delta \mathrm{C}}$	*fliO*$_{\Delta \mathrm{C}}$ in B128 C-terminal deletion: amino acids 217 to 283 were replaced with a FLAG tag	helical	Tsang and Hoover, 2014
sRNA_T	sRNA_T::*aphA-3* in B128	helical	This study

Table 3.2. Primers used in this chapter.

Targeted disruption primers

Name	**HPnc Number/ Alternative ID**	**Primer**	**Sequence**
sRNA_T	HPnc7700; Adjacent gene HP1439[a]/HPr07 (16S rRNA))	sRNA_T up F	AGT TTC ACA GCG CAT TAT AAG
		sRNA_T up R	GTA TAA CAT AGT ATC GAC TGA CAA GTT TGA TGA GCA GGA
		sRNA_T down F	GAA TTG TTT TAG TAC CTA GGC GAA TGT TAA AAG CTT TTC TC
		sRNA_T down R	ATA CAC GAA GAA CCT TAC CTA
		kan F	GTC GAT ACT ATG TTA TAC
		kan R	CTA GGT ACT AAA ACA ATT C

[a] Gene annotation in the human clinical isolate 26695 (Tomb *et al*., 1997).

Table 3.3. Average cell body and helical parameters of flagellar mutants.

	Average cell body parameters from Cell Tool[a]				**Average helical parameters**[b]		
Strain	n	Cell length (μm)	Side curvature	Cell diameter (μm)	n	Helical radius (μm)	Helical pitch (μm)
Wild-type B128	274	2.82	3.08	0.58	272	0.10	2.4
B128 *fliO*$_{\Delta C}$	307	3.25	3.98	0.66	296	0.17	2.6
B128 sRNA_T	326	3.41	3.94	0.60	305	0.14	2.5

[a] Cell body measurements acquired from CellTool.

[b] Helical parameter measurements acquired from fitting centerlines to a sinusoid.

Table 3.4. Speeds, percent track linearity, and the fraction of immobile wild-type bacteria and flagellar mutants in viscous PGM solutions (15 mg mL^{-1}).

	PGM[a] 15 mg mL^{-1}		
	WT B128	**B128 *fliO*$_{\Delta C}$**	**B128 sRNA_T**
n	100	23	100
Inst. values	2112	553	1673
v_{avg} (µm/s)	11.7	7.2	14.2
v_m (µm/s)	12.5	6.3	14.9
v_{max} (µm/s)	36.6	29.8	40.5
σ	5.5	4.8	5.6
K-S p-value[b]	<0.0001		<0.0001
% reduction to v_m relative to WT	50%		19% increase
Average %TL	77%	67%	84%
K-S p-value[b] for % TL	0.041		0.037

n	461	270	440
%Immobile[c]	36%	82%	14%
%clumps[d]	0.43%	31%	0.68%

[a] PGM: Purified gastric mucin at pH 6.0.

[b] For K-S tests used to compare WT to mutant cumulative distributions of swimming speeds and percent track linearity (%TL), p-values < 0.05 are considered significant.

[c] Fraction of immobile bacteria in viscous PGM solutions. Bacteria exhibit displacements < 0.3 µm (MSD < 0.1 μm^2).

[d] Fraction of clumped bacteria in viscous PGM solutions.

FIGURES

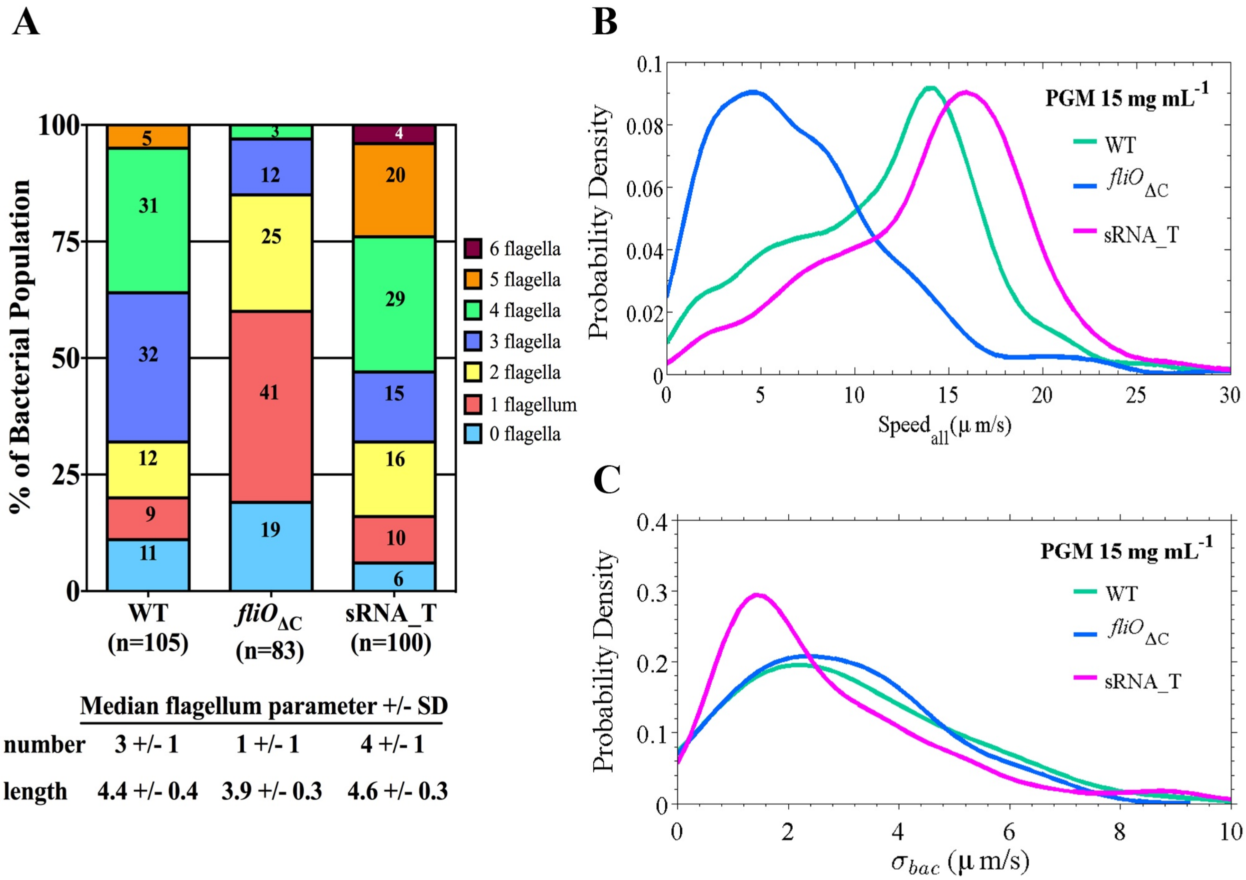

	Median flagellum parameter +/- SD		
number	**3 +/- 1**	**1 +/- 1**	**4 +/- 1**
length	**4.4 +/- 0.4**	**3.9 +/- 0.3**	**4.6 +/- 0.3**

Figure 3.1. Swimming speed correlates with flagellum number. (A) Individual bacteria were analyzed for the number of flagella from TEM images and are reported as percent of the total bacterial population examined (n=83-105). (B) Speed distributions and (C) speed standard deviation, σ_{bac}, distributions summarizing the speed variation acquired for wild-type B128 bacteria and isogenic flagellar mutants, $fliO_{\Delta C}$ and sRNA_T, in viscous solutions of PGM at 15 mg mL^{-1}. Representative data are from one of two independent experiments for each strain. The mutant speed distributions are significantly different from wild-type B128, where K-S $p < 0.05$ in each case (see Table 3.4). No significant difference in temporal speed distributions was observed between wild-type B128 and the B128 sRNA_T mutant (p=0.10), wild-type B128 and B128 $fliO_{\Delta C}$ mutant (p=0.98), or B128 sRNA_T and B128 $fliO_{\Delta C}$ mutants (p=0.29).

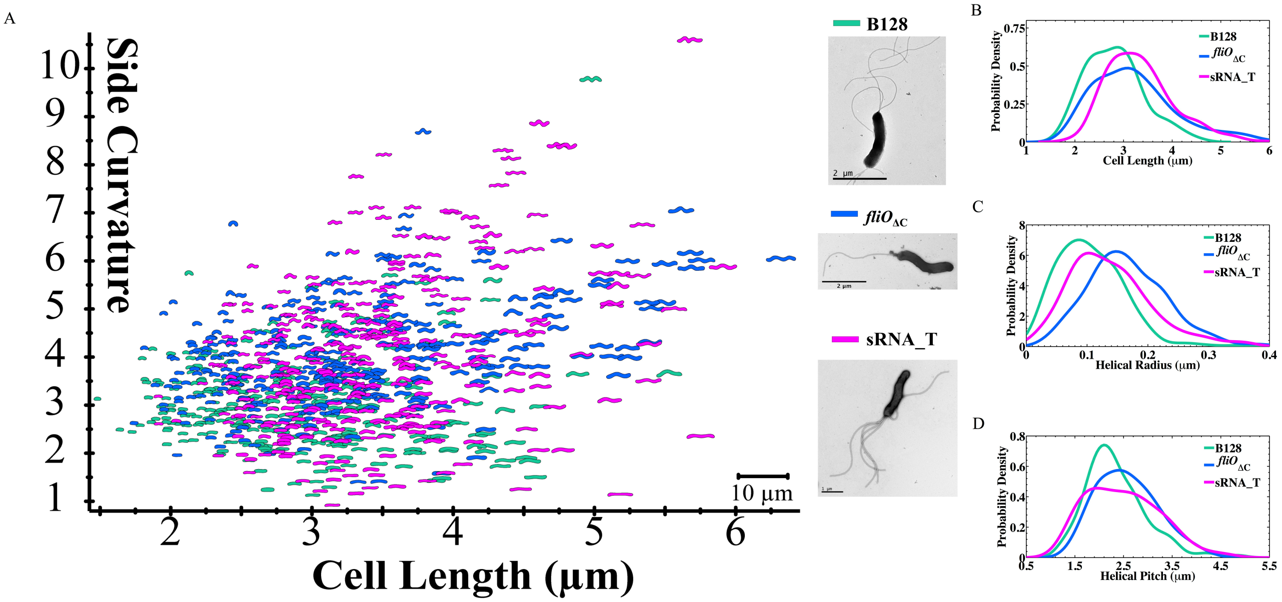

Figure 3.2. Flagellar mutants display increased cell length and helical parameters relative to wild-type B128. (A) Side curvature vs. cell length (µm) of individual bacterial cells imaged by phase contrast microscopy for wild-type B128 (n=274), *fliO*$_{\Delta \text{C}}$ (n=307), and sRNA_T (n=326) bacteria. Inset panel: TEM images of each. Scale bar = 1 µm for sRNA_T and 2 µm for wild-type B128 and *fliO*$_{\Delta \text{C}}$. Data shown are morphology analyses from two independent cultures for each strain. (B-E) Smooth histograms summarizing probability density distributions of cell length (µm) (B), helical radius (µm) (C), and helical pitch (µm) (D) measurements acquired for wild-type B128 (n=272), *fliO*$_{\Delta \text{C}}$ (n=296), and sRNA_T (n=305).

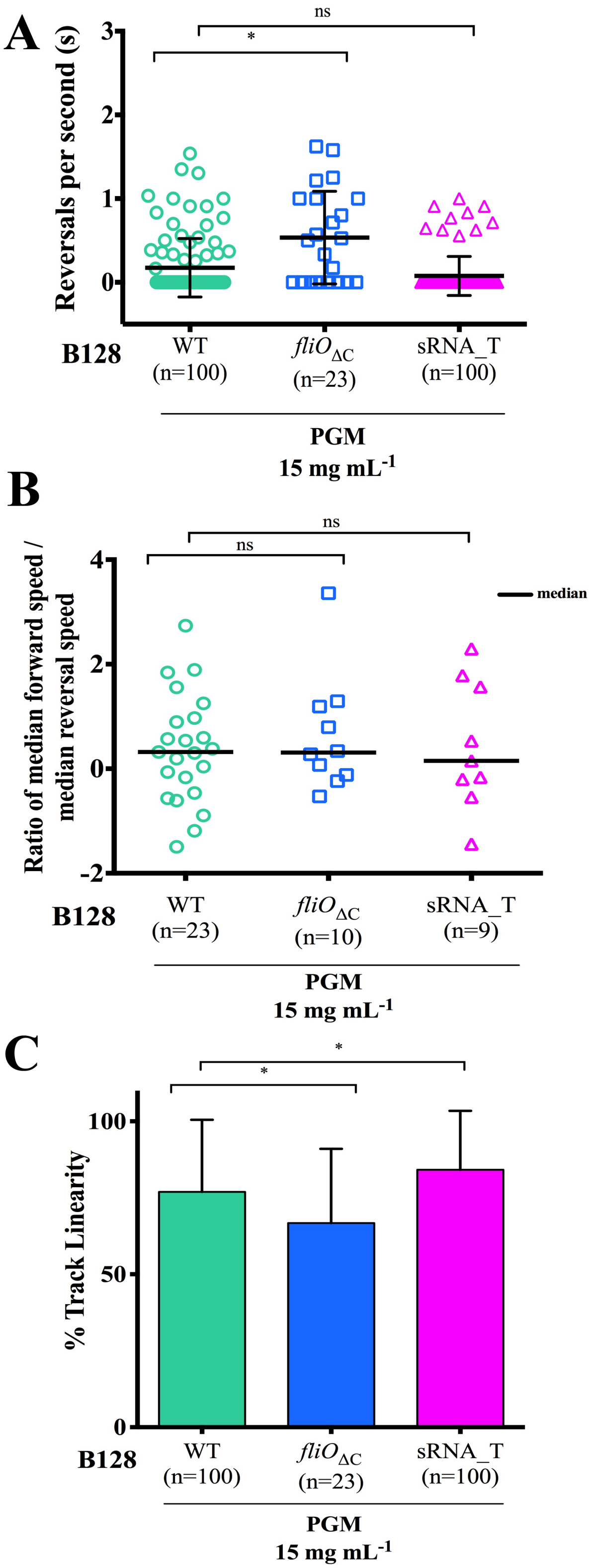
A
ns
*
Reversals per second (s)
3
2
1
0
B128
WT
(n=100)
fliO$_{\Delta C}$
(n=23)
sRNA_T
(n=100)
PGM
15 mg mL^{-1}
B
ns
ns
median
Ratio of median forward speed / median reversal speed
4
2
0
-2
B128
WT
(n=23)
fliO$_{\Delta C}$
(n=10)
sRNA_T
(n=9)
PGM
15 mg mL^{-1}
C
*
*
% Track Linearity
100
50
0
B128
WT
(n=100)
fliO$_{\Delta C}$
(n=23)
sRNA_T
(n=100)
PGM
15 mg mL^{-1}

Figure 3.3. Increased flagellation minimally affects reversal frequency, but increases % track linearity in *H. pylori*. (A) Dot plots summarizing the number of reversals per second acquired for wild-type B128 and isogenic flagellar mutants in viscous PGM solutions (15 mg mL^{-1}). Mean values of reversals per second are shown as bolded black lines and error bars indicate one standard deviation from the mean. The *fliO*$_{\Delta C}$ mutant shows a significant difference to wild-type B128 (KS, p =0.0114). (B) Dot plots summarizing individual ratios of median forward swimming speed to median reversal swimming speed acquired for each bacterial cell swimming in PGM (15 mg mL^{-1}). Ratios are plotted on a $\log_2$ scale and median values are shown as bolded black lines. (C) Bar histograms showing % track linearity (%TL) for wild-type B128 and isogenic flagellar mutants in PGM (15 mg mL^{-1}). Error bars show one standard deviation from the mean and mean %TL values are summarized in Table 3.4. All data shown is from the same experiment in Figure 3.1. *K-S p <0.05 was considered significant and ns = no significant difference.

CHAPTER 4

Implementation of a mathematical model to probe the contribution of both cell morphology and flagellar number variation on speed

INTRODUCTION

Chapters 2 and 3 discussed our findings where *H. pylori* strains vary both cell body helical parameters and flagellum number to maintain robust motility in viscous environments. In this chapter, we use a mathematical model to integrate our experimental findings into a conceptual framework that would allow us to probe the contribution of both cell morphology and flagellum number variation on *H. pylori's* swimming speed. We implemented the basic principles of resistive force theory (RFT) and force-torque balance, which have been extensively used to study flagellar propulsion and cell body-flagella interactions of different rod-shaped bacterial organisms to make swimming speed predictions (Gray & Hancock, 1955; Lighthill, 1976; Magariyama *et al*., 2002). RFT and force-torque balance state that the force and torque provided by a cell body or flagella must be proportional to the local velocity and angular frequency of the object (Gray & Hancock, 1955; Lighthill, 1976; Magariyama *et al*., 2002).

Our RFT-based model predicts that swimming speed (v_h) is proportional to a shape-dependent function (S_h) and a constant motor torque (T_m), where $v_h = S_h T_m$. Because swimming speed requires a flagellar motor torque, which has not been experimentally described for *H. pylori*, we calculated a shape factor for each wild-type *H. pylori* strain analyzed (LSH100, B128, and PMSS1) using their mean cell body measurements (Table 2.2). This application allowed us to gain insight into our experimental results by demonstrating how altering cell length, helical pitch, or helical radius impacts *H. pylori's* swimming speed.

We then hypothesized that the motor torque (T_m) increases proportionally with the number of flagella (N_f) in a flagella bundle, where $T_m = N_f T_f$ and T_f is the torque produced by a single flagellum. With this modification, swimming speed can be written as a function of both the shape factor and flagellum number, where $v_h = (S_h N_f)\, T_f$. To examine the concerted effects of both cell morphology and flagellum number variation on *H. pylori*'s swimming speed, we compared the product of $S_h N_f$ calculated for each wild-type *H. pylori* strain and for the flagellar mutant that showed increased flagellation (sRNA_T).

RESULTS

Resistive force theory modeling requires variation in both cell shape and flagellum number to explain speed differences observed between H. pylori strains

To gain further insight into our experimental results and the dependence of *H. pylori's* swimming speed on cell shape, we used Resistive force theory (RFT) (Gray and Hancock, 1955). RFT has previously been used to model swimming of *Caulobacter crescentus* (Li and Tang, 2006) *and Vibrio alginolyticus* (Magariyama *et al.*, 1995) by modeling their bacterial cell bodies as ellipsoids and their flagellum as a rotating rigid helix. In addition, bacteria were assumed to swim in a Newtonian fluid, where the viscosity of a fluid is constant for different rates of shear and does not change with time, and long-range hydrodynamic interactions were neglected. These simplifications make it possible to derive an analytical expression for the bacterium's swimming speed in terms of the motor torque on the flagellum, and the translational and rotational drag on the cell body and helical flagella bundle.

We used a similar approach for *H. pylori* but instead modeled its cell body as a thick helical rod, a geometry representative of its helical cell shape. The flagella bundle was modeled as a single thin helix attached at one end of the helical cell body. Using this geometry, the equations of motion for the cell body and flagellum can be written and solved analytically (for details on this derivation see Experimental Procedures). The final result is that swimming speed is proportional to the flagella bundle motor torque, T_m, via a shape factor S_h, $v_h = S_h T_m$. The motor torque, T_m, represents the influence of the flagellar motors on swimming while the shape factor, S_h, represents the effects of the translational and rotational drag of the cell body and flagella bundle. The shape factor relies on cell body and flagellar geometry and although the motor torque for *H. pylori* has not been measured, analysis of the shape factor provides insight into how different cell geometries affect swimming speed, with some geometries more efficiently converting motor torque to speed.

To examine how the shape factor depends on cell body helical parameters, we calculated S_h for a typical *H. pylori* bacterium with a cell length L = 3.1 μm, helical pitch P = 2.5 μm, helical radius R = 0.15 μm, and cell diameter D = 0.56 μm. These cell body parameters are the mean cell body measurements acquired for the three wild-type *H. pylori* strains: LSH100, B128, and PMSS1 (Table 2.2 in Chapter 2). For the flagella bundle, we used a bundle thickness of d = 0.07 μm, a flagellum pitch of p = 1.58 μm, a helical radius of r = 0.14 μm (see Experimental Procedures), and a flagellum length of l = 4.1 μm (the mean flagellum length of all the wild-type strains). Figure 4.1 shows the dependence of S_h on one cell shape parameter at a time (L, P, or R) keeping the other two parameters constant. In the parameter ranges observed for *H. pylori* (blue shaded region), S_h decreases monotonically with increasing L or R (Fig. 4.1 A,B), while it exhibits a non-monotonic dependence on P (Fig. 4.1C), exhibiting a shallow maximum at $P \approx$ 3.4 μm with a very slight decrease thereafter. This maximum corresponds to a speed maximum for bacteria with a pitch angle of approximately 15°. Our model predicts that in order to have a large S_h value, and hence a faster speed for the same motor torque, a helical cell must have a short cell length, small helical radius, and a helical pitch of approximately 3.4 μm.

To compare how the variation in cell shape for the different strains alters their shape factor, we calculated S_h for LSH100, B128, PMSS1, and the B128 sRNA_T flagellar mutant (Table 4.1). For each strain, S_h was calculated using their average cell body parameters (Table 2.2 in Chapter 2 and Table 3.3 in Chapter 3) and the same flagella bundle parameters described above. Table 4.1 shows that S_h for LSH100, PMSS1, and B128 sRNA_T all have similar values, while B128 has the largest S_h value (10% larger than all other strains). This is a result of the small average cell length and helical radius of B128 as compared to the other strains (Table 3.3 in Chapter 3). These shape factor differences would produce an approximate 10% change in swimming speed if all strains produced a similar motor torque on the flagella bundle. However, the differences in swimming speed in PGM at 15 mg mL^{-1} were observed to be much larger, ~ 0 - 90%. By comparing the ratios of shape factors to the ratios of swimming speeds (Table 4.1) we conclude that differences in shape factor alone do not fully explain the experimental swimming speed differences observed between the wild-type *H. pylori* strains.

Our experimental results show that *H. pylori* strains vary flagellum number (Fig. 2.2F in Chapter 2), and flagellum number correlates with swimming speed (Fig. 3.1 in Chapter 3). Based on this, we make the simplest hypothesis that the flagella bundle motor torque, T_m, increases proportionally with the number of flagella (N_f) in the flagella bundle, where $T_m = N_f T_f$ and T_f is the torque produced by a single flagellum. With this modification, the swimming speed can be written as a function of both the shape factor and flagellum number, $v_h = (S_h N_f)\, T_f$. Table 4.1 shows the product of $S_h N_f$ as calculated for each wild-type strain and the B128 sRNA_T flagellar mutant using their respective median flagellum numbers (Fig. 2.2F in Chapter 2 and

Fig. 3.1A in Chapter 3). The product of shape factor and flagellum number predicts larger differences, ~20-30% among the different strains as compared to the shape factor alone. For wild-type B128 and its flagellar mutant sRNA_T, the ratio of $S_h N_f$ agrees very well with the experimental ratio of swimming speeds, reflecting primarily the change in flagellum number, albeit with a small variation in cell length. The predicted $S_h N_f$ ratio for B128 and sRNA_T, relative to PMSS1, was within 10% of their measured speed ratios (Table 4.1). However, the predicted $S_h N_f$ ratio for LSH100 and PMSS1 does not agree well with the experimental ratio of speeds, suggesting that the RFT-model has some limitations in modeling the effects of helical-shaped bacteria.

DISCUSSION

To further understand the role of cell morphology on *H. pylori* swimming speed, we compared the influence of helical cell shape and number of flagella on swimming speed using a resistive force theory model. Assuming a constant motor torque, the swimming speed of helical-shaped bacteria is predicted to decrease with increasing cell length and helical radius, suggesting the fastest swimming speeds are obtained by bacteria with small cell lengths and small radii. However, altering helical cell shape led to a relatively small change in RFT-predicted swimming speeds, ~ 10%, in contrast to the large change in swimming speed observed experimentally (as much as 90%) for wild-type strains with different shape morphologies. Varying the motor torque using a simple linear dependence of motor torque on flagellum number produced a larger change in swimming speed, 20-30%, than that produced by only altering cell shape. Combining both the effect of cell shape and flagellum number, we were able to explain the observed differences in swimming speed for B128 and its isogenic flagellar mutant, sRNA_T, which reflects mostly the change in flagellum number. Comparing the other strains, which differ both in flagellum number and cell body helical parameters, produced mixed results. Comparing the ratios of RFT predictions for PMSS1 to those of B128 or sRNA_T showed better agreement with our experimental results than with predictions made when comparing PMSS1 to LSH100. Our results suggest that while both cell shape and flagellum number independently affect swimming speed, flagellum number contributes to a larger alteration in swimming speed. Recent modeling studies of bacteria with different numbers of peritrichous flagella predict that swimming speed increases logarithmically with increased flagellation (Kanehl and Ishikawa, 2014). While we assumed a linear model based on our experimental observations, a logarithmic dependence gives comparable results, predicting an increase of ~ 26% when comparing bacteria with four vs. three flagella and this supports our observations that swimming speed correlates with flagellum number.

While our RFT-based model provided insight into the relative effect of cell shape and flagellum number on swimming speed, it has inherent limitations. In particular, model predictions are based on cell shape parameters for an average or "typical" bacterium. However, the average or median speed measured from the speed distribution does not correspond to the speed of the average bacterium. Hence, the present state of modeling is capable of qualitative predictions, and one has to be careful in drawing detailed quantitative comparisons. The model underestimates the speed difference between LSH100 and PMSS1 and this may be due to it underestimating the shape factor for LSH100, which shows increased helical radius to PMSS1 (Fig. 2.2D and Table 2.2 in Chapter 2). Recent work by Rodenborn *et al.* showed that RFT can lead to inaccurate predictions for a helical flagellum with helical parameters in the range of $L>3P$ or $P<6R$ (Rodenborn *et al.*, 2013). These inaccuracies are due to RFT neglecting long-range interactions of the fluid flow from different parts of the helix. While our calculations for the cell body are outside the cited ranges, $L/P \approx 1.2$ and $P/R \approx 10$, Rodenborn *et al.* modeled a very thin helix (helical thickness to helical radius $D/R \approx 0.06$), which was meant to mimic the flagellum. For the *H. pylori* cell body, the helical radius is comparable to the cell thickness $D/R \approx 2$, meaning long-range hydrodynamic interactions may play a larger role. In light of this, we are currently exploring the use of a numerical solution of the hydrodynamic equations based on a regularized Stokeslet method to further probe the effect of helical cell shape on *H. pylori* swimming speed (Cortez *et al*., 2005).

Another aspect absent in our model is medium specific interactions. Our experimental results show medium specific changes in *H. pylori* swimming speed and temporal swimming behavior, which the RFT model cannot explain. Recently, Spagnolie *et al.* modeled a rotating helix in a viscoelastic fluid and showed that the swimming speed of the helix can increase or decrease depending on the combination of its helical parameters and the viscoelastic parameters of the medium (Spagnolie *et al.*, 2013). These effects could explain the increase in swimming speed observed for helical bacteria swimming in PGM solutions, however making any direct link between swimming speed and medium properties requires further study.

While efficient motility is essential for persistent colonization of the gastric mucus layer by this pathogen to get to its extracellular niche and during turnover of mucus and gastric epithelial cells, our study raises the question as to whether there may be selective pressures in addition to swimming speed that dictate *H. pylori* cell shape and flagellum number. Although both helicity and flagellum number alter swimming speed, it is noteworthy that their alteration resulted in a smaller change in speed (~1 μm/s) than the observed changes in an individual bacterium's speed with time (~1-5 μm/s). In addition, growth of a subpopulation of straight rod and curved cells along with bacteria with zero to two flagella persist in all strains analyzed (this work and Sycuro *et al.*, 2010). Having cells within the population with fewer flagella or a straight rod shape may play an unknown benefit to *H. pylori* unrelated to motility. Extending our cell-based morphologic studies to infected stomach tissues may begin to reveal whether different morphologies favor different niches within the stomach that include the surface mucus, gastric glands, and epithelial cell surface.

EXPERIMENTAL PROCEDURES

Resistive force theory mathematical modeling

At low Reynolds number the forces, F_c and F_f, and torques, T_c and T_f, on a bacterium must balance.

$$F_c + F_f = 0$$

$$T_c - T_f = 0$$

$$T_m - T_f = 0$$

Here *c, f*, and *m* denote the cell body, flagellum, and motor, respectively. Resistive force theory states that the forces and torques on an object are proportional to the local speed and angular rotation rate of that object, with the constant of proportionality determined by the object's geometry and viscosity of the liquid (Gray and Hancock, 1955).

We modeled the cell body of wild-type *H. pylori* as a rigid helix while the bacterium's helical flagellum was assumed to bundle and form a single helix. The total force on a translating and rotating helix is a sum of the translational drag, $F_{drag} = -\alpha_h v_h$, and rotational propulsion, $F_{propulsion} = \gamma_h \omega_h$, while total torque is a sum of the rotation drag, $T_{drag} = \beta_h \omega_h$, and translation drag, $T_{propulsion} = -\gamma_h v_h$. Here α_h, β_h, and γ_h represent the translational, rotational, and propulsion drag coefficients of a helical cell body, respectively. In an analogous way, the flagellum has translational, rotational, and propulsion drag coefficients which we designate as α_f, β_f, and γ_f, respectively.

Using the force and torque equations above, along with force torque balance between the cell body and flagellum, we solved for the swimming speed of a helical cell body, v_h, in terms of the motor torque, T_m. The swimming speed can be written as the product of T_m, and a shape factor, S_h, that depends on the cell body and flagellum drag coefficients.

$$v_h = S_h T_m$$

$$S_h = \frac{\frac{\gamma_h}{\beta_h} + \frac{\gamma_f}{\beta_f}}{\alpha_h + \alpha_f - \frac{\gamma_h}{\beta_h}\gamma_h - \frac{\gamma_f}{\beta_f}\gamma_f}$$

To calculate S_h we used previously derived expressions for α_h, β_h, and γ_h in terms of the cell body parameters: cell length (L), helical pitch (P), helical radius (R), and pitch angle (Φ) (Rodenborn *et al.*, 2013) with local normal (C_n) and tangential (C_t) force expressions derived by Gray and Hancock (Gray and Hancock, 1955). Using the same formula, the flagellum coefficients α_f, β_f, and γ_f can be written in terms of the flagellum helical length (l), pitch (p), radius (r), pitch angle (ϕ), and local normal (c_n) and tangential (c_t) forces.

$$\alpha_h = (C_n \sin^2(\Phi) + C_t \cos^2(\Phi))L$$

$$\beta_h = (C_n \cos^2(\Phi) + C_t \sin^2(\Phi))R^2 L$$

$$\gamma_h = (C_n - C_t)\sin(\Phi)\cos(\Phi)RL$$

$$\alpha_f = (c_n \sin^2(\phi) + c_t \cos^2(\phi))l$$

$$\beta_f = (c_n \cos^2(\phi) + c_t \sin^2(\phi))r^2 l$$

$$\gamma_f = (c_n - c_t)\sin(\phi)\cos(\phi)rl$$

Using these expressions, the drag coefficients and shape factor were calculated using average cell shape measurements acquired from CellTool (Fig. 2.2 in Chapter 2). For wild-type *H. pylori* strains, we used the average helical parameters acquired from fitting the centerlines of each bacterial cell within each wild-type population (Fig. 2.2B and Table 2.2 in Chapter 2). We acquired a uniform flagellum diameter (*d* ~0.07 μm), and used the average flagellum length (*l*) acquired from measurements done on TEM and SEM images (Figures 2.2 and 2.7 and Table 2.5 in Chapter 2). Because the flagellum helical pitch (*p*) and helical radius (*r*) for *H. pylori* have not been measured, we assumed a helical flagellum form similar to that of *Vibrio alginolyticus*, where $p = 1.58$ μm and $r = 0.14$ μm (Magariyama *et al.*, 1995) for all bacteria examined in this study. All numerical calculations and manipulations were done using MATLAB v7.12.

Table 4.1. Comparison of experimental median speeds in PGM (15 mg mL^{-1}) and predictions of Resistive Force Theory-model implementations.

Strain	Median speed in PGM[a] 15 mg mL^{-1} (µm/s)	S_h[b] +/- SE[c]	S_hN_f[d] +/- SE
LSH100	6.5	115 +/- 10	345
PMSS1	12.2	120 +/- 7	480
B128	12.5	132 +/- 8	396
B128 sRNA_T	14.9	116 +/- 8	464

Strains compared	Ratio of median speed in PGM 15 mg mL^{-1}	Ratio of S_h +/- SE	Ratio of S_hN_f +/- SE
sRNA_T / B128	1.2	1.9 +/- 0.1	1.2 +/- 0.1
sRNA_T / PMSS1	1.2	1.0 +/- 0.1	1.0 +/- 0.1
B128 / PMSS1	1.0	1.1 +/- 0.1	0.8 +/- 0.1
LSH100 / PMSS1	0.5	1.0 +/- 0.1	0.7 +/- 0.2

[a] PGM: Purified gastric mucin at pH 6.0.
[b] S_h: Shape factor.
[c] SE: Standard error.
[d] S_hN_f: the product of shape factor and median flagellum number.

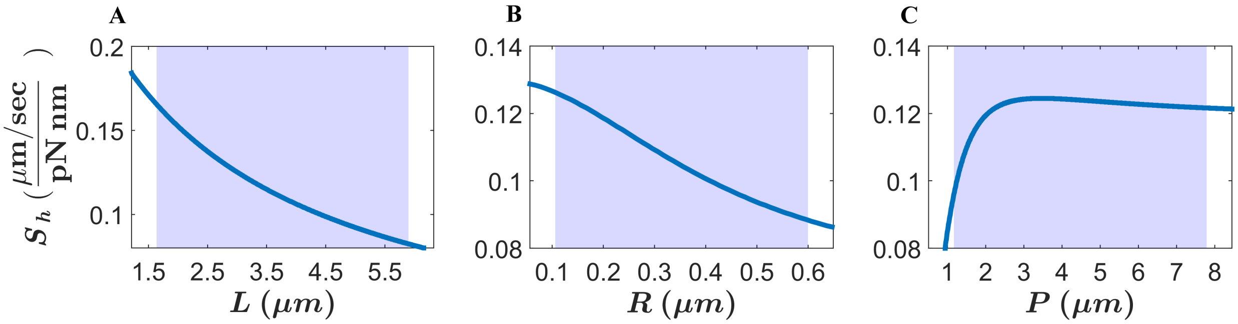

Figure 4.1. Resistive force theory model predicts that variation in helical body length (*L*), helical radius (*R*), and helical pitch (*P*) alter *H. pylori's* shape factor, S_h. Calculated shape factor (S_h) for a bacterium with helical cell body shape. In each plot, the dependence of S_h is shown for a single cell body parameter L (A), R (B), or P (C) while keeping the other two parameters constant. The parameters that were not varied were maintained at a cell length $L = 3.1$ µm, helical pitch $P = 2.5$ µm, helical radius $R = 0.15$ µm, cell diameter $D = 0.56$ µm, flagellum length $l = 4.1$ µm, flagellar pitch $p = 1.58$ µm, flagellar helical radius $r = 0.14$ µm, and flagella bundle thickness $d = 0.07$ µm. These are the average helical cell body or flagellum morphological parameters acquired for the wild-type *H. pylori* strains LSH100, B128, and PMSS1 (Figure 2.2 and Table 2.2 in Chapter 2; Figures 3.1A and 3.2 and Table 3.3 in Chapter 3). The blue shaded regions represent the range (min to max) of the cell shape parameters observed experimentally for LSH100, B128, PMSS1, and the B128 sRNA_T isogenic flagellar mutant.

CHAPTER 5

Visualization of *H. pylori* during initial colonization reveals multiple gastric niches and specific deficits for cell shape mutants

INTRODUCTION

Chapters 2, 3, and 4 focused on the effects of cell shape and flagellum number variation and how they influence *H. pylori* swimming behavior *in vitro*. In this chapter, I explore how these changes influence localization of the bacterium within the stomach.

Different wild-type *H. pylori* strains show tropism for the corpus (the main body of the stomach where acid is produced) or the antrum (Akada *et al*., 2003). Upon establishing residence, the majority of *H. pylori* are found living within a narrow band of gastric mucus immediately overlying the gastric epithelium (Schreiber *et al.* 2004). Bacteria living in mucus may act as a reservoir of infection for the underlying surface epithelial cells and gastric glands. Only a small proportion of bacteria are found in association with gastric epithelial cells, but the interaction of bacteria with epithelial cells may be important for the development of disease. *H. pylori* may also penetrate into the gastric pits and establish residence within gastric glands and grow as cell-associated microcolonies (Fig. 1.2D in Chapter 1). It is thought that these bacteria serve as a reservoir for repopulating at the superficial mucosa, that is subject to the mechanical forces generated by peristalsis and epithelial cell sloughing.

To gain understanding of how cell shape impacts *H. pylori’s* ability to acquire a gastric niche *in vivo*, we exploited the use of the cell shape mutants to (1) test their fitness in a mouse model of infection, and (2) determine their localization within different regions of the stomach. We tested the wild-type *H. pylori* strain PMSS1, an isogenic mutant with curved and variable morphologies (Δ*csd1*), and an isogenic straight rod mutant (Δ*csd6*). These experiments utilize

PMSS1 because this clinical isolate has been previously used to localize bacteria in infected mouse tissues, both in the superficial mucus lining of the stomach epithelium and in dense colonies deep within the gastric glands (Howitt *et al*., 2011; Sigal *et al*., 2015). In addition, chronic infection with PMSS1 in mice triggers chronic inflammation and hyperplasia, and manifests early signs of metaplasia (Arnold *et al*., 2011), which makes it an ideal model to study as it mimics human pathology.

We conducted a time course of single-strain infections and assessed their localization within the stomach during initial colonization (1 day and 1 week of infection) and chronic infection (1, 2, and 4 months). We utilized confocal microscopy and image-based 3D reconstructions of infected gastric tissue to determine the localization of wild-type *H. pylori* bacteria and the cell shape mutants in different regions of the stomach. Because *H. pylori* may colonize both the surface mucus and penetrate gastric glands to establish a niche within the gastric gland lumen, we will examine both these populations (Fig. 1.2D in Chapter 1). However, this chapter presents preliminary findings from a pilot experiment that only examines and quantitates *H. pylori* within gastric glands.

RESULTS

Loss of csd1 results in a strain-specific alteration in cell morphology

We characterized the morphology of the *csd1* deletion mutant generated in the PMSS1 strain background using the CellTool software program (described in Chapter 2) (Lacayo *et al*., 2007; Pincus and Theriot, 2007; and Sycuro *et al*., 2010). Generation and morphological analysis of the *csd6* deletion mutant in PMSS1 was discussed in Chapter 2 (Fig. 2.9). Deletion of *csd1* in the PMSS1 strain background resulted in curved rods with varying degrees of curvature and cells with variable morphologies ranging from "c"-shapes, coiled, helical, and straight rods (Fig. 5.1A). Significant differences in side curvature distributions were observed between wild-type and Δ*csd1* (K-S statistics, $p<0.00001$) (Fig. 5.1B). In addition to the measured differences in side curvature, the mutant showed significant differences in cell diameter to wild-type (data not shown). The variable non-helical morphology observed in the PMSS1 strain background appears distinct from the phenotype of Δ*csd1* in the LSH100 strain background, which exclusively showed curved rod morphology (Fig. 1.4 in Chapter 1). This mutant was unable to colonize the stomach as efficiently as helical shaped bacteria (Sycuro *et al*., 2010).

The helical cell shape of H. pylori confers an advantage during initial colonization of the stomach

To study how helical morphology promotes both colonization in the stomach and persistence, we conducted single-strain infections with wild-type, Δ*csd1* (variable shapes), and Δ*csd6* (straight) and determined their stomach colonization load in mice early after infection (1 day and 1 week) and after chronic infection (1-4 months) compared to wild-type (Fig. 5.2).

We observed significant attenuation during initial colonization (1-2 log difference in recovery of bacteria) of both Δ*csd1* and Δ*csd6* after a day and a week of infection (Fig. 5.3A). These results are consistent with our published observations for a curved rod (Δ*csd1*) and straight rod mutant (Δ*csd4*), generated in a different *H. pylori* strain background (LSH100) (Sycuro *et al*. 2010; Sycuro *et al*., 2012). At later time points of infection, a subset of mice infected with Δ*csd1* or Δ*csd6* showed robust stomach colonization levels that were comparable to or above wild-type load levels, while other mice showed very low colonization loads or no colonization at all (Fig. 5.3A). As expected, we did not recover bacteria for the uninfected group controls.

Our results suggest that helical cell shape provides *H. pylori* an advantage during early colonization of the stomach.

Development of a system to quantitate bacteria in infected-gastric tissue

Usually *H. pylori* infection is visualized using histology of very thin 4-5 μm tissue sections. Quantification of *H. pylori* is limited by this technique, as *H. pylori* in the tissue is restricted to the gastric gland lumen that is rarely captured in thin sections. We thus have employed methods developed by Manuel Amieva's group at Stanford University, where by immunofluorescence, confocal microscopy, and 3-dimenstional (3D) reconstructions of thick longitudinal tissue sections (100-200 μm) that fully capture the gastric gland lumen, we can assess the anatomical localization of bacteria within different regions of the stomach and within glands (Fig. 5.4) (Howitt *et al.,* 2011; Sigal *et al*., 2015).

We first generated 3D-images of wild-type *H. pylori* bacteria to determine the volume of an individual bacterial cell. This volumetric measurement would be used to quantitate the number of bacterial cells found within different microcolonies. Wild-type bacteria fixed in paraformaldehyde (PFA) showed excellent cellular and subcellular structures (note the cell body and flagella bundle of a bacterium in Fig. 5.5A). We used the Volocity 3D-image analysis software to quantify the volume for individual bacterial cells based on their fluorescence signal intensity and total volume (μm^3) (Fig. 5.5C). We found that the mean volume for 200 individual bacterial cells analyzed was ~10 μm^3. Analysis of two bacteria provided a mean volume of ~21 μm^3 (Fig. 5.5C), suggesting a direct increase in volume as the grouping of bacterial cells increased. The mean volume of 10 μm^3 was used to calculate the total number of bacteria colonizing different regions of the gastric glands, including dense microcolonies.

Since most *H. pylori* bacteria colonize the mucus layer immediately overlying the gastric epithelium, we also optimized methods to preserve and stain the surface mucus. We used modified Carnoy's solution (Methacarn, 60% methanol: 30% chloroform: 10% glacial acetic acid) to help preserve the mucus layer (Fig. 5.5D). Even though this fixation method does not retain as well the cellular structure of gastric cells and bacteria, we were able to perform volumetric analysis of bacteria (Fig. 5.5B) and obtain measurements for ~200 individual bacterial cells (Fig. 5.5C). In this fixative, the mean volume per bacterium was 6 μm^3. Analysis of two bacteria provided a mean volume of 13 μm^3 and the analysis of 3-4 bacteria provided a mean volume of 23 μm^3 (Fig. 5.5C), further confirming a direct increase in volume as the grouping of bacterial cells increased. The mean volume of 6 μm^3 will be used to quantitate bacteria within the surface mucus population in future studies.

Mutation of csd6 attenuates antral gland colonization during early infection

In our pilot experiment, we used 3D-confocal microscopy and volumetric analysis to quantitate the number of bacteria residing within corpus or antral gastric glands. Our measurements include the quantification of bacteria present per field of view (~355 μm wide) along the mucosa (from the limiting ridge at the forestomach to the pyloric junction with the duodenum) (Fig. 5.4A). We determined the localization of wild-type bacteria and straight rods from mice samples with similar bacterial loads by CFU/gram of stomach. After a day of infection, both wild-type and straight rods showed similar low levels of colonization of both the corpus and antral regions (ranging from 0 to 40 bacteria per field of view) (Fig. 5.6). However, quantitation of bacteria at these regions does not explain the 1-2 log load difference observed between wild-type and the mutant by our CFU data (Fig. 5.3A). This discrepancy may reflect the mucus population that is not well preserved by paraformaldehyde fixation.

At one week, wild-type bacteria robustly colonized the antral glands (~200-600 bacteria per field of view), but showed limited colonization of corpus glands (Fig. 5.7A). The straight rod mutant colonizes the antrum at a log lower density than wild-type (0-20 bacteria per field of view), but colonizes the corpus with a similar density as wild-type (Fig. 5.7B). This ~1 log difference in colonization of the antrum parallels the 1 log difference in bacterial load observed between wild-type and the straight rod mutant by CFU (Fig. 5.3A).

Complementation restores antral gland colonization of **Δ***csd6 mutant*

To determine whether the antral predominance localization of wild-type bacteria is directly impacted by the nature of its helical cell morphology, we assessed the localization of a *csd6* complemented strain after a week of infection. We complemented the mutant by expressing the *csd6* gene at a distal and neutral locus in *H. pylori*, the McGee locus (Sycuro *et al*., 2013; Langford *et al*., 2006). Complementation of *csd6* restored helical cell shape (Fig. 5.8A,B) and no significant differences in side curvature distributions were observed between wild-type and the *csd6* complemented strain (K-S statistics, p =0.64078) (Fig. 5.8C). As expected, significant differences in side curvature distributions were observed between the Δ*csd6* and the *csd6* complemented strain (K-S statistics, p<0.00001) (Fig. 5.8C).

After a week of infection, the *csd6* complemented strain robustly colonizes the antrum and like wild-type, shows decreased colonization of the corpus that is about 1-2 logs lower from the bacterial density observed in the antrum (Fig. 5.7C). Fig. 5.9 shows 3D-stacked images (Z-stack projections) of one-week infected antrum sections with wild-type, Δ*csd6*, and the *csd6* complemented strain. For the wild-type infected antrum, you can see bacteria associated with gastric epithelial cells at or near the surface epithelium and bacteria that have penetrated the gastric glands to form dense microcolonies within most of the gastric glands shown (Fig. 5.9A). The Δ*csd6*-infected antrum only shows few bacteria at the surface but no penetration of antral glands within this tissue field of view (~355 μm wide) (Fig. 5.9B). As indicated by our localization studies, *csd6* complemented bacteria colonize the surface epithelium and all neighboring antral glands (Fig. 5.9C).

Given our preliminary results where helical cell shape provides an advantage in colonizing antral glands early after infection (1 week), we decided to focus our studies on the straight rod mutant. We repeated a time course of single-strain infections with wild-type, Δ*csd6,* and the *csd6* complemented strain, and determined their stomach colonization loads after early (1 week) and chronic infection (1 and 3 months). We used a larger cohort of mice (15 mice) per infection group for the long-term infection studies. In this case, we obtained similar stomach colonization loads between wild-type and Δ*csd6*-infeced mice*,* and for Δ*csd6* and the *csd6* complemented strain (Fig. 5.3B). Similar to our results presented in Fig. 5.3A, we observed a bimodal spread of stomach colonization loads in different mice from each infected genotype after a month of infection (Fig. 5.3B). A subset of mice infected with wild-type, Δ*csd6*, or the *csd6* complemented strain showed robust stomach colonization loads, while a subset of mice showed reduced stomach colonization loads. In one case, a mouse cleared the mutant bacteria (Fig. 5.3B). At three months of infection, we observed similar stomach colonization loads (~10^5 CFU/gram), with similar geometric means, between each infected group (Fig. 5.3B).

Straight rods chronically infect the stomach

Our studies show variable stomach colonization loads in wild-type and Δ*csd6*-infected mice after 4 months of infection. We determined the localization of wild-type bacteria and straight rods from mice samples with similar bacterial loads by CFU/gram of stomach (~2 x10^4). At 4 months, straight rods persistently colonize the stomach and show slightly higher corpus gland colonization, while wild-type colonizes both the corpus and antrum (Fig. 5.10). These results suggest that straight rods established and persistently maintained a niche within corpus glands.

Chronic infection with cell shape mutants reveals differences in inflammation and hyperplasia

To determine the pathology of chronically infected samples, H&E-stained gastric tissue samples of uninfected, wild-type, Δ*csd1*, and Δ*csd6* infected samples after 1 - 4 months were examined for inflammation and hyperplasia in the corpus/antral junction and the antrum (Figures 5.11 and 5.12). No significant inflammation and hyperplasia was observed in the corpus for any of the samples.

The scoring criteria for inflammation and hyperplasia are presented in Table 5.4. Uninfected mice did not show inflammation or hyperplasia at the corpus/antral junction or at the antrum after 1, 2, and 4 months (Fig. 5.12). The stomach loads (CFU/gram) of the two mice samples submitted for pathology per group (Fig. 5.3A) are presented in Fig. 5.12A. After a month, both wild-type-infected mice (with 10^5 - 10^6 CFU/gram of stomach loads) had mild patchy or moderate coalescing infiltrates in the mucosa (scores of 1 and 2) and mild hyperplasia (score of 1) in the corpus/antral junction (Fig. 5.12B-C), while one of the Δ*csd1* infected mice (~2.5x10^4 CFU/gram load) had more inflammation (score of 3) in the corpus/antral junction

(Figures 5.11 and 5.12B) and in the antrum (score of 2) (Fig. 5.12D). This mouse sample also showed increased hyperplasia (score of 2) in the corpus/antral junction, but mild hyperplasia (score of 1) in the antrum that was comparable to wild-type (Fig. 5.12C,E). Both Δ*csd6*-infected mice (loads of 10^4-10^7 in CFU/gram) produced little or no inflammation or hyperplasia at the corpus/antral junction or the antrum after a month of infection (Fig. 5.11 and 5.12B-E). These results suggest a delayed inflammatory response for the Δ*csd6*-infected mice, with little or no disease in the mucosa.

After two months, wild-type-infected mice with similar CFU loads (~10^4-10^5), had inflammation scores of 1 and 2 at both the corpus/antral junction and the antrum (Fig. 5.12B,D). One of the Δ*csd1*-infected mice cleared the bacteria (0 CFU/gram) and this tissue sample did not show signs of inflammation or hyperplasia in the corpus/antral junction or the antrum. The second Δ*csd1*-infected mouse with a very low bacterial load (409 CFU/gram) produced considerable inflammation at the corpus/antral junction (score of 3) and at the antrum (score of 2) (Fig. 5.12B,D). Its hyperplasia scores (score of 2) were comparable to wild-type at the corpus/antral junction and antrum (Fig. 5.12C,E). At two months, the Δ*csd6*-infected mice caught up and produced comparable inflammation and hyperplasia to wild-type and the Δ*csd1*-infected mice (Fig. 5.12B-E).

After four months of infection, wild-type infected mice showed increased stomach colonization loads as compared to Δ*csd1* (< 1 log) and Δ*csd6* (~ 2 logs) infected mice (Fig. 5.12A). Both wild-type and cell shape mutant-infected samples showed variable inflammation and hyperplasia at the corpus/antral junction and the antrum (Figures 5.11 and 5.12B-E).

DISCUSSION

Our pilot studies reveal that helical cell shape is not required for stomach colonization, but confers an advantage for robust colonization of the stomach early after infection. Cell shape mutants have reduced stomach colonization potential (~1-2 log) after a day and a week of infection (Fig. 5.3A). Our preliminary bacterial localization studies reveal that straight rods colonize both the corpus and antrum at a similar density to wild-type after a day of infection (Fig. 5.6). At one week, straight rods localize to the corpus at a similar density to wild-type, but are compromised in their ability to colonize antral glands (Fig. 5.7B).

Although straight rods show attenuated stomach colonization early after infection, they persistently colonize the stomach (Fig. 5.3A), and at four months, show higher corpus gland colonization than wild-type (Fig. 5.10). We hypothesize that early colonization events may impact persistence and regional pathology.

We then asked whether pathologic outcomes differ between mice infected with wild-type bacteria to mice infected with cell shape mutants. We compared pathologic changes after 1, 2, and 4 months of infection. We found that in all mice evaluated for pathology (n= 2 mice per group), only the corpus/antral junction and the antrum showed hyperplasia and signs of chronic inflammation. After a month of infection, mice infected with straight rods resulted in reduced hyperplasia and inflammation to wild-type (Figures 5.11 and 5.12). Over a two and four month time course, mice infected with straight rods showed similar inflammation and hyperplasia to wild-type (Fig. 5.12), suggesting a delayed inflammatory response. In contrast, infection with the curved rod mutant (Δ*csd1*) showed increased inflammation and hyperplasia to wild-type after a month infection (Figures 5.11 and 5.12). Both wild-type and shape mutants showed variable inflammation and hyperplasia after two and four months of infection.

The most drastic pathologic outcomes of Δ*csd1* and Δ*csd6* infected mice to wild-type infected mice occurred both after a month of infection and within the corpus/antral junction and the antrum. These results suggest that differences in colonization of gastric glands exist between wild-type and the cell shape mutants, but these differences do not necessarily correlate with bacterial load, as measured by CFU. For example, mice with low bacterial loads exhibit a high degree of hyperplasia and chronic inflammation (i.e. Δ*csd1* after two months) (Fig. 5.12). Because we only have data from a small group of mice, we cannot make definitive conclusions. Further evaluation of a larger group of mice is required as it may help provide insight on how regional localization of bacteria within the stomach relates to the corpus/antral junction and antral predominant inflammation and hyperplasia observed.

To begin to address this, we conducted single-strain infections with wild-type, Δ*csd6,* and the *csd6* complemented strain using 15 mice per group for long-term infection study (Fig. 5.3B). Similar to our pilot study, we observed a subset of mice with increased stomach colonization loads and a subset of mice with decreased colonization after a month of infection (Fig. 5.3B). This bimodal spread in stomach colonization load was less pronounced in the three-month colonization data (Fig. 5.3B). To provide further insight on how the bimodal feature in stomach colonization load impacts the ability of *H. pylori* to support chronic colonization, we plan to evaluate the pathologic outcomes of multiple mice per group with varying stomach colonization loads. Beyond the scope of this study, we would like to evaluate the localization of Δ*csd1* within the stomach during initial colonization and after chronic infection; describe the local immune response to chronic infection; and determine how active inflammation augments gland hyperplasia.

Our 3D-visualization system will help us gain a better understanding of why the cell shape mutants show attenuated stomach colonization, and may help provide insight on the natural course of *H. pylori* infection and persistence in the stomach. However, our assay has limitations. Because *H. pylori* may colonize corpus or antral glands and at varying loads, we would like to determine where bacteria reside within gastric glands. Our bacterial localization assay quantifies the total number bacteria in each tissue section per field of view (355 μm wide), and it does not distinguish the fraction of bacteria at or near the surface epithelium from the fraction of bacteria that colonized deep within gastric glands. Given that *H. pylori* may robustly colonize antral glands and impact progenitor and stem cell compartments, which in turn may induce glandular hyperplasia (Sigal *et al*., 2015; Earle *et al*., 2015), we would like to examine the bacterial population within different gastric gland compartments: at the top (near the surface), mid (progenitor/stem cell compartment), and base of glands. To carefully characterize these fractions, we will implement a new software program, BacSpace, which will allow us to automatically distinguish these populations and quantify the invasion depth of *H. pylori* within gastric glands (Earle *et al*., 2015). Because chronic *H. pylori* infection induces glandular hyperplasia, this subsequently generates pathologic changes within the glands that include alteration in gland height. Therefore, we will determine whether any differences in invasion depth or gland height exist between wild-type infected mice and mice infected with the cell shape mutants.

H. pylori colonization of gastric mucus may be essential to the establishment of chronic infection as bacteria may act as a reservoir of infection for underlying gastric epithelial cells. The discrepancy between our CFU data and the number of bacteria quantified by our 3D-imaging and volumetric analyses may reflect the mucus population, which is not well preserved by the fixation method used in our pilot study. However, we have shown that the surface mucus can be preserved using a Methacarn fixation method (Fig. 5.5D). Characterization of the bacterial population within the surface mucus will help determine whether cell shape impacts this population in addition to the gland population, as observed for the straight rods after a week of infection (Fig. 5.7B and 5.9B). BacSpace may also be implemented to measure mucus and bacterial density, distance from the epithelium, and variability between different mouse samples (Earle *et al*., 2015).

In summary, the data presented in this chapter indicate that helical cell shape perturbation alters the ability of *H. pylori* to utilize some of the available niches within the stomach in addition to altering swimming speed in mucus. Furthermore, our established mouse model is used to define the role of cell shape in *H. pylori's* ability to acquire specific gastric niches within the stomach.

EXPERIMENTAL PROCEDURES

H. pylori strains and culture conditions

Strains used in this study are described in Table 5.1. Wild-type *H. pylori* strain PMSS1, also called 10700 (Lee *et al*., 1997; Arnold *et al*., 2011) and mutant derivatives (Δ*csd1* and Δ*csd6*), and the *csd6* complemented strain, were cultured on horse blood plates or in liquid media containing 90% (v/v) Brucella broth (BD Biosciences) and 10% fetal bovine serum (GIBCO) (BB10) in the absence of antimicrobials as previously described (Sycuro *et al*., 2010). Cells were maintained at 37^oC under microaerobic conditions in a tri-gas incubator equilibrated to 10% CO_2 and 10% O_2. Plates were incubated 24-72 hours and liquid cultures were incubated for 12-16 hours under constant agitation at 200 rpm. For resistance marker selection, horse blood plates were supplemented with chloramphenicol (15 μg mL^{-1}) or kanamycin (25 μg mL^{-1}).

Generation of PMSS1 knockout isogenic cell shape mutants

Isogenic mutants of *csd1* (HPG27_1481) and *csd6* (HPG27_477) in the PMSS1 strain background were generated by transfer of the mutation constructed in the LSH100 strain background (Sycuro *et al*., 2010; Sycuro *et al.,* 2013) using natural transformation (Wang *et al*., 1993). Transformants were confirmed by PCR using primers homologous to upstream and downstream flanking regions for each gene using the primers indicated in Table 5.2. The mutation was then backcrossed into PMSS1 once by isolating genomic DNA from the resulting strain for natural transformation of PMSS1. The resulting backcrossed clones were evaluated by PCR to confirm replacement of the wild-type allele with the null allele. Clones were checked for urease activity and motility, and single clones were used for quantitative morphology analyses and for oral gavage of mice.

Construction of the csd6 complemented strain

The *csd6* complemented strain was constructed by natural transformation of PMSS1 Δ*csd6* with genomic DNA from a *csd6* complemented strain generated in the *H. pylori* G27 strain background, TSH31 (Δ*csd6*::*cat McGee*:*csd6*:*aphA3*), where a wild-type copy of *csd6* (HPG27_477) was introduced at a previously characterized and neutral intergenic chromosomal site, the McGee locus (hp0203-0204 intergenic region) (Langford *et al*., 2006). In the *H. pylori* G27 strain, McGee is located between genes HPG27_186 and HPG27_187 and TSH31 carries a kanamycin resistance cassette (*aphA3*) gene (Sycuro *et al*., 2013). Genomic DNA from TSH31 was used for natural transformation of the PMSS1 Δ*csd6* strain. Transformants were selected on horse blood plates supplemented with kanamycin (25 μg mL^{-1}). The recipient strain (EPH1) was PCR confirmed using primers homologous to upstream and downstream flanking regions within HPG27_186 and HPG27_187 using the primers indicated in Table 5.2. The *csd6* complemented strain was then backcrossed once by isolating genomic DNA from EPH1 for natural transformation of PMSS1 Δ*csd6*. The resulting backcrossed clones were evaluated by PCR to confirm integration of *csd6* at McGee. At least three clones successfully showed integration at McGee and were renamed LMH12 clones 1-3. The clones were then checked for urease activity and motility, and were used for quantitative morphology analysis (as described below). Figure 5.8 shows morphology analysis of LMH12 clone 3 (*csd6* complemented strain), which was the strain used for single-strain infections in mice and for bacterial localization studies.

Transmission Electron Microscopy (TEM) of H. pylori cells

TEM of *H. pylori* was performed as described in Lowenthal *et al*., 2009, and cells were visualized with a JEOL JEM 1400 transmission electron microscope. Digital images were manipulated using Image J and Adobe Photoshop.

Morphology analysis

Wild-type *H. pylori* PMSS1 and shape mutants were grown in liquid culture to an optical density at 600 nm (O.D. $_{(600)}$) of 0.4 - 0.6. Bacteria were fixed (4% Paraformaldehyde, 1X PBS, and 25% Glycerol) and added to 0.1% poly-L-lysine (Sigma Aldrich) coated coverslips that were placed on a pre-cleaned microscope slide, and sealed with VaLP (1:1:1 Vaseline: Lanolin: Paraffin). Single focal plane images were collected using a 100 X ELWD Plan APO (NA 1.40

oil) objective mounted on a Nikon TE 200 microscope, equipped with a Nikon CoolSNAP HQ CCD camera controlled by MetaMorph software (MDS Analytical Technologies). Quantitative morphology analysis of manually thresholded phase-contrast images was performed as described in Sycuro *et al.* 2010 using the CellTool software program (Lacayo *et al.*, 2007; Pincus and Theriot, 2007; Sycuro *et al.*, 2010).

Ethics statement

All procedures involving animals were done under practices and procedures of Animal Biosafety Level 2 and carried out with strict accordance with the recommendations in the Guide for the Care and Use of Laboratory Animals of the National Institutes of Health. The facility is fully accredited by the Association for Assessment and Accreditation of Laboratory Animal Care and complies with the United States Department of Agriculture, Public Health Service, Washington State and local area animal welfare regulations. All activities were approved by the FHCRC Institutional Animal Care and Use Committee (IACUC).

Mouse colonization assay

4 - 6 week old female C57BL/6 mice were purchased from Jackson Laboratories (Maine, U.S.) and were certified free of endogenous *Helicobacter* infection by the vendor. All animals were maintained in autoclaved microisolator cages (1-5 mice per cage) and provided with standard chow and water ad libitum. Mice were infected with a single oral dose of 5×10^7 *H. pylori* cells/strain (0.1 mL) in the inocula using flexible gavage needles. The uninfected control group was gavaged with 0.1 mL of liquid culture media containing 90% (v/v) Brucella broth and 10% fetal bovine serum (BB10).

For the pilot experiment, mice were euthanized by inhalation of CO_2 and stomachs were harvested after one-day, one-week, and 1-4 months of infection (Fig. 5.2). Most of the non-glandular region (forestomach) was discarded since this region of the stomach is lined with squamous rather than glandular epithelium and *H. pylori* has not been shown to colonize this region of the stomach. However, *H. pylori* may colonize the interface between the squamous forestomach and glandular stomach where the corpus begins (the squamocolumnar junction). The regions of interest using *H. pylori* models of infection include the corpus, antrum, and the pyloric junction with the duodenum. Figures 5.2 and 5.4 show a whole longitudinal tissue cross-section that includes these regions of the stomach and serves as an example for the sections collected for immunofluorescence. Therefore, part of the forestomach was maintained and the glandular stomach (corpus and antrum) was opened along the greater curvature from the esophagus through the proximal duodenum.

Half the stomach was collected for CFU/gram and the other half of the stomach was fixed in 4% paraformaldehyde (PFA) (100 mM phosphate buffer (pH 7.4)) for immunofluorescence (to localize bacteria within the stomach) or fixed in 10% neutral buffered formalin (NBF) for histology (only tissue harvested after 1-4 months of infection) (Fig. 5.2). The food was carefully removed and the stomach was laid flat on an index card and placed in a cassette with a sponge at top, closed, and fixed in their respective solutions. For one day or one-week harvests, half the stomach was used for plating for CFU enumeration and the other half was fixed in 4% PFA for 1-2 hours or in Methacarn fixative (60% methanol: 30% chloroform: 10% glacial acetic acid) for 48-72 hrs for mucus-preservation and immunofluorescence. Methacarn is not a cross-linking fixative and does not preserve well host cellular structure or bacteria, but it provides efficient preservation of carbohydrate constituents in mucus (Puchtler *et al*., 1970).

For the second experiment (Fig. 5.3B), the methods differed by a few modifications. To collect adjacent tissues samples for bacterial load, immunofluorescence, and histology, the stomach was divided in thirds. A third of the stomach was collected to measure CFU/gram of stomach load, a third was fixed in 4% PFA (100 mM phosphate buffer (pH 7.4)) for immunofluorescence, and a third was fixed in 10% NBF for histology of 15 mice per group.

For CFU counts, one-half or one-third stomachs were manually homogenized using a pestle in 0.5 mL of BB10. Dilutions of stomach homogenate were plated on solid horse blood agar plates containing 4% Columbia agar base (Oxoid, Hampshire, UK), 5% defibrinated horse blood (HemoStat Labs, Dixon, CA) 0.2% β-cyclodextrin (Sigma, St. Louis, MO), 10 μg mL^{-1} vancomycin (Sigma), 5 μg mL^{-1} cefsulodin (Sigma), 2.5 U/mL polymyxin B (Sigma), 5 μg mL^{-1} trimethoprim (Sigma), 8 μg mL^{-1} amphotericin B (Sigma), and bacitracin (200 μg mL^{-1}) to eliminate normal mouse microbiota growth, and incubated at 37°C using a tri-gas incubator (10% CO_2, 10% O_2; Thermo Scientific) for 4-5 days.

Preparation of H. pylori for 3D-image analysis

Wild-type *H. pylori* PMSS1 bacteria was grown in liquid culture to an optical density at 600 nm (O.D. $_{(600)}$) of 0.4 - 0.6. A 1 mL of bacterial culture was harvested in a 1.5 mL microcentrifuge tube and centrifuged at 5,000 rpm for 5 min. The cell pellet was resuspended in 100-200 μL of 4% paraformaldehyde (in 100 mM phosphate buffer (pH 7.4)) and fixed for at least an hour at room temperature. Bacteria were then embedded in 4% agarose (ultra pure low-melting point agarose, Invitrogen) prepared in 1X phosphate-buffered saline (pH 7.4) (Gibco). The agarose solution was first cooled down to ~55 - 65°C and then aliquotted into 1.5 mL microcentrifuge tubes. Aliquots of fixed bacteria were immediately added and gently resuspended into the solution before it solidified. The solidified slabs were gently removed by insertion of a metal spatula on the side of the tube. The slabs were then sectioned using a vibratome (Leica VT 1200 S fully automated vibrating blade microtome, Leica Biosystems - Germany) to generate 100 μm thick sections. Sections were permeabilized in blocking buffer (3% bovine serum albumin (Sigma Aldrich); 1% Saponin (Sigma Aldrich); 1% Triton X-100 (Sigma Aldrich)) in 1X PBS and immunostained with primary anti-*H. pylori* polyclonal antibody (1:1,000 dilution) (Howitt *et al*., 2011) overnight at 4°C (Table 5.3). A goat anti-rabbit Alexa Fluor-488 conjugate (1:2,000) (Molecular Probes) was used to visualize *H. pylori* (Table 5.3), and samples were incubated in the secondary antibody for 2 hrs at room temperature. Sections were then washed 3-5X with blocking buffer and then mounted onto standard glass microscope slides with secure imaging spacers (9 mm in diameter x 0.12 mm depth, Electron Microscopy Sciences). Pro-Long Diamond Antifade medium was added (Molecular Probes) before mounting on coverslips.

Confocal microscopy, 3-D imaging, and volumetric analysis of H. pylori cells

Samples were imaged using a Zeiss LSM 780 NLO confocal and multi-photon microscope (EC Plan-Neofluar 40 X/1.30 DIC M27 or Plan-Apochromat 63 X/1.40 DIC M27 oil immersion objective lens) with ZEN acquisition software program (2013). Z-stacks were generated with a slice interval of 0.5 μm. The Volocity 3D-image analysis software program (Volocity v6.3, Perkin Elmer, Inc., Waltham, MA, USA) was used to import Z-stacks, generate 3-D images, and analyze individual bacterial cells based on their fluorescence intensity (ranging from 30-255) and total volume (μm^3) (minimum volume criteria = 3.5 μm^3).

Immunofluorescence of thick longitudinal tissue sections

Tissues from murine stomachs were processed for confocal immunofluorescence microscopy as described in Howitt *et al*., 2011 and Sigal *et al*., 2015, with minor modifications. Gastric tissue was fixed in 2-4% paraformaldehyde in 100 mM phosphate buffer (pH 7.4) for 2 hours at room temperature. Tissue was embedded in 4% agarose in 1X phosphate-buffered saline (PBS) (pH 7.4) (Gibco) and sectioned using a vibratome to generate 100 – 200 μm thick longitudinal sections that include the limiting ridge at the forestomach/ glandular junction to the pyloric junction with the duodenum (Fig. 5.4). Tissue sections were then permeabilized in blocking buffer (3% bovine serum albumin (Sigma Aldrich); 1% Saponin (Sigma Aldrich); 1% Triton X-100 (Sigma Aldrich)) in 1X PBS (pH 7.4) (Gibco). Anti-*H. pylori* polyclonal antibody (1:1,000 dilution) was used to immunostain *H. pylori* (Table 5.3). Anti-MUC5AC monoclonal antibody (clone 45M1) (1:400) was used to stain mucin for those samples fixed in Methacarn (Table 5.3). The tissue and primary antibodies were incubated overnight at 4^{o}C. The sections were then washed 5X with blocking buffer and a goat anti-rabbit Alexa Fluor-647 conjugate (1:2,000) was used to visualize bacteria in tissue (Molecular Probes). 4', 6-Diamidino-2-phenylindole (DAPI) (0.1 μg mL^{-1}) was used to stain nuclei, and goat anti-mouse Alexa-Fluor-555 conjugate was used to visualize MUC5AC (1:1,000) (Table 5.3). The tissue was incubated with DAPI and appropriate secondary antibodies in blocking buffer for 2 hrs at room temperature. The sections were then washed 5X with blocking buffer and mounted onto standard glass microscope slides with secure imaging spacers (20 mm in diameter x 0.12 mm thick, Electron Microscopy Sciences) or hand-made imaging spacers using parafilm (0.12 mm thick). Pro-Long Diamond Antifade medium was added (Molecular Probes) before mounting on coverslips.

Confocal microscopy, 3-D imaging, and volumetric analysis to quantitate bacteria within gastric tissue

Tissue samples were imaged with a Zeiss LSM 780 NLO confocal and multi-photon microscope with a 40 X oil immersion objective lens (EC Plan-Neofluar 40 X/1.30 oil) and Z-stacks (355 μm wide) were generated using the ZEN acquisition software program (2013). Images were acquired at a frame size of 1,024 x 1,024 with 8-bit depth and at a frame rate speed of 8 frames per second. Z-stacks were generated with a slice interval of 0.5 μm. For each tissue section, multiple Z-stacks (ranging from 25-30) were acquired in order to capture the full length of longitudinal tissue sections and to include the limiting ridge of the forestomach to the glandular junction to the pyloric junction with the duodenum (Fig. 5.4). For all Z-stacks, we acquired a collection of non-overlapping images by manual translation of the microscope stage (see example in Fig. 5.4A).

Volumetric analyses and quantitation of H. pylori in the murine stomach

Quantitation of *H. pylori* within individual gastric glands was performed using the Volocity 3D-image analysis software program as described in Howitt *et al.*, 2011 and Sigal *et al.*, 2015 with minor modifications. 3D-reconstructed images were imported onto Volocity and the total volume (μm^3) for individual bacterial cells was determined. The mean volume for a bacterium (10 μm^3) was used to calculate the total number of bacteria near or at the surface epithelium and within gastric glands. The same measurement protocol was applied across all tissue samples analyzed for wild-type *H. pylori* bacteria and straight rods.

Analysis of 3 sections (>500 μm apart) showed consistent results in bacterial number counts. Our bacterial localization studies included analysis of 1-3 sections per infected mouse.

One section was analyzed per mouse after a day of infection; three sections were analyzed per mouse after a week of infection, and only one section was examined per mouse after 4 months of infection.

Histopathologic examination of H. pylori infected murine stomachs

Gastric tissue was fixed in 10% NBF (Thermo Fisher Scientific). Samples were paraffin embedded, sectioned, and stained with Hematoxylin and Eosin (H&E) by the Experimental Histopathology Core at the Fred Hutchinson Cancer Research Center. Slides were interpreted and scored by a Veterinary Pathologist (Sue Knoblaugh at the Ohio State University) in a blinded manner as described in Rogers *et al*., 2005 and Houghton (2012). The pathologist evaluated two mice samples per group (uninfected, wild-type, Δ*csd1*, or Δ*csd6*-infected samples) after 1, 2, and 4 months of infection (Fig. 5.12A). She identified several sections per mouse that had complete longitudinal sections from the limiting ridge at the forestomach/glandular stomach junction to the pyloric junction with the duodenum. Only the most severely affected sections were evaluated and the corpus and antrum were scored separately for the following six criteria and categories: (a) inflammation, (b) epithelial defects, (c) oxyntic atrophy, (d) hyperplasia, (e) pseudopyloric metaplasia, and (f) dysplasia as based from the histologic scoring criteria and evaluation of *H. pylori* infected murine samples published by Rogers *et al*., 2005 and in Houghton (2012). Only inflammation and hyperplasia was observed at the corpus/antral junction and the antrum. No histologic perturbations were observed in the corpus at any time-point. The scoring scheme for inflammation and hyperplasia is summarized in Table. 5.4.

Statistical analyses

We used the Kolmogorov-Smirnov (K-S) statistics tool in CellTool to assay the differences in cell shape morphology, including cell length and side curvature distributions, as described in detail in Sycuro *et al*. (2010, 2012). To make statistical comparisons between wild-type and mutant stomach colonization loads (CFU/gram of stomach), unpaired non-parametric Kolmogorov-Smirnov (K-S) tests were performed using GraphPad Prism version 6.00 for Windows or Mac (GraphPad Software, La Jolla, CA USA). For each comparison, a K-S p-value less than or equal to 0.05 was considered significant, and ns, denotes no significant difference.

TABLES

Table 5.1. Bacterial strains used in this chapter.

Strain Name	**Genotype or Description**	**Shape phenotype**	**Reference or Source**
PMSS1	Wild-type *H. pylori*	helical	Lee *et al*., 1997; Arnold *et al*., 2011
LMH1	Δ*csd1::cat* in PMSS1	curved and variable morphologies	This study
LMH6	Δ*csd6::cat* in PMSS1	straight	This study
TSH31	Δ*csd6*::*cat* *McGee*:*csd6*:*aphA3* in LSH100	helical and straight morphologies	Sycuro *et al*., 2013
EPH1	*csd6* complemented strain: Δ*csd6*::*cat McGee:csd6 :aphA3* in PMSS1	helical	This study
LMH12	*csd6* complemented strain: EPH1 backcrossed in PMSS1	helical	This study

Table 5.2. Primers used in this chapter.

Gene name	***H. pylori* gene annotation**	**Primer**	**Sequence**
Targeted disruption primers			
csd1	HPG27_1481[a] (HP1543)[b]	HPG27_1482 Forward	GCGAGCGCTGATGGGATTGTG
		HPG27_1480 Reverse	ATATTCTTAGGGCGAGTCTCCC
csd6	HPG27_477[a] (HP0518)[b]	HPG27_476 Forward	gcgcgctctag AAGGAAGAAAAGAGCTTGC[c]
		HPG27_478 Reverse	GCTGGTAGGCTTTGTAATC
Complementation primers			
csd6 at McGee locus[d]	Δ*csd6*::*cat McGee:csd6 :aphA3* in PMSS1	McGee locus Forward	GAGCGAGAATTCAAAGACAACCCCA
		McGee locus Reverse	GGCGATGGGGCTGGGGCGTGCGTGA TAGGC

[a] Gene annotation in the human clinical isolate G27 (Baltrus *et al*., 2009).
[b] Gene annotation in the human clinical isolate 26695 (Tomb *et al*., 1997).
[c] Gene specific sequences are in uppercase and sequences added for cloning are in lower case.
[d] McGee Locus: intergenic sequence located between HPG27_186 and HPG27_187 (*H. pylori* strain G27 (Baltrus *et al*., 2009)).

Table 5.3. Antibodies and reagents used for immunofluorescence.

Antibody	Dilution	Resource
Primary anti-*H. pylori* polyclonal antibody (rabbit)	1:1,000	Gift from Dr. Manuel Amieva, Stanford University (Howitt *et al*., 2011)
Monoclonal anti-mucin gastric antibody produced in mouse (clone 45M1) (anti-MUC5AC)	1:400	Sigma Aldrich, M5293
Goat anti-Rabbit IgG (H+L) secondary antibody, Alexa Fluor-488 conjugate	1:2,000	Molecular Probes, A-11034
Goat anti-Rabbit IgG (H+L) secondary antibody, Alexa Fluor-647 conjugate	1:2,000	Molecular Probes, A-21244
Goat anti-Mouse IgG (H+L) secondary antibody, Alexa Fluor-555 conjugate	1:1,000	Molecular Probes, A-21422
4’, 6-Diamidino-2-phenylindole (DAPI)	0.1 μg mL^{-1}	Molecular Probes, D-1306

Table 5.4. Histopathologic scoring scheme for inflammation and hyperplasia in mice chronically infected with *H. pylori*.

Score	Inflammation	Hyperplasia
0	No inflammation	No hyperplasia
1	Mild patchy or multifocal islands	Mild elongation of mucosa
2	Moderate coalescing infiltrate	Increased surface epithelium 2X normal length
3	Moderate to severe sheets in mucosa and/or submucosa	Increased surface epithelium 3X normal length
4	Severe florid inflammation into muscularis	Increased surface epithelium 4X normal length +/- dysplasia

FIGURES

A

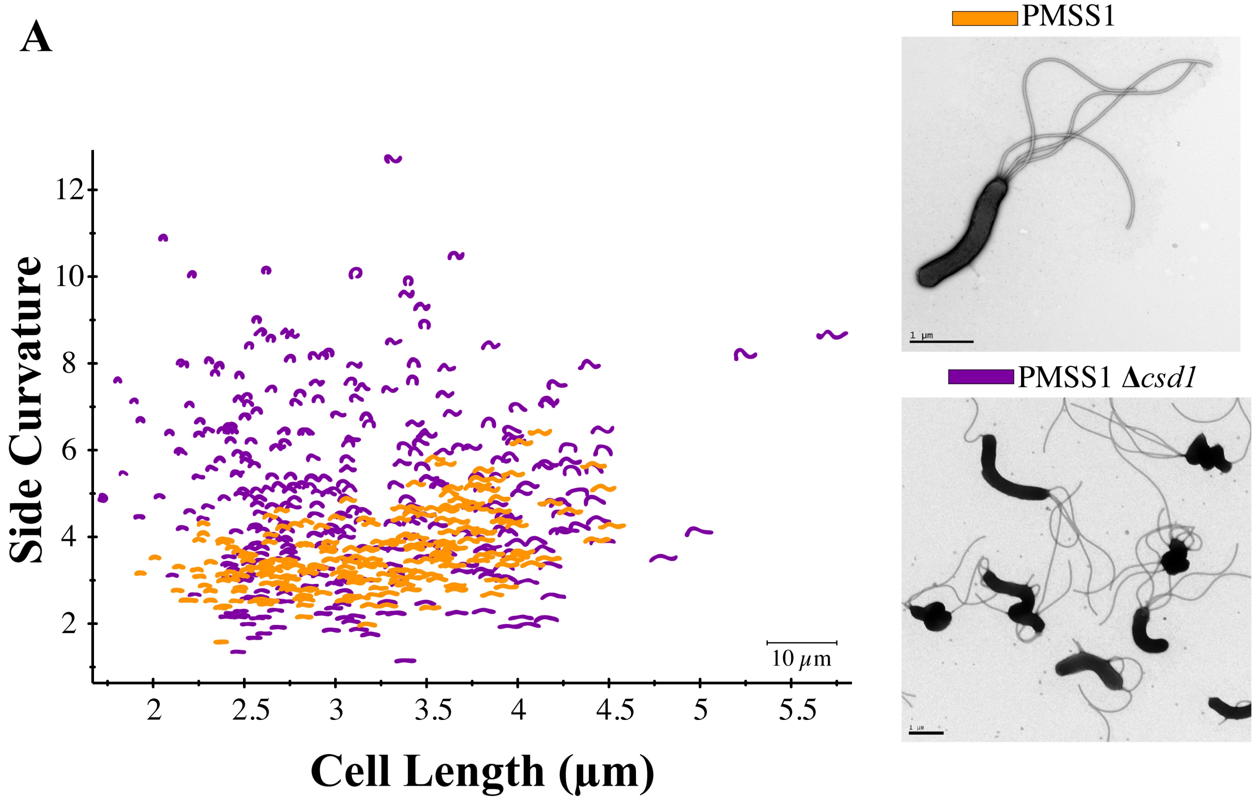
PMSS1
PMSS1 Δ*csd1*
1 μm
Side Curvature
12
10
8
6
4
2
10 μm
2
2.5
3
3.5
4
4.5
5
5.5
Cell Length (μm)

B

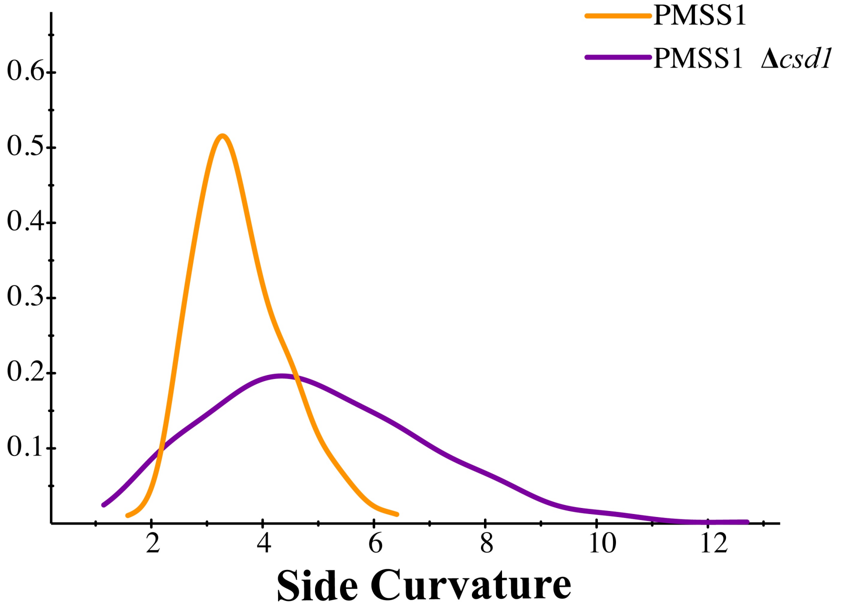
PMSS1
PMSS1 Δ*csd1*
0.6
0.5
0.4
0.3
0.2
0.1
2
4
6
8
10
12
Side Curvature

Figure 5.1. Deletion of *csd1* results in curved and variable morphologies. **(**A) Scatter plot arraying the wild-type PMSS1 (orange, n=218) and isogenic Δ*csd1* mutant (purple, n=325) populations by cell length (μm) and side curvature (arbitrary units). Morphologies of single cells were captured from 100 X (oil immersion objective lens) phase contrast images of each strain using the CellTool software program (Zachary Pincus, St. Louis, MO, USA). Inset panel shows TEM images of PMSS1 at 4,000 X and Δ*csd1* at 2,000 X. Scale bar = 1 μm. (B) Smooth histogram summarizing the side curvature distributions acquired for each strain shown in A. Significant differences in side curvature distributions were observed between wild-type PMSS1 and Δ*csd1* ($p<0.00001$) (Kolmogorov-Smirnov (K-S) statistics of side curvature distributions). Strains used: PMSS1 and LMH1.

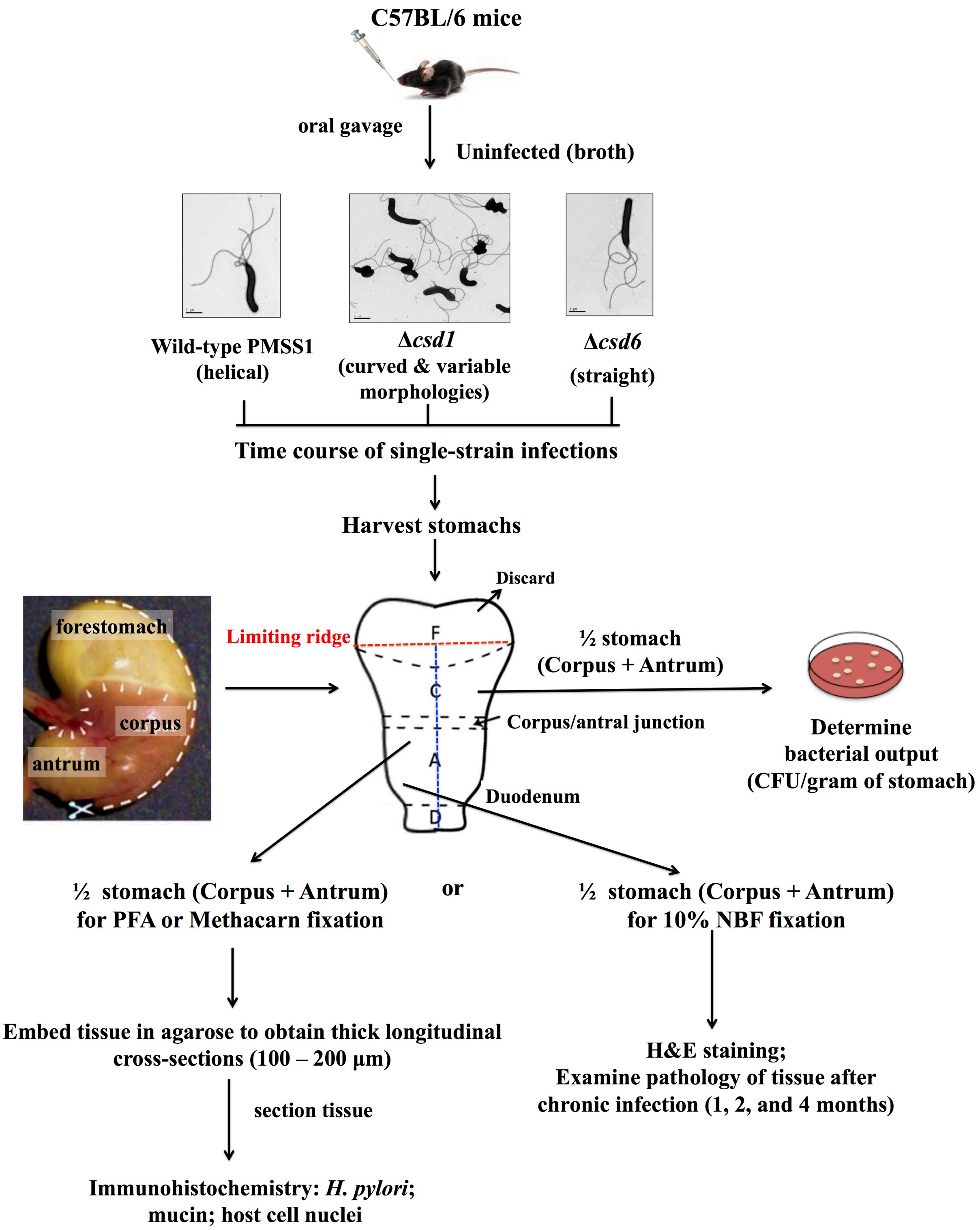

Figure 5.2. Mouse stomach colonization assay. A representative schematic for our pilot experiment is shown where C57BL/6 mice were orally gavaged with broth (uninfected), wild-type PMSS1 bacteria, curved rod (Δ*csd1*) or straight rod (Δ*csd6*) mutants (5 mice per group).

The pilot study included a time course to capture initial colonization (1 day and 1 week) and chronic infection (1, 2, and 4 months), at which point their stomachs were harvested. The stomach was opened along the greater curvature and sectioned in halves. After a day or week of infection, one-half of the stomach was used to measure bacterial output (CFU/gram of stomach load) (mice 1-5), and one-half was fixed in 4% paraformaldehyde (PFA) (mice 1-3) or Methacarn (mice 4-5) per group for immunofluorescence. For long-term infections (1, 2, and 4 months), one-half of the stomach was used to measure bacterial output (CFU/gram of stomach load), and one-half of the stomach was fixed in 4% PFA (mice 1-3) or 10% neutral buffered formalin (NBF) (mice 4-5) for histology. Portions of this figure were adapted from Rolig *et al.* (2012) and Eberle *et al.* (2013).

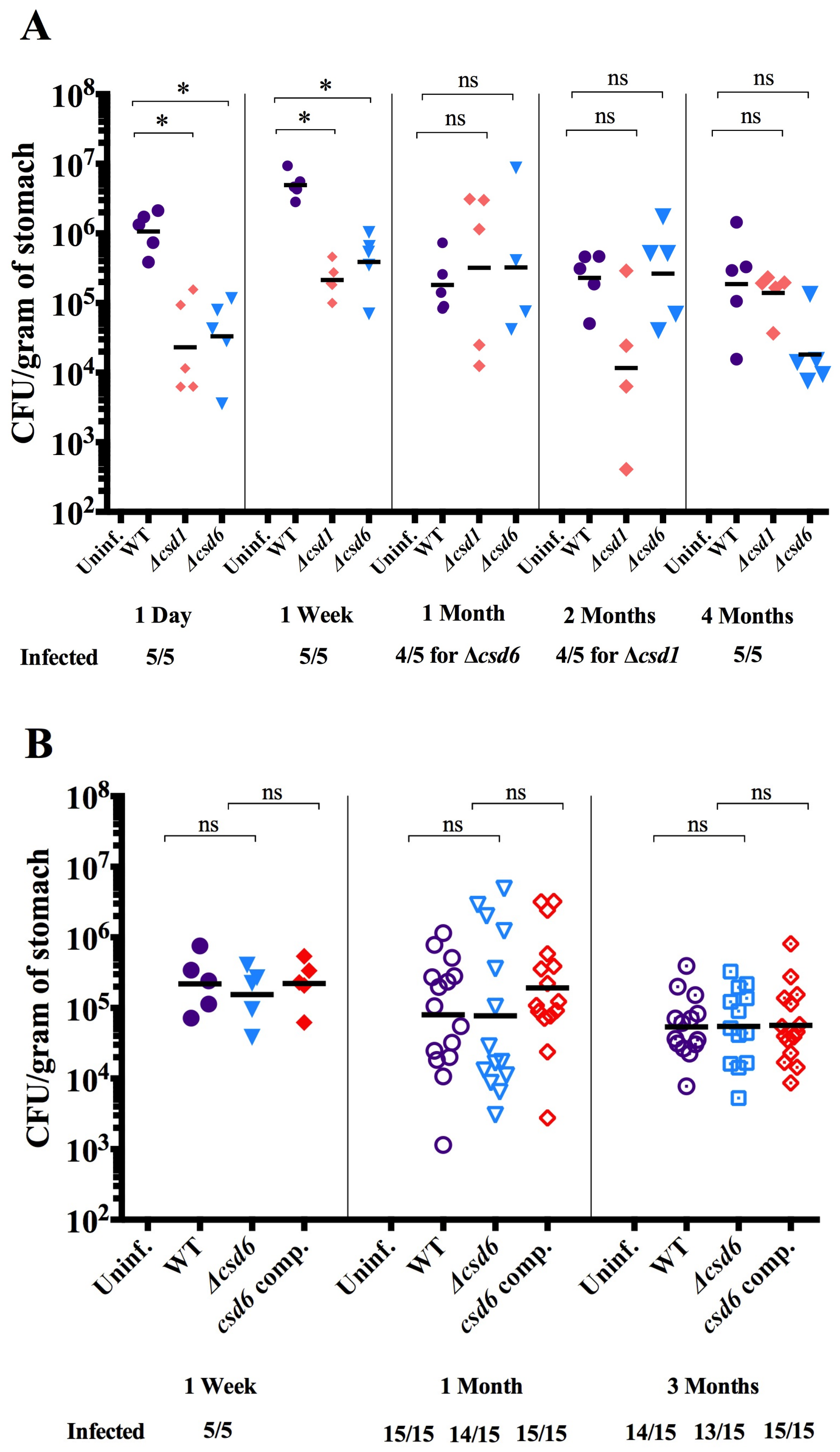
A
CFU/gram of stomach
10^8
10^7
10^6
10^5
10^4
10^3
10^2
*
*
*
*
ns
ns
ns
ns
ns
ns
Uninf.
WT
Δcsd1
Δcsd6
1 Day
1 Week
1 Month
2 Months
4 Months
Infected
5/5
5/5
4/5 for Δcsd6
4/5 for Δcsd1
5/5
B
CFU/gram of stomach
10^8
10^7
10^6
10^5
10^4
10^3
10^2
ns
ns
ns
ns
ns
ns
Uninf.
WT
Δcsd6
csd6 comp.
1 Week
1 Month
3 Months
Infected
5/5
15/15
14/15
15/15
14/15
13/15
15/15

Figure 5.3. Cell shape mutants show early colonization deficiencies in the mouse stomach but persistently colonize the stomach over time. (A) Pilot time course of single-strain infections with wild-type, Δ*csd1*, and Δ*csd6*. Each point represents the load in CFU/gram of 1/2-stomachs per single mouse. In some cases, mice cleared the mutant bacteria (1 month and 2 months). (B) Single-strain infections with wild-type, Δ*csd6*, and the *csd6* complemented strain. Each point represents the load in CFU/gram of 1/3-stomachs per single mouse. 15 mice were infected per group for long-term infection (1 and 3 months). In some cases, mice cleared the bacteria. Black bars are the geometric means. Asterisks (*) denote significant differences between wild-type and mutant in stomach colonization load (CFU/gram of stomach tissue) where $p<0.05$ using a Kolmogorov-Smirnov nonparametric test and ns = no significant difference. Strains used: PMSS1, LMH1, LMH6, and LMH12.

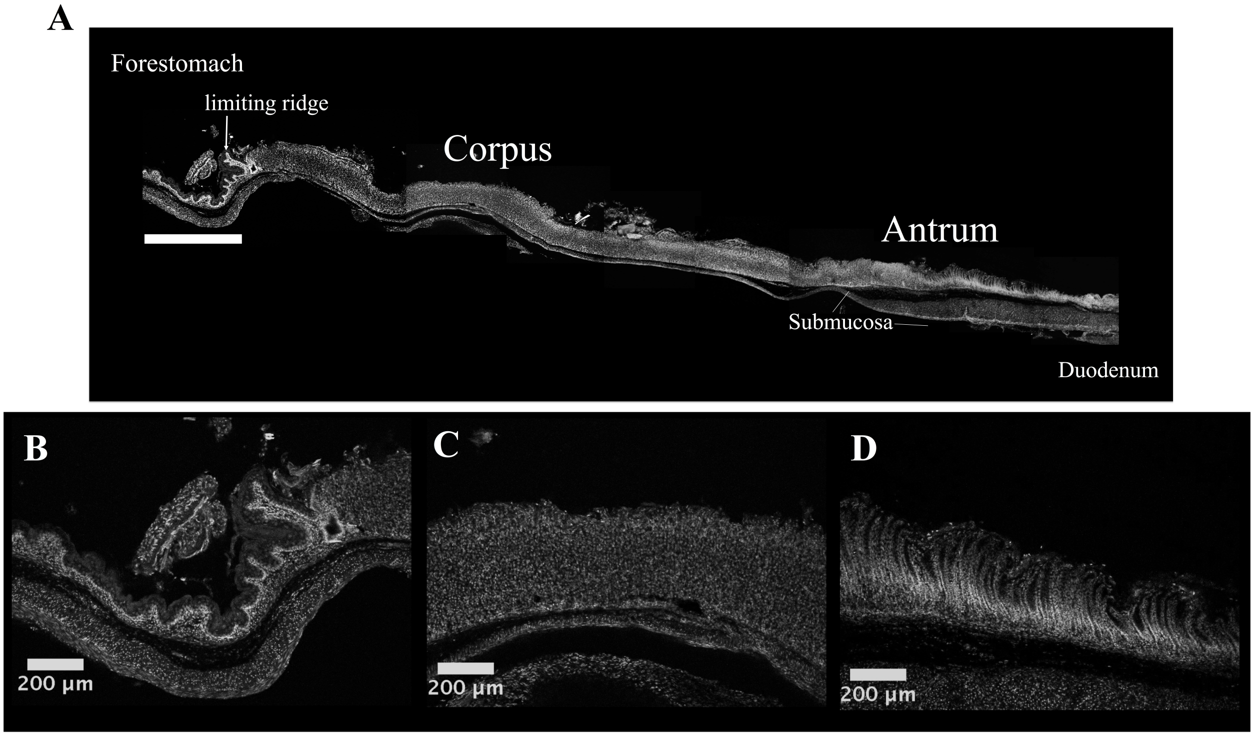

Figure 5.4. Composite confocal microscopy image of a week-long infected (wild-type) longitudinal gastric tissue section. (A) The image shows serial adjacent non-overlapping fields of view (1417 µm wide, 10 X objective) stitched together to generate a whole longitudinal section from the limiting ridge at the forestomach with the glandular stomach junction (also referred to as the squamocolumnar junction) to the pyloric junction with the duodenum. Scale bar = 1,000 µm (white bar). The tissue was fixed in 4% paraformaldehyde and was stained for nuclei with DAPI (white) to show architectural structure of the different regions of the stomach. (B-D) Magnified views of image A showing the limiting ridge (B), corpus (C), and antral glands (D). Scale bar = 200 µm (white). Features of the limiting ridge were used to locate the glandular stomach junction with the corpus. Images C and D show distinctions between corpus and antral gastric glands, where corpus glands are taller.

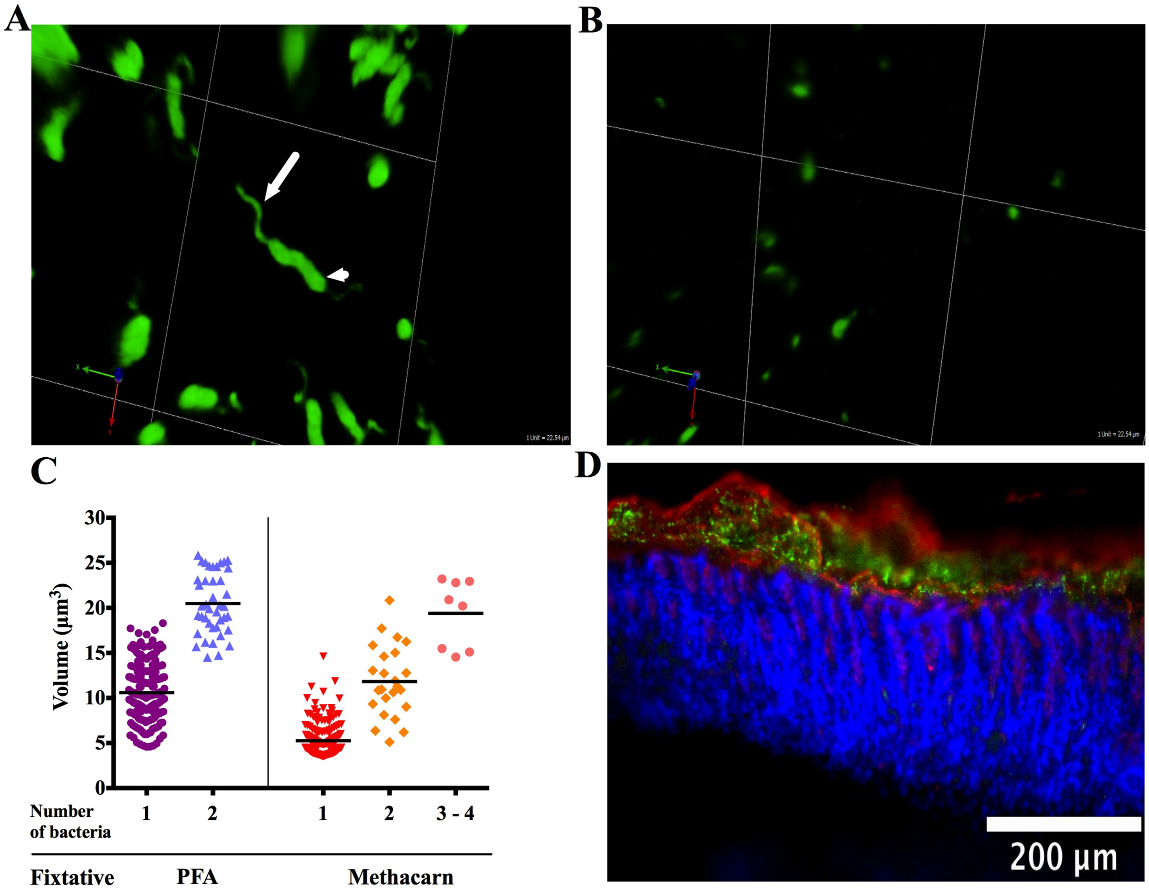

Figure 5.5. 3D-visualization of *H. pylori* and volumetric analysis of individual bacterial cells. 3-dimensional images of wild-type PMSS1 bacteria (green) fixed in 2% paraformaldehyde (PFA) (A) or Methacarn (B) were embedded in 4% agarose and sectioned to generate 200 µm thick sections. 3D-images were generated from Z-stacks collected at 63 X (oil-immersion objective) with a Zeiss LSM 780 confocal microscope. In A, the arrowhead points to the cell body and the arrow to a flagella bundle. (C) Volumetric analysis of individual bacterial cells fixed in 2% PFA (n= 203) or Methacarn (n=193). Black bars indicate the mean volume per bacterium (1); two bacteria (2); or multiple bacteria (3-4). Results are from one of two experiments. (D) One-week infected tissue with wild-type PMSS1 bacteria that was fixed in Methacarn to preserve mucus. The image was acquired at 20 X using a Zeiss LSM 780 confocal microscope. Scale bar = 200 µm. Staining is shown for *H. pylori* (green), mucin MUC5AC (red), and host cell nuclei (blue).

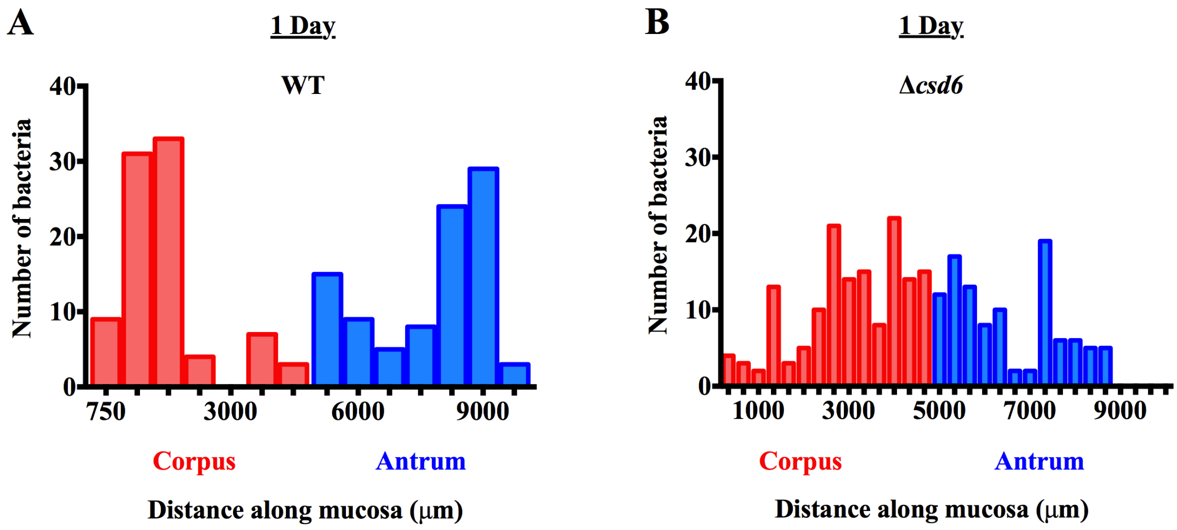

Figure 5.6. Wild-type bacteria and straight rods show similar localization to the corpus and antrum after a day of infection. Quantitation of wild-type bacteria (A) and straight rods (Δ*csd6*) (B) present after a day of infection along the whole longitudinal section from the limiting ridge at the forestomach/ glandular stomach junction to the pyloric junction with the duodenum. Volumetric analysis of Z-stacks (Volocity) was used to quantify the number of bacteria present in adjacent non-overlapping fields of view acquired at 20 X for A (710 μm wide) and at 40 X for B (355 μm wide) with a Zeiss LSM 780 confocal microscope. Bar histograms summarize the number of bacteria found within each field of view for the corpus (red) and the antrum (blue). Results are for a single tissue section analyzed from an infected mouse per strain. The bacterial load of the wild-type-infected mouse was $7.4\text{x}10^5$ CFU/gram of stomach, and the load for the Δ*csd6*-infected mouse was $1.2\text{x}10^5$ CFU/gram of stomach.

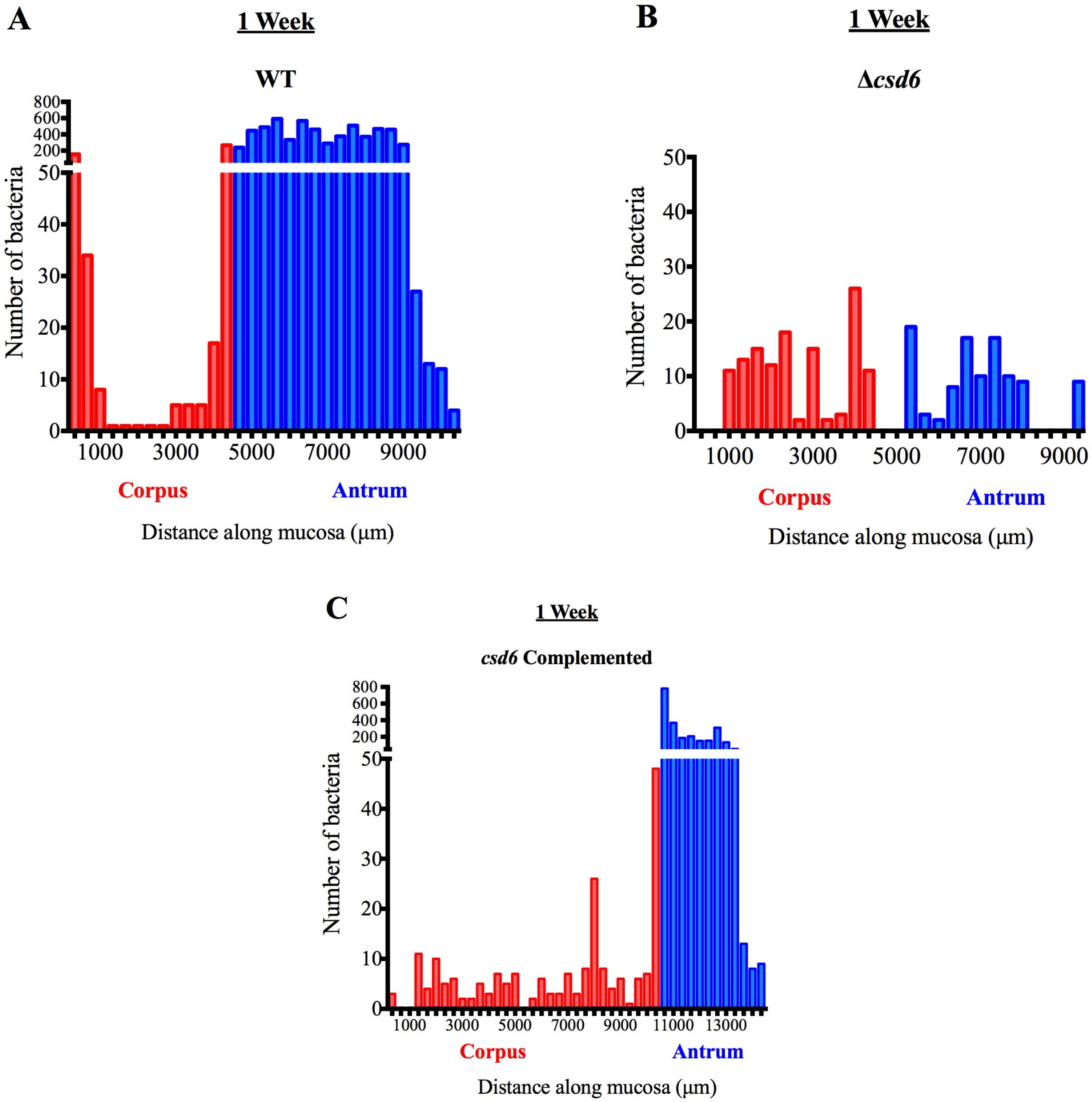

Figure 5.7. Straight rods show impaired penetration of antral glands and show similar tropism for the corpus and antrum after a week of infection. Quantitation of wild-type bacteria (A), straight rods (Δ*csd6*) (B), and *csd6* complemented bacteria (C) present after a week of infection along the mucosa, as described in Fig. 5.6. Results are for a single tissue section analyzed from an infected mouse per strain. The bacterial load of the wild-type-infected mouse was 2.8×10^6 CFU/gram of stomach; the load for the Δ*csd6*-infected mouse was 1.0×10^6 CFU/gram of stomach; and the load for the mouse infected with the *csd6* complemented strain was 5.4×10^5 CFU/gram of stomach.

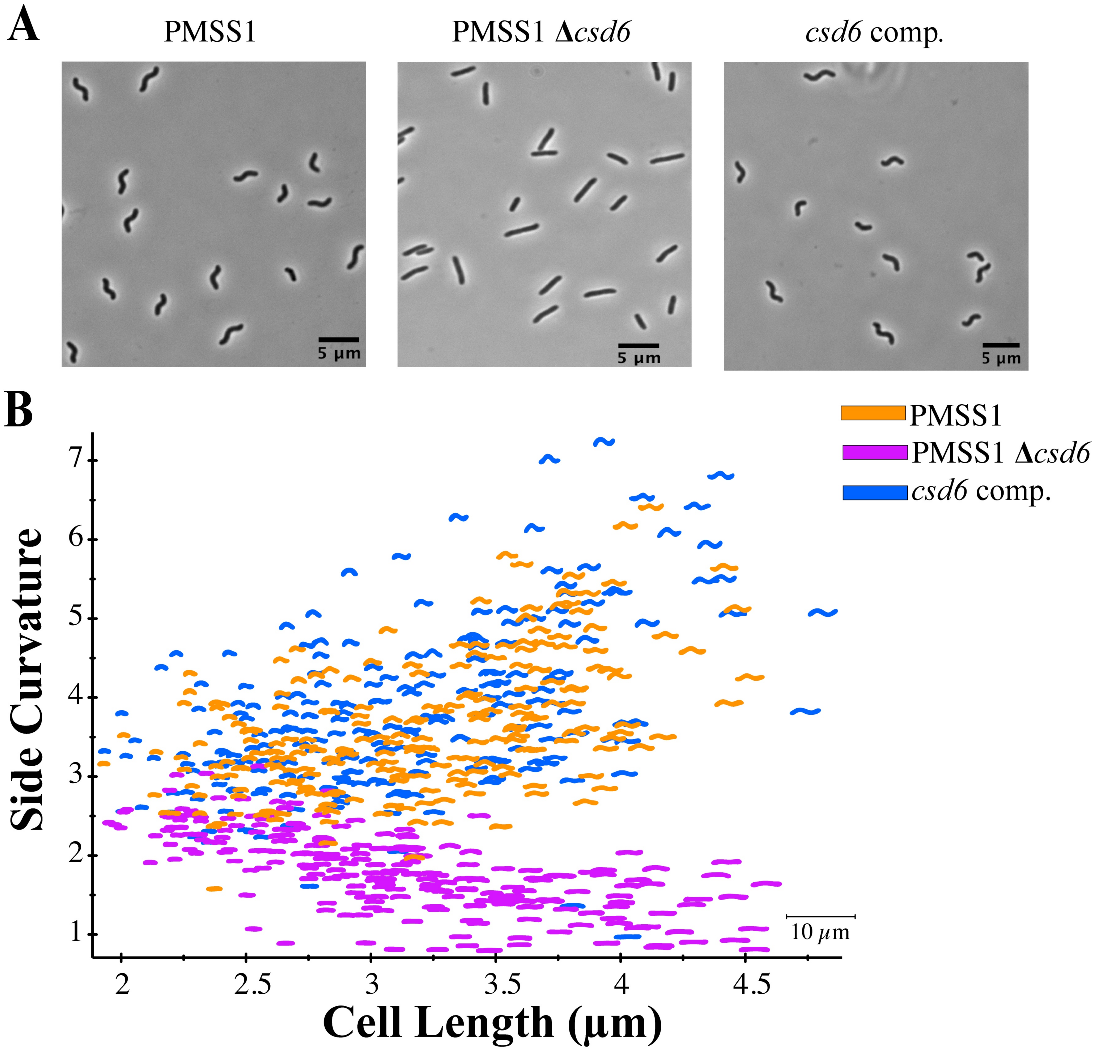
A
PMSS1
PMSS1 Δ*csd6*
csd6 comp.
5 µm
5 µm
5 µm
B
PMSS1
PMSS1 Δ*csd6*
csd6 comp.
Side Curvature
1
2
3
4
5
6
7
Cell Length (µm)
2
2.5
3
3.5
4
4.5
10 µm

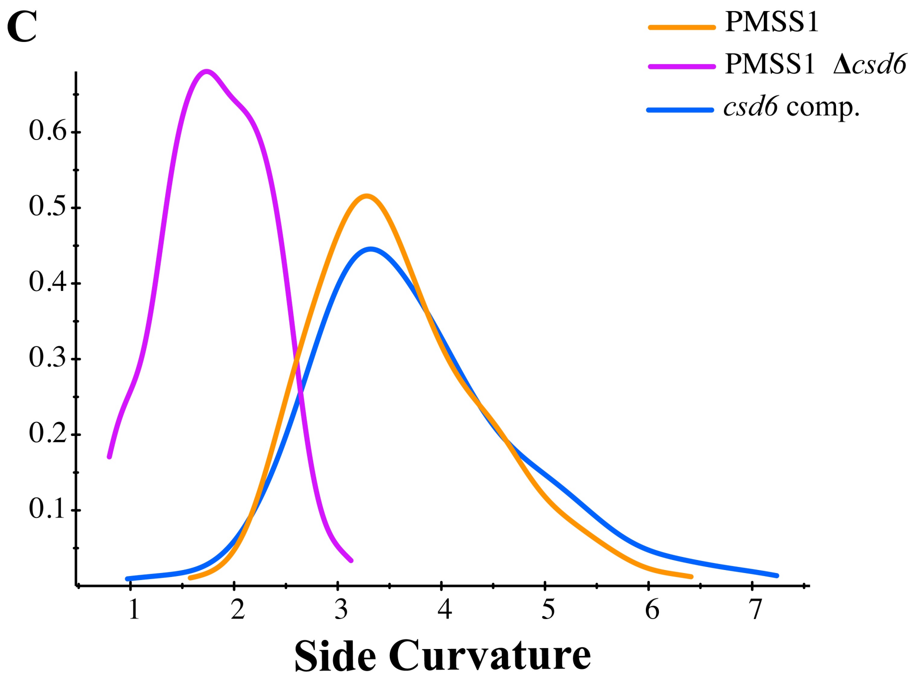

Figure 5.8. Complementation of *csd6* restores helical cell shape. (A) Phase contrast images of wild-type PMSS1 bacteria, the straight rod mutant (Δ*csd6*), and *csd6* complemented bacteria. Images were acquired at 100 X (oil immersion objective). Scale bar = 5 μm. (B) Side curvature vs. cell length (μm) for individual bacterial cells imaged using phase contrast microscopy of wild-type PMSS1 (orange, n=218), Δ*csd6* (magenta, n=230), and the *csd6* complemented strain (blue, n=212). (C) Smooth histograms summarizing the side curvature distributions acquired for each strain shown in B. No significant difference in side curvature distributions were observed between wild-type and the *csd6* complemented strain (p =0.64078) using the K-S statistics of side curvature distributions. Significant differences in side curvature distributions were observed between wild-type and Δ*csd6*, and between Δ*csd6* and the *csd6* complemented strain, where p<0.00001. Strains used: PMSS1, LMH6, and LMH12.

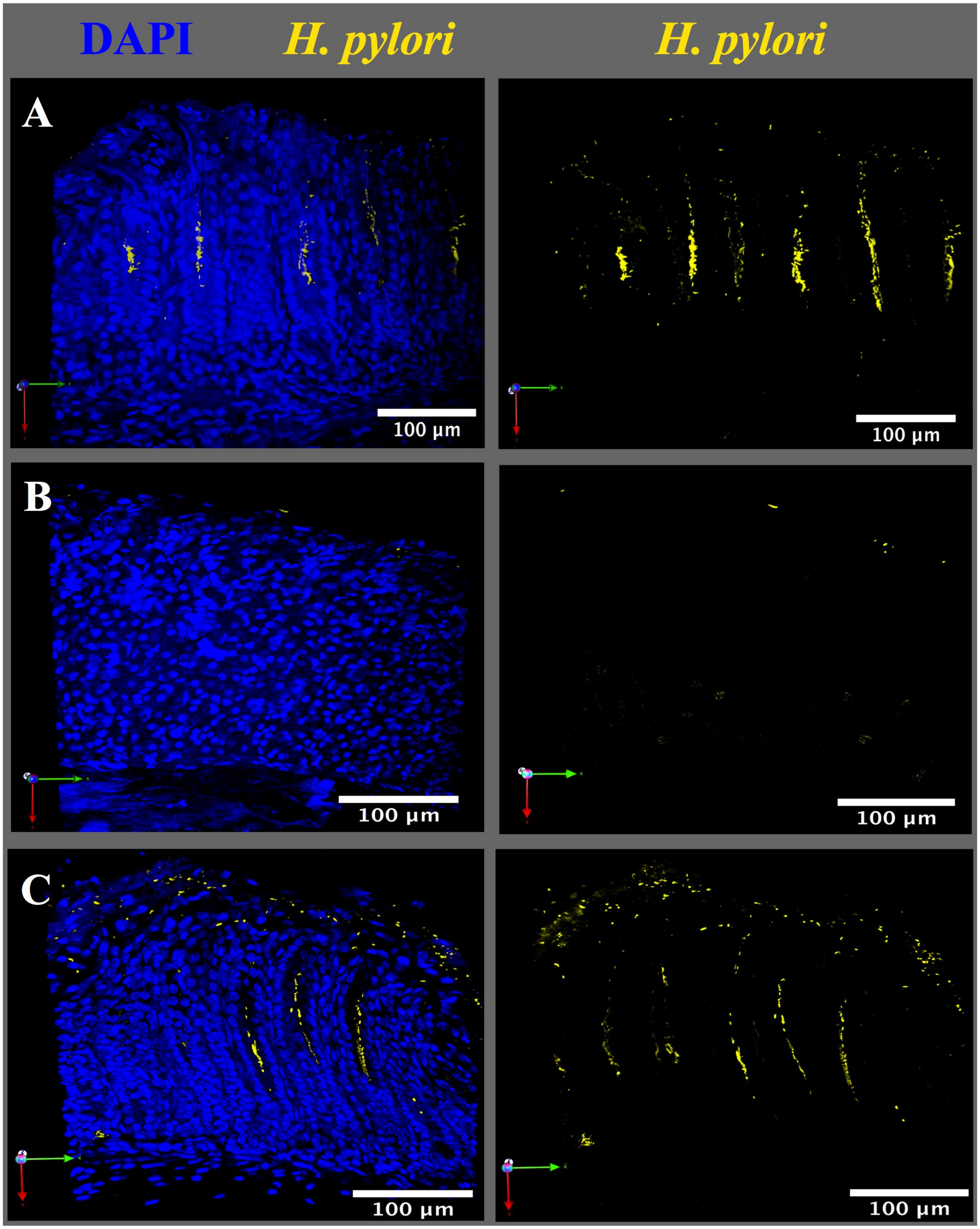

Figure 5.9. 3D-visualization of gastric gland colonization by *H. pylori* reveals colonization deficits for straight rod mutants after one week. Z-stack projections of wild-type bacteria (A), straight rods (Δ*csd6*) (B), and *csd6* complemented bacteria (C) present in antral glands after a week of infection. Images show single fields of view acquired from longitudinal thick sections

for each (120 μm thick, 355 μm wide) using a 40 X oil objective lens. Tissue samples were fixed in 4% paraformaldehyde, stained with DAPI (blue) for nuclei, and immunostained with anti-*H. pylori* polyclonal antibody and a secondary Alexa-Fluor 647 conjugate for *H. pylori* visualization (gold). Left panel: both channels and right panel: *H. pylori* only. The images were taken from the tissue sections analyzed and shown in Figure 5.7.

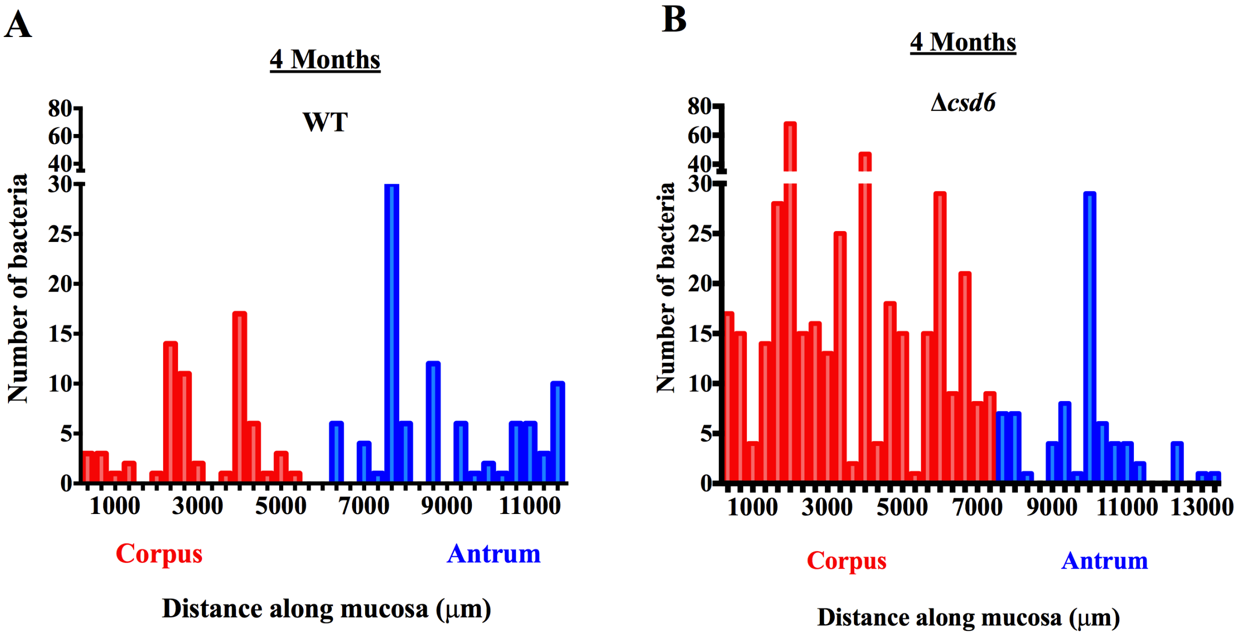

Figure 5.10. At 4 months, straight rods show higher corpus gland colonization than wild-type. Quantitation of wild-type bacteria (A) and straight rods (Δ*csd6*) (B) present after four months of infection along the mucosa, as described in Figure 5.6. Results are for a single tissue section analyzed from an infected mouse per strain. The bacterial load of the wild-type-infected mouse was 1.6x10^4 CFU/gram of stomach, and the load for the Δ*csd6*-infected mouse was 1.5x10^4 CFU/gram of stomach.

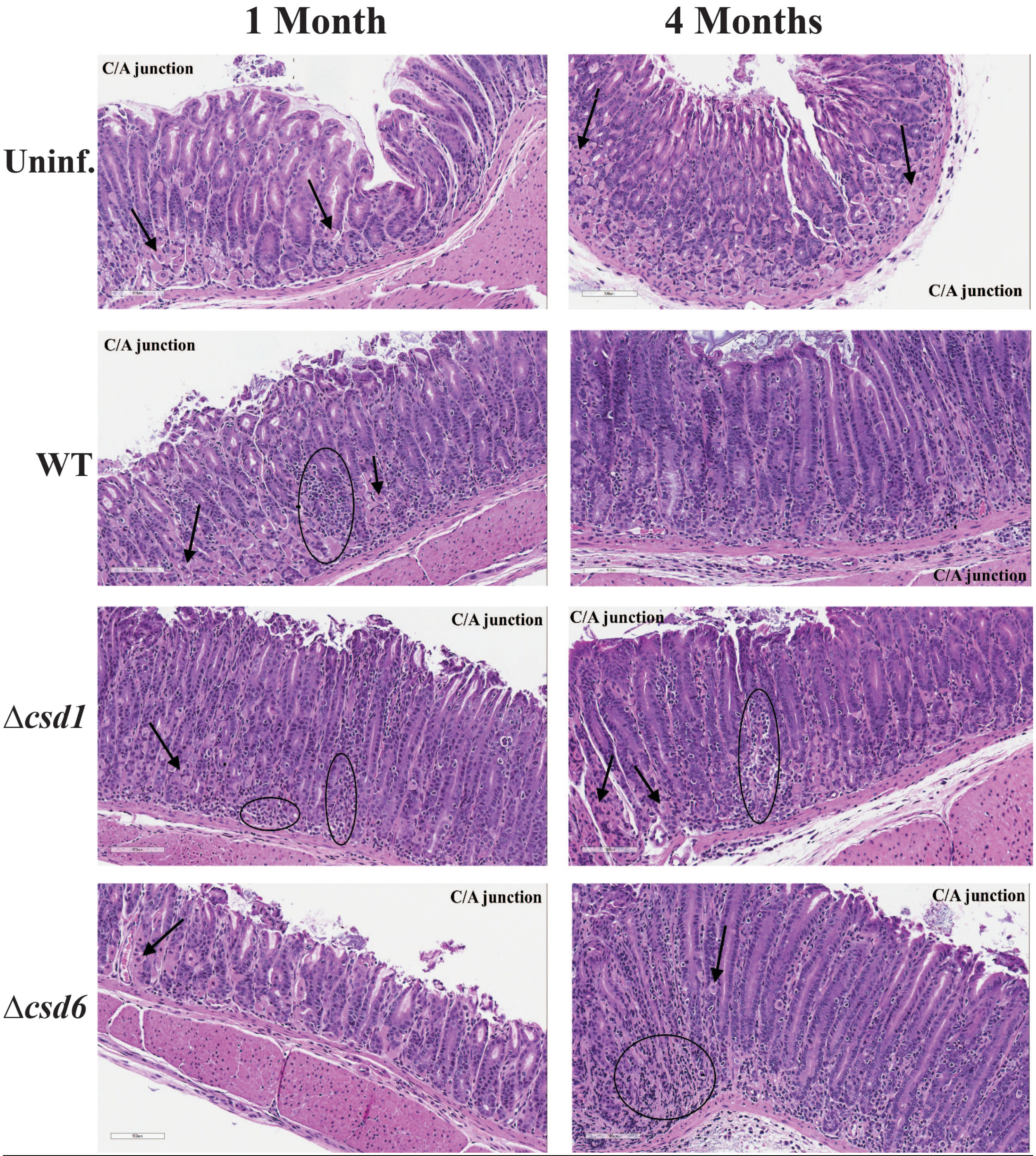

Figure 5.11. Representative images of chronically infected tissue samples examined for pathology (1 and 4 months). Shown are H&E stained images of the corpus/antral junction of each: uninfected, wild-type, Δ*csd1,* and Δ*csd6*-infected samples at 1 and 4 months. Inflammation and hyperplasia was observed at the corpus/antral junction of mice infected with wild-type or Δ*csd1* (1 and 4 months). The Δ*csd6*-infected sample does not show signs of inflammation or

hyperplasia after a month, and the glands show unperturbed gland length. At 4 months, the Δ*csd6*-infected sample shows similar inflammation and hyperplasia as wild-type, and shows increased gland length (2X normal length). The arrows point to parietal cells in corpus glands, and the circles show examples of sites where infiltrating immune cells are observed. Scale bar = 100 μm (white).

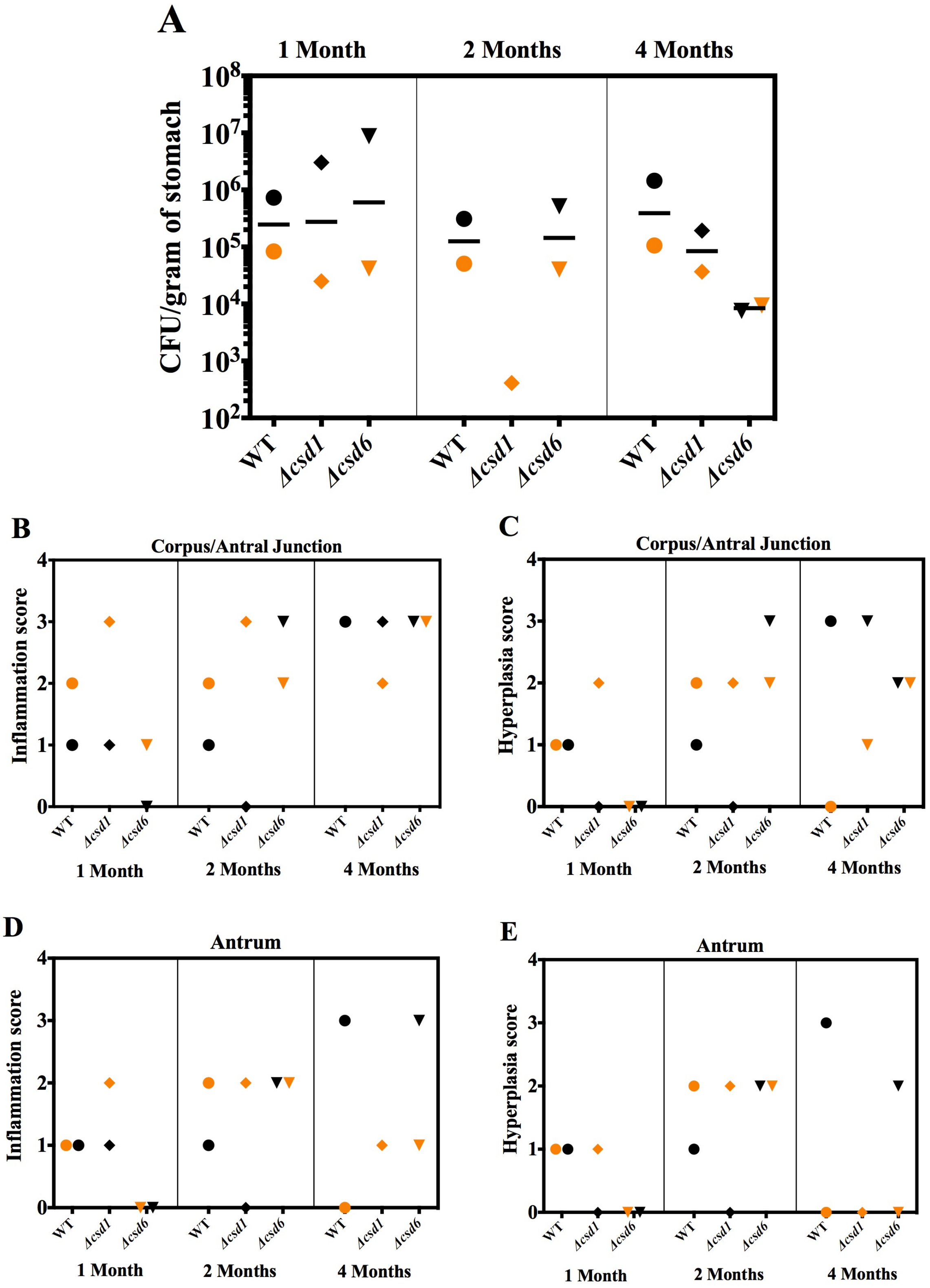
A
1 Month
2 Months
4 Months
CFU/gram of stomach
10^8
10^7
10^6
10^5
10^4
10^3
10^2
WT
Δcsd1
Δcsd6
B
Corpus/Antral Junction
Inflammation score
C
Corpus/Antral Junction
Hyperplasia score
D
Antrum
Inflammation score
E
Antrum
Hyperplasia score
0
1
2
3
4

Figure 5.12. Cell shape mutants show altered hyperplasia and chronic inflammation to wild-type at the corpus/antral junction and antrum. (A) CFU/gram of stomach loads for the two mice evaluated for histology per infected-group (wild-type, Δ*csd1*, and Δ*csd6*). The different colored symbols serve to distinguish which mouse produced the inflammation and hyperplasia scores shown in B-E (mouse 1 (orange symbol) and mouse 2 (black symbol)). Mouse 2 cleared Δ*csd1* at 2 months, and does not show inflammation or hyperplasia at either site (B-E). At 4 months, the wild-type infected sample in panel A (mouse 1, orange) had a focal lymphoid follicle at the corpus/antral junction and an inflammation score was not provided. Pathology scores at the antrum were not provided for Δ*csd1*-infected mouse 2 (black) at 4 months because of an incomplete antral section. The inflammation and hyperplasia scoring system (scale, 0 – 4) is described in the main text and in Table 5.4. The pathologic scoring system was adapted from Rogers *et al*., 2005 and Houghton (2012).

Chapter 6

Conclusions and Future Directions

It has long been hypothesized that helical cell shape facilitates *H. pylori*'s ability to penetrate the thick gastric mucus layer by enhancing cell body propulsion, thus enhancing colonization of the stomach. The goals of my dissertation research were to 1) to characterize the effect of cell shape on *H. pylori's* motility in physiologically relevant concentrations of purified gastric mucin (PGM) *in vitro*, and 2) to investigate how helical cell morphology impacts *H. pylori*'s niche acquisition *in vivo*.

Chapter 2 addressed the first goal with motility analysis of isogenic straight rod mutants in purified gastric mucin solutions that model the inner and outer mucus layers of the stomach. Loss of helical cell shape alters *H. pylori's* swimming speed in viscous media and its ability to escape from a mucin gel. Chapter 3 summarizes the contribution of flagellar number variation on *H. pylori's* swimming speed in viscous PGM solutions. Increasing flagellum number promotes faster swimming speeds in *H. pylori*. Thus, *H. pylori* strains may compensate for suboptimal helical parameters by increasing the number of flagella.

Chapter 4 describes a mathematical model that incorporates both the different cell shape parameters and flagellum number of each wild-type strain to predict *H. pylori* swimming speed. Our model partly explains the swimming speed differences observed between wild-type strains but requires further modifications. A model that incorporates both the diverse cell body geometries of *H. pylori* and experimental motor torque measurements of the different strains may provide insight on additional swimming dynamics not examined by our assay. *H. pylori's* cell body propulsion, flagellar motor torque, and flagella bundling dynamics remain unknown. These highly coordinated events may be examined experimentally. Recent studies used optical trapping and 3D-holographic microscopy to investigate the propulsive effects of bundling flagella for individual *E. coli* cells for extended periods of time and at fast acquisition rates (Bianchi *et al*., 2015). Optical trapping may serve a tool for characterizing *H. pylori*'s cell body propulsion and flagellar swimming dynamics in viscous PGM media.

My results show that *H. pylori* strains vary cell shape and flagellum number to maintain robust motility in viscous environments. We hypothesized that helical cell shape enhances *H. pylori's* propulsion through mucus to access specific niches within the stomach and to promote penetration of gastric glands. Chapter 5 investigates how the subtle differences in swimming speed observed between wild-type and straight rods *in vitro* impact gastric gland colonization *in vivo* using confocal microscopy and a 3D-imaging system.

Our *in vivo* studies reveal that cell shape mutants are significantly attenuated during initial colonization, but persist in the stomach after 1-4 months of infection in a subset of mice. Wild-type bacteria and straight rods show similar low-level colonization of both corpus and antral glands one day after infection. After a week of infection, the antral gland population shows marked expansion during wild-type infection, while the Δ*csd6* mutant maintains low level of colonization as observed at one day. Despite the diminished ability to acquire a niche within antral glands, straight rods persist and colonize both the corpus and antrum at 4 months of infection, with slightly higher loads at the corpus. Thus, helical cell shape perturbation alters the ability of *H. pylori* to utilize some of the available niches within the stomach. How *H. pylori* utilizes these niches to sustain chronic infection remains unknown. Before addressing this, we need to first address the discrepancies in the bacterial load quantified by our volumetric analysis and by CFU/gram of stomach load, which may reflect the population of bacteria localized at the surface mucus. Using the fixation methods described in Chapter 5, future studies will characterize the fraction of *H. pylori* within the surface mucus overlying the gastric epithelium to determine whether cell shape impacts this population in addition to the gland population.

Recently, Sigal *et al*. showed that *H. pylori* may colonize the progenitor and stem cell compartments of human or mouse gastric glands after a few weeks of infection, thus inducing gland hyperplasia (Sigal *et al*., 2015). Antral gland compartments can provide additional support for *H. pylori* growth and survival. If our cell shape mutants cannot access these compartments, they may not be able to induce damage or local gland hyperplasia. To address this, we will examine *H. pylori's* localization within different gland compartments.

Our pilot studies reveal that both wild-type and cell shape mutants show variable and bimodal spreads in mouse stomach colonization loads after a month of infection. We repeated this experiment by conducting single strain infections with wild-type and the straight rod mutant using a larger group of mice (15), and obtained comparable results. A subset of mice showed increased bacteria loads that were 1 or 2 logs higher than their geometric mean; a subset of mice showed lower colonization loads below their geometric mean; and in some cases mice cleared the bacteria. Addressing the spatial localization of bacteria within the stomach of mice that show varying stomach colonization loads will help address 1) how load impacts the gland population over time and 2) whether regional localization of bacteria impacts regional pathology to cause disease in the stomach.

The degree of inflammation found at the corpus/antral junction is often greater than seen in the adjacent mucosa of either the antrum or corpus after chronic infection, and may result in glandular atrophy and loss of corpus parietal cells, followed by mucous cell gland hyperplasia (Goldenring and Nomura, 2006). This phenotypic antralization of the corpus is described as spasmolytic polypeptide-expressing metaplasia (SPEM) and is characterized by the presence of trefoil factor 2 (TFF2, spasmolytic polypeptide) in antral glands (Goldenring and Nomura, 2006). To address how the regional localization of bacteria at the corpus/antral junction or antrum impacts pathology, we will evaluate the histology of mouse samples that show varying colonization loads after 3 and 4 months of infection, and stain for early metaplasia markers (i.e. TFF2) by immunohistochemistry.

Innate and adaptive immune responses are required for control of *H. pylori* infection and this includes neutrophils and lymphocyte infiltrates, and macrophages and plasma cells also infiltrate into the mucosa (Nakajima *et al.*, 2004; Necchi *et al.*, 2009; Caruso *et al.*, 2011). In particular, $CD4^+$ T-helper 1 (Th1) and Th17-polarized T-effector cell subsets, and their secreted cytokines, help control *H. pylori* infection (Sayi *et al.*, 2009; Velin *et al.*, 2009). Similarly, in a mouse model of *H. pylori* infection, an influx of neutrophils, mononuclear cells, CD4+ Th-1 cells and Th17 subsets, and B-cells are observed in the mucosa (Algood and Cover, 2006). In addition, *H. pylori* strains express VacA, a virulence factor that has been shown to suppress T-cell responses to mediate longevity of infection (Boncristiano *et al.*, 2003; Gebert *et al.*, 2003; and Sundrud *et al.*, 2004). To address the nature of the host immune response after long-term residence of wild-type bacteria or the cell shape mutants, we plan to examine different infiltrating immune cells (neutrophils, macrophages, T-cells, and B-cells) after a month of infection, where we observed differences in inflammation at the corpus/antral junction and antrum of wild-type-infected samples and of Δ*csd1* and Δ*csd6*-infected samples. It would also be important to determine whether cell shape mutants have unexpected effects on the expression of other factors that could mediate or suppress inflammation, such as VacA, in order for *H. pylori* to maintain a favorable niche in the stomach.

Unpublished work in our lab reveals that *H. pylori* clonal isolates cultured from gastric biopsies taken from a patient at different times and from different regions of the stomach, show diverse and distinct cell shapes to the *H. pylori* strain that originally infected the individual (J99). Although this clinical *H. pylori* strain shows more curved rod morphologies as compared to other helical *H. pylori* strains in nature, some gastric biopsy isolates show increased curvature (isolated from the antrum), and other isolates show decreased curvature and/or loss of helical cell shape (isolated from the corpus or antrum). The strains with straight rod morphology had frame shift mutations in genes *csd4* or *csd6*. These findings are very interesting because they suggest that even in a natural setting of *H. pylori* infection in humans, cell shape may be favored at different times of infection and within different locations of the stomach. Our preliminary analysis of bacteria harvested after 4 months of infection, reveals cell shape changes in some clones recovered from Δ*csd1*-infected mice. The Δ*csd1* mutant shows a broad distribution of cell shapes that vary in “c”-shaped, curved, helical, and straight rod morphology. In particular, one of 8 clones recovered from a mouse infected for 4 months shows straight rod morphology. We hypothesize that mutation in shape genes may accumulate due to genetic drift. Other factors that regulate the shape generation program in *H. pylori*, for example, may have fitness costs during chronic infection. We can address this by sequencing known cell shape determining genes in clones we recovered for wild-type and cell shape mutants after chronic infection.

This dissertation work provides insight on how helical cell shape and flagellum number variation impacts *H. pylori's* motility in different viscous environments, and how helical shape impacts *H. pylori's* niche acquisition in the stomach. Helical cell shape promotes *H. pylori's* motility and acquisition of multiple niches within the stomach. Understanding of how *H. pylori* establishes a niche in the stomach can provide further insight on the mechanisms through which *H. pylori* induces damage and maintains long-term colonization of the gastric niche.

BIBLIOGRAPHY

Akada, J.K., Ogura, K., Dailidiene, D., Dailide, G., Cheverud, J.M. and Berg, D.E. (2003). *Helicobacter pylori* tissue tropism: mouse-colonizing strains can target different gastric niches. *Microbiology* 149(Pt 7): 1901-9.

Algood, H.M.S. and Cover, T.L. (2006). *Helicobacter pylori* persistence: an Overview of Interactions between *H. pylori* and Host Immune Defenses. *Clin. Microbiol. Rev*. 19(4): 597-613.

Allen, A. and Garner A. (1980). Mucus and bicarbonate secretion in the stomach and their possible role in mucosal protection. *Gut* 21(3): 249–62.

Allen, A. (1981). Structure and function of gastrointestinal mucus. In: Johnson, L.R. editor. *Physiology of the Gastrointestinal Tract*. New York: Raven Press. p. 617–39.

Allen, A., Flemstrom, G., Garner, A. and Kivilaakso, E. (1993). Gastroduodenal mucosal protection. *Physiol. Rev.* 73(4): 823–57.

Alm R.A., Ling, L.S., Moir, D.T. *et al.* (1999). Genomic-sequence comparison of two unrelated isolates of the human gastric pathogen *Helicobacter pylori*. *Nature* 397(6715): 176–180.

Amieva, M.R., Salama, N.R., Tompkins, L.S. and Falkow, S. (2002). *Helicobacter pylori* enter and survive within multivesicular vacuoles of epithelial cells. *Cell Microbiol.* 4(10): 677-90.

Amieva, M.R., Vogelmann, R., Covacci, A., Tompkins, L.S., Nelson, W.J. and Falkow, S. (2003). Disruption of the epithelial apical-junctional complex by *Helicobacter pylori* CagA. *Science* 300(5624): 1430-4.

Arnold, I.C., Lee, J.Y., Amieva, M.R., Roers, A., Flavell, R.A., Sparwasser, T. and Muller, A. (2011). Tolerance rather than immunity protects from *Helicobacter pylori*-induced gastric preneoplasia. *Gastroenterology* 140(1): 199-209.

Asakura, H., Churin, Y., Bauer, B., Boettcher, J.P., Bartfeld, S., Hashii, N., Kawasaki, N., Mollenkopf, H.J., Jungblut, P.R., Brinkmann, V. and Meyer, T.F. (2010). *Helicobacter pylori* HP0518 affects flagellin glycosylation to alter bacterial motility. *Mol. Microbiol.* 78(5): 1130-1144.

Ashton-Key, M., Diss, T.C. and Isaacson, P.G. (1996). Detection of *Helicobacter pylori* in gastric biopsy and resection specimens. *J. Clin. Pathol*. 49(2): 107–11.

Backert, S., Clyne, M. and Tegtmeyer, N. (2011). Molecular mechanisms of gastric epithelial cell adhesion and infection of CagA by *Helicobacter pylori. Cell Communication and Signaling* 9: 28 (1-11).

Bagnoli, F., Buti, L., Tompkins, L., Covacci, A. and Amieva, M.R. (2005). *Helicobacter pylori* CagA induces a transition from polarized to invasive phenotypes in MDCK cells. *Proc. Natl. Acad. Sci.* USA 102(45): 16339-44.

Bell, A.E., Allen, A., Morris, E.R. and Ross-Murphy, S.B. (1984). Functional interactions of gastric mucus glycoprotein. *Int. J. Biol. Macromolec*. 6: 309–325.

Bell, A.E., Sellers, L.A., Allen, A., Cunliffe, W.J., Morris, E.R. and Ross-Murphy, S.B. (1985). Properties of gastric and duodenal mucus: effect of proteolysis, disulfide reduction, bile, acid, ethanol, and hypertonicity on mucus gel structure. *Gastroenterology* 88(1 Pt 2): 269–280.

Baltrus, D.A., Amieva, M.R., Covacci, A., Lowe, T.M., Merrell, D.S., Ottemann, K.M., Stein, M., Salama, N.R. and Guillemin, K. (2009). The complete genome sequence of *Helicobacter pylori* strain G27. *J. Bacteriol.* 191(1): 447-448.

Bansil, R., Celli, J.P., Hardcastle, J.M. and Turner, B.S. (2013). The Influence of Mucus Microstructure and Rheology in *Helicobacter pylori* Infection. *Front. Immunol.* 4: 310.

Bumann, D. (2015). Heterogeneous Host-Pathogen Encounters: Act Locally, Think Globally. *Cell Host & Microbe* 17(1): 13-19.

Blaser, M.J. and Berg, D.E. (2001). *Helicobacter pylori* genetic diversity and risk of human disease. *J. Clin. Invest.* 107(7): 767-73.

Blaser, M.J. and Atherton, J.C. (2004). *Helicobacter pylori* persistence: biology and disease. *J. Clin. Invest.* 113(3): 321-33.

Berg, H.C. and Turner, L. (1979). Movement of microorganisms in viscous environments. *Nature* 278(5702): 349-351.

Bianchi, S., Saglimbeni, F., Lepore, A. and Di Leonardo, R. (2015). Polar features in the flagellar propulsion of *E. coli* bacteria. *Phys. Rev. E. Stat Nonlin. Soft Matter Phys.* 91(6): 062705.

Boncristiano, M., Paccani, S.R., Barone, S., Ulivieri, C., Patrussi, L., Ilver, D., A. Amedei, A., D'Elios, M.M., Telford, J.L. and Baldari, C.T. (2003). The *Helicobacter pylori* vacuolating toxin inhibits T cell activation by two independent mechanisms. *J. Exp. Med.* 198(12): 1887-1897.

Bonis, M., Ecobichon, C., Guadagnini, S., Prevost, M.C. and Boneca, I.G. (2010). A M23B family metallopeptidase of *Helicobacter pylori* required for cell shape, pole formation and virulence. *Mol. Microbiol.* 78(4): 809-819.

Bronsdon, M.A. and Schoenknecht, F.D. (1988). *Campylobacter pylori* isolated from the stomach of the monkey *Macaca nemestrina. J. Clin. Microbiol.* 26(9): 1725–1728.

Bubendorfer, S., Koltai, M., Rossmann, F., Sourjik, V. and Thormann, K.M. (2014). Secondary bacterial flagellar system improves bacterial spreading by increasing the directional persistence of swimming. *Proc. Natl. Acad. Sci.* USA 111(31): 11485-11490.

Cabeen, M.T. and Jacobs-Wagner, C. (2005). Bacterial cell shape. *Nat. Rev. Microbiol.* 3(8): 601-610.

Caldara, M., Friedlander, R.S., Kavanaugh, N.L., Aizenberg, J., Foster, K.R. and Ribbeck, K. (2012). Mucin biopolymers prevent bacterial aggregation by retaining cells in the free-swimming state. *Curr. Biol.* 22(24): 2325-2330.

Calore, F., Genisset, C., Casellato, A., Rossatto, M., Cadolo, G., Esposti, M.D., Scorrano, L. and de Bernard, M. (2010). Endosome-mitochondria juxtaposition during apoptosis induced by *H. pylori* VacA. *Cell Death Differ.* 17(11): 1707-16.

Caruso, R.A., Parisi, A., Crisafulli, C., Bonanno, A., Lucian, R., Branca, G., Scardigno, M. and Fedele, F. (2011). Intraepithelial infiltration by mast cells in human *Helicobacter pylori* active gastritis. *Ultrastruct. Pathol.* 35(6): 251-5.

Celli, J., Gregor, B., Turner, B., Afdhal, N.H., Bansil, R. and Erramilli, S. (2005). Viscoelastic properties and dynamics of porcine gastric mucin. *Biomacromolecules* 6(3): 1329-1333.

Celli, J.P., Turner, B.S., Afdhal, N.H., Ewoldt, R.H., McKinley, G.H., Bansil, R. and Erramilli, S. (2007). Rheology of gastric mucin exhibits a pH-dependent sol-gel transition. *Biomacromolecules* 8(5): 1580-1586.

Celli, J.P., Turner, B.S., Afdhal, N.H., Keates, S., Ghiran, I., Kelly, C.P., Ewoldt, R.H., McKinley, G.H., So, P., Erramilli, S. and Bansil, R. (2009) *Helicobacter pylori* moves through mucus by reducing mucin viscoelasticity. *Proc. Natl. Acad. Sci.* USA 106(34): 14321-14326.

Censini, S., Lange, C., Xiang, Z. *et al*. (1996). Cag, a pathogenicity island of *Helicobacter* *pylori*, encodes type I-specific and disease-associated virulence factors. *Proc. Natl. Acad. Sci.* USA 93(25): 14648–14653.

Charon, N.W., Cockburn, A., Li, C., Liu, J., Miller, K.A., Miller, M.R., Motaleb, M.A. and Wolgemuth, C.W. (2012). The unique paradigm of spirochete motility and chemotaxis. *Annu. Rev. Microbiol.* 66: 349-370.

Chey, W.D. and Wong, B.C. (2007). American College of Gastroenterology guideline on the management of *Helicobacter pylori* infection. *Am. J. Gastroenterol.* 102(8): 1808-25.

Chu, Y.T., Wang, Y.H., Wu J.J. and Lei, H.Y. (2010). Invasion and multiplication of *Helicobacter pylori* in gastric epithelial cells and implications for antibiotic resistance. *Infect. Immun*. 78(10): 4157-4165.

Cicuta, P. and Donald, A.M. (2007). Microrheology: a review of the method and applications. *Soft Matter* 3: 1449-1455.

Cortez, R., Fauci, L. and Medovikov, A. (2005). The method of regularized Stokeslets in three dimensions: Analysis, validation, and application to helical swimming. *Physics of Fluids* 17: 031504.

Cover, T.L. and Blanke, S.R. (2005). *Helicobacter pylori* VacA, a paradigm for toxin multifunctionality. *Nat. Rev. Microbiol.* 3(4): 320-32.

Cover, T.L. (2016). *Helicobacter pylori* Diversity and Gastric Cancer Risk. *MBio*. 7(1): e01869-15.

Darnton, N.C., Turner, L., Rojevsky, S. and Berg, H.C. (2007). On torque and tumbling in swimming *Escherichia coli*. *J. Bacteriol.* 189(5): 1756-1764.

Day, A.S., Jones, N.L, Policova, Z., Jennings, H.A., Yau, E.K., Shannon, P., Neumann A.W., Sherman, P.M. (2001). Characterization of virulence factors of mouse-adapted *Helicobacter pylori* strain SS1 and effects on gastric hydrophobicity. *Dig. Dis. Sci.* 46(9): 1943-51.

Desai, H.G., Gill, H.H., Shankaran, K., Mehta, P.R. and Prabhu, S.R. (1991). Dental plaque: a permanent reservoir of *Helicobacter pylori*? *Scand. J. Gastroenterol*. 26(11): 1205-8.

Dey, A., Yokota, K., Kosavashi, K., Oguma, K., Hirai, Y. and Akagi, T. (1998). Antibody and cytokine responses in *Helicobacter pylori-infected* various mouse strains. *Acta Medica Okayama* 52(1): 41–48.

Dombrowski, C., Kan, W., Motaleb, M.A., Charon, N.W., Goldstein, R.E. and Wolgemuth, C.W. (2009). The elastic basis for the shape of *Borrelia burgdorferi*. *Biophys. J*. 96(11): 4409-4417.

Duan, Q., Zhou, M., Zhu, L. and Zhu, G. (2013). Flagella and bacterial pathogenicity. *J. Basic Microbiol.* 53(1): 1-8.

Dubois, A., Berg, D., Incecik, E., Fiala, N., Heman-Ackah, L., Yang, M., Wirth, H., Perez-Perez, G.I. and Blaser, M.J. (1999). Host specificity of *Helicobacter pylori* strains and host responses in experimentally challenged nonhuman primates. *Gastroenterology* 116(1): 90–96.

Dusenbery, D.B. (1998). Fitness landscapes for effects of shape on chemotaxis and other behaviors of bacteria. *J. Bacteriol*. 180(22): 5978-5983.

Eaton, K.A., Brooks, C.L., Morgan, D.R. and Krakowka, S. (1991). Essential role of urease in pathogenesis of gastritis induced by *Helicobacter pylori* in gnotobiotic piglets. *Infect. Immun*. 59(7): 2470-2475.

Eaton, K.A. and Krakowka, S. (1994). Effect of gastric pH on urease-dependent colonization of gnotobiotic piglets by *Helicobacter pylori. Infect. Immun.* 62(9): 3604-7.

Eaton, K.A., Suerbaum, S., Josenhans, C. and Krakowka, S. (1996). Colonization of gnotobiotic piglets by *Helicobacter pylori* deficient in two flagellin genes. *Infect. Immun.* 64(7): 2445-2448.

Eberle, J.A-M., Richter, P., Widmayer, P., Chubanov, V., Gudermann, T., and Breer, H. (2013). Band-like arrangement of taste-like sensory cells at the gastric groove: evidence for paracrine communication. *Front. Physiol*. 4(58): 1-10.

Earle, K.A, Billings, G., Sigal, M., Lichtman, J.S., Hansson, G.C., Elias, J.E., Amieva, M.R., Huang, K.C. and Sonnenburg, J.L. (2015). Quantitative Imaging of Gut Microbiota Spatial Organization. *Cell Host Microbe*. 18(4): 478-88.

Ertem, D. (2013). Clinical practice: *Helicobacter pylori* infection in childhood. *Eur. J. Pediatr*. 172(11): 1427-34.

Ferlay, J., Soerjomataram, I., Ervik, M., Dikshit, R., Eser, S., Mathers, C., Rebelo, M., Parkin, D.M., Forman, D. and Bray, F. (2013). Cancer Incidence and Mortality Worldwide: IARC CancerBase No. 11 [Internet]. Lyon, International Agency for Research on Cancer.

Ferrero, R.L. and Lee, A. (1988). Motility of *Campylobacter jejuni* in a viscous environment: comparison with conventional rod-shaped bacteria. *J. Gen. Microbiol.* 134(1): 53-59.

Ferrero, R.L., Thiberge, J.M., Huerre, M. and Labigne, A. (1998). Immune responses of specific-pathogen-free mice to chronic *Helicobacter pylori* (strain SS1) infection. *Infect. Immun.* 66(4): 1349-55.

Fox, J.G., Perkins, S., Yan, L., Shen, Z., Attardo, L. and Pappo, J. (1996). Local immune response in *Helicobacter pylori-infected* cats and identification of *H. pylori* in saliva, gastric fluid and faeces. *Immunol.* 88(3): 400–406.

Frirdich, E., Vermeulen, J., Biboy, J., Soares, F., Taveirne, M.E., Johnson, J.G., DiRita, V.J., Girardin, S.E., Vollmer, W. and Gaynor, E.C. (2014). Peptidoglycan LD-carboxypeptidase Pgp2 influences *Campylobacter jejuni* helical cell shape and pathogenic properties and provides the substrate for the DL-carboxypeptidase Pgp1. *J. Biol. Chem.* 289(12): 8007-8018.

García, A., Salas-Jara, M.J., Herrera, C. and González, C. (2014). Biofilm and *Helicobacter pylori*: from environment to human host. *World J. Gastroenterol*. 20(19): 5632-5638.

Gauthier, N.C., Monzo, P., Gonzalez, T., Doye, A., Oldani, A., Gounon, P., Ricci, V., Cormont, M. and Boquet, P. (2007). Early endosomes associated with dynamic F-actin structures are required for late trafficking of *H. pylori* VacA toxin. *J. Cell Biol.* 177(2): 343-54.

Georgiades, P., Pudney, P.D., Thornton, D.J. and Waigh, T.A. (2014). Particle tracking microrheology of purified gastrointestinal mucins. *Biopolymers* 101(4): 366-377.

Gebert, B., Fischer, W., Weiss, E., Hoffmann, R. and Haas, R. (2003) *Helicobacter pylori* vacuolating cytotoxin inhibits T lymphocyte activation. *Science* 301(5636): 1099-1102.

Genta, R.M., Robason, G.O. and Graham, D.Y. (1994). Simultaneous visualisation of *Helicobacter pylori* and gastric morphology: a new stain. *Hum. Pathol.* 25(3): 221–6.

Gerhard, M., Lehn, N., Neumayer, N., Borén, T., Rad, R., Schepp, W., Miehlke, S., Classen, M. and Prinz, C. (1999). Clinical relevance of the *Helicobacter pylori* gene for blood-group antigen-binding adhesin. *Proc. Natl. Acad. Sci.* USA. 96(22): 12778–12783.

Goldenring, J.R. and Nomura, S. (2006). Differentiation of the gastric mucosa III. Animal models of oxyntic atrophy and metaplasia. *Am. J. Physiol. Gastrointest. Liver Physiol*. 291(6): G999-1004.

Gray, J. and Hancock, G.J. (1955). The propulsion of sea urchin spermatozoa. *J. Exp. Biol.* 32: 802–814.

Greenberg, E.P. and Canale-Parola, E. (1977a). Motility of flagellated bacteria in viscous environments. *J. Bacteriol.* 132(1): 356–358.

Greenberg, E.P. and Canale-Parola, E. (1977b). Relationship between cell coiling and motility of spirochetes in viscous environments. *J. Bacteriol.* 131(3): 960-969.

Hazell, S.L., Lee, A., Brady, L. and Hennessy, W. (1986). *Campylobacter pyloridis* and gastritis: association with intercellular spaces and adaptation to an environment of mucus as important factors in colonization of the gastric epithelium. *J. Infect. Dis.* 153(4): 658-663.

Hirayama, F., Takagi, S., Iwao, E. *et al*. (1999). Development of poorly differentiated adenocarcinoma and carcinoid due to long-term *Helicobacter pylori* colonization in Mongolian gerbils. *J. Gastroenterol.* 34(4): 450–454.

Houghton, J.M. (ed.) (2012). *Helicobacter Species: Methods and Protocols*, Methods in Molecular Biology, vol. 921, DOI 10.1007/978-1-62703-005-2_22, © Springer Science + Business Media.

Howitt, M.R., Lee, J.Y., Lertsethtakarn, P., Vogelmann, R., Joubert, L.M., Ottemann, K.M. and Amieva, M.R. (2011). ChePep controls *Helicobacter pylori* Infection of the gastric glands and chemotaxis in the Epsilonproteobacteria. *MBio* 2:e00098-11.

Hyon, Y., Marcos, T.R., Powers, T.R., Stocker, R. and Fu, H.C. (2012). The wiggling trajectories of bacteria. *Journal of Fluid Mechanics* 705: 58-76.

IARC Working Group on the Evaluation of Carcinogenic Risks to Humans (2012). Biological agents. Volume 100 B. A review of human carcinogens. IARC *Monogr. Eval. Carcinog. Risks Hum*. 100: 1-441.

Ilver, D., Arnqvist, A., Ogren, J., Frick, I.M., Kersulyte, D., Incecik, E.T., Berg, D.E., Covacci, A., Engstrand, L. and Boren. T. (1998). *Helicobacter pylori* adhesin binding fucosylated histo-blood group antigens revealed by retagging. *Science* 279(5349): 373–377.

Ikeno, T., Ota, H., Sugiyama, A., Ishida, K., Katsuyama, T., Genta, R.M. and Kawasaki, S. (1999). *Helicobacter pylori-induced* chronic active gastritis, intestinal metaplasia, and gastric ulcer in Mongolian gerbils. *Am. J. Pathol*. 154(3): 951–960.

Iwaki, H., Sugiyama, T. and Asaka, M. (1998). A modified McMullen's staining for *Helicobacter pylori*: a high contrast, visibly prominent method. *Helicobacter* 3(1): 45–8.

Johansson, M.E.V., Sjovall, H. and Hansson, G.C. (2013). The gastrointestinal mucus system in health and disease. *Nat. Rev. Gastroenterol. Hepatol.* 10(6): 352-361.

Kamradt, A.E., Greiner, M., Ghiara, P. and Kaufmann, S.H. (2000). *Helicobacter pylori* infection in wild-type and cytokine-deficient C57BL/6 and BALB/c mouse mutants. *Microbes Infect*. 2(6): 593–597.

Kanehl, P. and Ishikawa, T. (2014). Fluid mechanics of swimming bacteria with multiple flagella. *Phys. Rev. E. Stat. Nonlin. Soft Matter Phys*. 89(4): 042704.

Karim, Q.N., Logan, R.P., Puels, J., Karnholz, A. and Worku, M.L. (1998). Measurement of motility of *Helicobacter pylori*, *Campylobacter jejuni*, and *Escherichia coli* by real time computer tracking using the Hobson BacTracker. *J. Clin. Pathol.* 51(8): 623-628.

Karita, M., Kouchiyama, T., Okita, K. *et al*. (1991). New small animal model for human gastric *Helicobacter pylori* infection: success in both nude and euthymic mice. *Am. J. Gastroenterol.* 86(11): 1596–1603.

Karita, M., Li, Q., Cantero, D. *et al*. (1994). Establishment of a small animal model for human *Helicobacter pylori* infection using germ-free mouse. *Am. J. Gastroenterol.* 89(2): 208–213.

Kim, I.J. and Blanke, S.R. (2012). Remodeling the host environment: modulation of the gastric epithelium by the *Helicobacter pylori* vacuolating toxin (VacA). *Front. Cell Infect. Microbiol.* 2:37. doi: 10.3389.

Kivi, M., Johansson, A.L., Reilly, M. and Tindberg. Y. (2005). *Helicobacter pylori* status in family members as risk factors for infection in children. *Epidemiol. Infect.* 133(4): 645-52.

Krakowka, S., Morgan, D.R., Kraft, W.G. and Leunk, R.D. (1987). Establishment of gastric *Campylobacter pylori* infection in the neonatal gnotobiotic piglet. *Infect. Immun.* 55(11): 2789–2796.

Kusters, J.G., van Vliet, A.H. and Kuipers, E.J. (2006). Pathogenesis of *Helicobacter pylori* infection. *Clin. Microbiol. Rev.* 19(3): 449-90.

Kwok, T., Backert, S., Schwarz, H., Berger, J. and Meyer, T.F. (2002). Specific Entry of *Helicobacter pylori* into Cultured Gastric Epithelial Cells via a Zipper-Like Mechanism. *Infect. Immun.* 70(4): 2108-2120

Lacayo, C.I., Pincus, Z., VanDuijn, M.M., Wilson, C.A., Fletcher, D.A., Gertler, F.B., Mogilner, A. and Theriot, J.A. (2007). Emergence of large-scale cell morphology and movement from local actin filament growth dynamics. *PLoS Biol.* 5(9): e233.

Lambert, J.R., Borromeo, M., Pinkard, K.J., Turner, H., Chapman, C.B. and Smith, M.L. (1987). Colonization of gnotobiotic piglets with *Campylobacter Pyloridis—an* animal model? *J. Infect. Dis*. 155(6): 1344.

Langford, M.L., Zabaleta, J., Ochoa, A.C., Testerman, T.L. and McGee, D.J. (2006). *In vitro* and *in vivo* complementation of the *Helicobacter pylori* arginase mutant using an intergenic chromosomal site. *Helicobacter* 11(5): 477-93.

Lauga, E. and Powers, T.R. (2009). The hydrodynamics of swimming microorganisms. *Reports on Progress in Physics* 72: 096601.

Lee, A., O'Rourke, J., De Ungria, M.C., Robertson, B., Daskalopoulos, G. and Dixon, M.F. (1997). A standardized mouse model of *Helicobacter pylori* infection: introducing the Sydney strain. *Gastroenterology* 112(4): 1386-1397.

Li, G. and Tang, J.X. (2006). Low flagellar motor torque and high swimming efficiency of *Caulobacter crescentus* swarmer cells. *Biophys. J.* 91(7): 2726-2734.

Lieleg, O., Vladescu, I. and Ribbeck, K. (2010). Characterization of particle translocation through mucin hydrogels. *Biophys. J.* 98(9): 1782-1789.

Lighthill J (1976) Flagellar hydrodynamics - Neumann, JV Lecture, 1975. *SIAM Rev.* 18: 161–230.

Liu, B., Gulino, M., Morse, M., Tang, J.X., Powers, T.R. and Breuer, K.S. (2014). Helical motion of the cell body enhances *Caulobacter crescentus* motility. *Proc. Natl. Acad. Sci.* USA 111(31): 11252-11256.

Lowenthal, A.C., Hill, M., Sycuro, L.K., Mehmood, K., Salama, N.R. and Ottemann, K.M. (2009). Functional analysis of the *Helicobacter pylori* flagellar switch proteins. *J. Bacteriol.* 191(23): 7147-7156.

Luzza, F., Mancuso, M., Imeneo, M., Contaldo, A., Giancotti, L., Pensabene, L., Doldo, P., Liberto, M.C., Strisciuglio, P., Focà, A., Guandalini, S. and Pallone, F. (2000). Evidence favouring the gastro-oral route in the transmission of *Helicobacter pylori* infection in children. *Eur. J. Gastroenterol. Hepatol*. 12(6): 623-7.

Magariyama, Y., Sugiyama, S., Muramoto, K., Kawagishi, I., Imae, Y. and Kudo, S. (1995). Simultaneous measurement of bacterial flagellar rotation rate and swimming speed. *Biophys. J.* 69(5): 2154-2162.

Magariyama, Y. and Kudo, S. (2002). A mathematical explanation of an increase in bacterial swimming speed with viscosity in linear-polymer solutions. *Biophys. J.* 83(2): 733-9.

Marchetti, M., Arico, B., Burroni, D. *et al.* (1995) Development of a mouse model of *Helicobacter pylori* infection that mimics human disease. *Science* 267(5204): 1655–1658.

Martinez, V.A., Schwarz-Linek, J., Reufer, M., Wilson, L.G., Morozov, A.N. and Poon, W.C. (2014) Flagellated bacterial motility in polymer solutions. *Proc. Natl. Acad. Sci.* USA 111(50): 17771-17776.

Mears, P. (2014). Illuminating the relationship between flagellar activity and bacterial swimming (Doctoral dissertation, University of Illinois at Urbana-Champaign).

McClain, M.S., Shaffer, C.L., Israel, D.A., Peek, R.M. Jr. and Cover, T.L. (2009). Genome sequence analysis of *Helicobacter pylori* strains associated with gastric ulceration and gastric cancer. *BMC Genomics* 10: 3. doi: 10.1186/1471-2164-10-3.

Montecucco, C. and Rappuoli, R. (2001). Living dangerously: how *Helicobacter pylori* survives in the human stomach. *Nat. Rev. Mol. Cell Biol.* 2(6): 457-466.

Nakajima, S., Bamba, N. and Hattori, T. (2004). Histological aspects and role of mast cells in *Helicobacter-pylori*-infected gastritis. *Aliment. Pharmacol. Ther.* 20 Suppl. 1: 165-70.

Nakamura, H., Yoshiyama, H., Takeuchi, H., Mizote, T., Okita, K. and Nakazawa, T. (1998). Urease plays an important role in the chemotactic motility of *Helicobacter pylori* in a viscous environment. *Infect. Immun.* 66(10): 4832-4837.

Naughton, J.A., Marino, K., Dolan, B., Reid, C., Gough, R., Gallagher, M.E., Kilcoyne, M., Gerlach, J.Q., Joshi, L., Rudd, P., Carrington, S., Bourke, B. and Clyne, M. (2013). Divergent mechanisms of interaction of *Helicobacter pylori* and *Campylobacter jejuni* with mucus and mucins. *Infect. Immun.* 81(8): 2838-2850.

Necchi, V., Manca, R., Ricci, V. and Solcia, E. (2009). Evidence for transepithelial dendritic cells in human *H. pylori* active gastritis. *Helicobacter* 14(3): 208-22.

Noto, J.M., Lee, J.Y., Gaddy, J.A., Cover, T.L., Amieva, M.R. and Peek, R.M. Jr. (2015). Regulation of *Helicobacter pylori* Virulence Within the Context of Iron Deficiency. *J. Infect. Dis.* 211(11): 1790-1794.

Odenbreit, S., Püls, J., Sedlmaier, B., Gerland, E., Fischer, W. and Haas, R. (2000). Translocation of *Helicobacter pylori* CagA into gastric epithelial cells by type IV secretion. *Science* 287(5457): 1497-500.

Ogura, K., Maeda, S., Nakao, M. *et al.* (2000). Virulence factors of *Helicobacter pylori* responsible for gastric diseases in Mongolian gerbil. *J. Exp. Med.* 192(11): 1601–1610.

Olbermann, P., Josenhans, C., Moodley, Y., Uhr, M., Stamer, C., Vauterin, M., Suerbaum S., Achtman, M. and Linz, B. (2010). A global overview of the genetic and functional diversity in the *Helicobacter pylori* cag pathogenicity island. *PLoS Genet.* 6(8): e1001069. doi: 10.1371.

Ottemann, K.M. and Lowenthal, A.C. (2002). *Helicobacter pylori* uses motility for initial colonization and to attain robust infection. *Infect. Immun.* 70(4): 1984-1990.

Pearson, J., Allen, A. and Venables, C. (1980). Gastric mucus: isolation and polymeric structure of the undegraded glycoprotein: its breakdown by pepsin. *Gastroenterology* 78(4): 709–715.

Peek, R.M. Jr. and Blaser, M.J. (2002). *Helicobacter pylori* and gastrointestinal tract adenocarcinomas. *Nat. Rev. Cancer* 2(1): 28-37.

Peek, R.M., Jr. and Crabtree, J.E. (2006). *Helicobacter* infection and gastric neoplasia. *J. Pathol.* 208(2): 233-248.

Pincus, Z. and Theriot, J.A. (2007). Comparison of quantitative methods for cell-shape analysis. *J. Microsc.* 227(Pt 2): 140-156.

Poutahidis, T., Tsangaris, T., Kanakoudis, G., Vlemmas, I., Iliadis, N. and Sofianou, D. (2001). *Helicobacter pylori*-induced gastritis in experimentally infected conventional piglets. *Vet. Pathol.* 38(6): 667–678.

Puchtler, H., Waldrop, F.S., Meloan, S.N., Terry, M.S. and Conner, H.M. (1970). Methacarn (Methanol-Carnoy) Fixation: Practical and Theoretical Considerations. *Histochemie* 21(2): 97-116.

Rodenborn, B., Chen, C.H., Swinney, H.L., Liu, B. and Zhang, H.P. (2013). Propulsion of microorganisms by a helical flagellum. *Proc. Natl. Acad. Sci.* USA 110(5): E338-347.

Rogers, A.B., Taylor, N.S., Whary, M.T., Stefanich, E.D., Wang, T.C. and Fox, J.G. (2005). *Helicobacter pylori* but not high salt induces gastric intraepithelial neoplasia in B6129 mice. *Cancer Res.* 65(23): 10709-15.

Rogers, S.S., Waigh, T.A., Zhao, X. and Lu, J.R. (2007). Precise particle tracking against a complicated background: polynomial fitting with Gaussian weight. *Phys. Biol.* 4(3): 220-227.

Rolig, A.S., Shanks, J., Carter, J.E. and Ottemann, K.M. (2012). *Helicobacter pylori* requires TlpD-driven chemotaxis to proliferate in the antrum. *Infect. Immun.* 80(10): 3713-3720.

Rothenbacher, D., Inceoglu, J., Bode, G. and Brenner, H. (2000). Acquisition of *Helicobacter pylori* infection in a high-risk population occurs within the first 2 years of life. *J. Pediatr.* 136(6): 744-8.

Saadat, I., Higashi, H., Obuse, C., Umeda, M., Murata-Kamiya, N., Saito, Y., Lu, H., Ohnishi, N., Azuma, T., Suzuki, A., Ohno, S. and Hatakeyama M. (2007). *Helicobacter pylori* CagA targets PAR1/MARK kinase to disrupt epithelial cell polarity. *Nature* 447(7142): 330-3.

Sakagami, T., Dixon, M., O'Rourke, J., Howlett, R., Alderuccio, F., Vella, J., Shimoyama, T. and Lee, A. (1996). Atrophic gastric changes in both *Helicobacter felis* and *Helicobacter pylori* infected mice are host dependent and separate from antral gastritis. *Gut* 39(5): 639-48.

Salama, N.R., Shepherd, B. and Falkow, B. (2004) Global transposon mutagenesis and essential gene analysis of *Helicobacter pylori*. *J. Bacteriol.* 186(23): 7926-7935.

Sayi, A., Kohler, E., Hitzler, I., Arnold, I., Schwendener, R., Rehrauer, H. and Müller, A. (2009). The CD4+ T cell-mediated IFN-gamma response to *Helicobacter infection* is essential for clearance and determines gastric cancer risk. *J. Immunol.* 182(11): 7085-101.

Schneider, W.R. and Doetsch, R.N. (1974) Effect of viscosity on bacterial motility. *J. Bacteriol.* 117(2): 696–701.

Schrager, J. and Oates, M.D. (1974). The isolation and partial characterization of a glycoprotein isolated from human gastric aspirates and from extracts of gastric mucosae. *Biochim. Biophys. Acta* 372(1): 183–195.

Schreiber, S., Konradt, M., Groll, C., Scheid, P., Hanauer, G., Werling, H.O., Josenhans, C. and Suerbaum, S. (2004). The spatial orientation of *Helicobacter pylori* in the gastric mucus. *Proc. Natl. Acad. Sci.* USA 101(14): 5024-5029.

Schwarz, S., Morelli, G., Kusecek, B., Manica, A., Balloux, F., Owen, R.J., Graham, D.Y., van der Merwe, S., Achtman, M. and Suerbaum, S. (2008). Horizontal versus familial transmission of *Helicobacter pylori*. *PLoS Pathog*. 4(10): e1000180. doi: 10.1371.

Sellers, L.A., Allen, A., Morris, E.R. and Ross-Murphy, S.B. (1987). Mechanical characterization and properties of gastrointestinal mucus gel. *Biorheology* 24(6): 615-623.

Sharma, C.M., Hoffmann, S., Darfeuille, F., Reignier, J., Findeiss, S., Sittka, A., Chabas, S., Reiche, K., Hackermuller, J., Reinhardt, R., Stadler, P.F. and Vogel, J. (2010). The primary transcriptome of the major human pathogen *Helicobacter pylori*. *Nature* 464(7286): 250-255.

Shoesmith, J.G. (1960) The measurement of bacterial motility. *J. Gen. Microbiol.* 22: 528–535.

Sigal, M., Rothenberg, M.E., Logan, C.Y., Lee, J.Y., Honaker, R.W., Cooper, R.L., Passarelli, B., Camorlinga, M., Bouley, D.M., Alvarez, G., Nusse, R., Torres, J. and Amieva, M.R. (2015). *Helicobacter pylori* Activates and Expands Lgr5(+) Stem Cells Through Direct Colonization of the Gastric Glands. *Gastroenterology.* 148(7): 1392-404.e21.

Smith, L.E., Smallwood, R. and Macneil, S. (2010). A comparison of imaging methodologies for 3D tissue engineering. *Microsc. Res. Tech.* 73(12): 1123-33.

Son, K., Guasto, J.S. and Stocker, R.(2013). Bacteria can exploit a flagellar buckling instability to change direction. *Nature Physics* 9: 494-498.

Spagnolie, S.E., Liu, B. and Powers, T.R. (2013). Locomotion of helical bodies in viscoelastic fluids: enhanced swimming at large helical amplitudes. *Phys. Rev. Lett.* 111(6): 068101.

Stuurman, N., Edelstein, A., Amodaj, N., Hoover, K. and Vale, R. (2010). Computer control of microscopes using microManager. *Curr. Protoc. Mol. Biol.* Chapter 14: Unit 14.20.

Suerbaum, S. and Josenhans, C. (2007). *Helicobacter pylori* evolution and phenotypic diversification in a changing host. *Nat. Rev. Microbiol*. 5(6): 441-52.

Sundrud, M. S., Torres, V.J., Unutmaz, D. and Cover. T.L. (2004). Inhibition of primary human T cell proliferation by *Helicobacter pylori* vacuolating toxin (VacA) is independent of VacA effects on IL-2 secretion. *Proc. Natl. Acad. Sci.* USA. 101(20): 7727-7732.

Suzuki, M., Mimuro, H., Kiga, K., Fukumatsu, M., Ishijima, N., Morikawa, H., Nagai, S., Koyasu, S., Gilman, R.H., Kersulyte, D., Berg, D.E. and Sasakawa, C. (2009). *Helicobacter pylori* CagA phosphorylation-independent function in epithelial proliferation and inflammation. *Cell Host & Microbe* 5(1): 23-34.

Sycuro, L.K., Pincus, Z., Gutierrez, K.D., Biboy, J., Stern, C.A., Vollmer, W. and Salama, N.R. (2010). Peptidoglycan crosslinking relaxation promotes *Helicobacter pylori*'s helical shape and stomach colonization. *Cell* 141(5): 822-833.

Sycuro, L.K., Wyckoff, T.J., Biboy, J., Born, P., Pincus, Z., Vollmer, W. and Salama, N.R. (2012) Multiple peptidoglycan modification networks modulate *Helicobacter pylori's* cell shape, motility, and colonization potential. *PLoS Pathog.* 8(3): e1002603.

Sycuro, L.K., Rule, C.S., Petersen, T.W., Wyckoff, T.J., Sessler, T., Nagarkar, D.B., Khalid, F., Pincus, Z., Biboy, J., Vollmer, W. and Salama, N.R. (2013). Flow cytometry-based enrichment for cell shape mutants identifies multiple genes that influence *Helicobacter pylori* morphology. *Mol. Microbiol.* 90(4): 869-883.

Tam, C., LeDue, J., Mun, J.J., Herzmark, P., Robey, E.A., Evans, D.J. and Fleiszig, S.M. (2011). 3D quantitative imaging of unprocessed live tissue reveals epithelial defense against bacterial adhesion and subsequent traversal requires MyD88. *PLoS One* 6(8): e24008.

Tan, S., Tompkins, L.S. and Amieva, M.R. (2009). *Helicobacter pylori* usurps cell polarity to turn the cell surface into a replicative niche. *PLoS Pathog.* 5(5): e1000407.

Taylor, C., Allen, A., Dettmar, P.W. and Pearson, J.P. (2004) Two rheologically different gastric mucus secretions with different putative functions. *Biochim. Biophys. Acta.* 1674(2): 131-138.

Tegtmeyer, N., Wessler, S. and Backert. S. (2011). Role of the cag-pathogenicity island encoded type IV secretion system in *Helicobacter pylori*. *FEBS J.* 278(8): 1190-202.

Terebiznik, M.R., Raju, D., Vázquez, C.L., Torbricki, K., Kulkarni, R., Blanke, S.R., Yoshimori, T., Colombo, M.I. and Jones, N.L. (2009). Effect of *Helicobacter pylori's* vacuolating cytotoxin on the autophagy pathway in gastric epithelial cells. *Autophagy* 5(3): 370-9.

Terry, K., Williams, S.M., Connolly, L. and Ottemann, K.M. (2005). Chemotaxis plays multiple roles during *Helicobacter pylori* animal infection. *Infect. Immun.* 73(2): 803-811.

Thomas, J.E., Gibson, G.R., Darboe, M.K., Dale, A. and Weaver, L.T. (1992). Isolation of *Helicobacter pylori* from human faeces. *Lancet* 340(8829): 1194-5.

Thompson, L.J., Danon, S.J., Wilson, J.E., O'Rourke, J.L., Salama, N.R., Falkow, S., Mitchell, H. and Lee, A. (2004). Chronic *Helicobacter pylori* infection with Sydney strain 1 and a newly identified mouse-adapted strain (Sydney strain 2000) in C57BL/6 and BALB/c mice. *Infect Immun.* 72(8): 4668-79.

Tomb, J.F., White, O., Kerlavage, A.R. *et al*. (1997). The complete genome sequence of the gastric pathogen *Helicobacter pylori*. *Nature* 388(6642): 539–547.

Tsang, J. and Hoover, T.R. (2014). Requirement of the flagellar protein export apparatus component FliO for optimal expression of flagellar genes in *Helicobacter pylori*. *J. Bacteriol*. 196(15): 2709-2717.

Tsuda, M., Karita, M., Mizote, T., Morshed, M.G., Okita, K. and Nakazawa, T. (1994a). Essential role of *Helicobacter pylori* urease in gastric colonization: definite proof using a urease-negative mutant constructed by gene replacement. *Eur. J. Gastroenterol. Hepatol.* 6 Suppl 1: S49-52.

Tsuda, M., Karita, M., Morshed, M.G., Okita, K. and Nakazawa, T. (1994b). A urease-negative mutant of *Helicobacter pylori* constructed by allelic exchange mutagenesis lacks the ability to colonize the nude mouse stomach. *Infect. Immun.* 62(8): 3586-3589.

Tsugawa, H., Suzuki, H., Saya, H., Hatakeyama, M., Hirayama, T., Hirata, K., Nagano, O., Matsuzaki, J. and Hibi, T. (2012). Reactive oxygen species-induced autophagic degradation of *Helicobacter pylori* CagA is specifically suppressed in cancer stem-like cells. *Cell Host & Microbe.* 12(6): 764-77.

Urita, Y., Watanabe, T., Kawagoe, N., Takemoto, I., Tanaka, H., Kijima, S., Kido, H., Maeda, T., Sugasawa, Y., Miyazaki, T., Honda, Y., Nakanishi, K., Shimada, N., Nakajima, H., Sugimoto, M. and Urita, C. (2013). Role of infected grandmothers in transmission of *Helicobacter pylori* to children in a Japanese rural town. *J. Paediatr. Child Health* 49(5): 394-8.

van Doorn, N.E., Namavar, F., Sparrius, M., Stoof, J., van Rees, E.P., van Doorn, L.J. and Vandenbroucke-Grauls, C.M. (1999). *Helicobacter pylori*-associated gastritis in mice is host and strain specific. *Infect. Immun.* 67(6): 3040–3046.

Velin, D., Favre, L., Bernasconi, E., Bachmann, D., Pythoud, C., Saiji, E., Bouzourene, H. and Michetti, P. (2009). Interleukin-17 is a critical mediator of vaccine-induced reduction of *Helicobacter* infection in the mouse model. *Gastroentetrology* 136(7): 2237-2246.

Volocity: Improvision PE. (versions 2011 and 2013). Volocity 3D Rendering and Image Analyses Program. Versions 6.1 and 6.3.

Wang, Y., Roos, K.P. and Taylor, D.E. (1993). Transformation of *Helicobacter pylori* by chromosomal metronidazole resistance and by a plasmid with a selectable chloramphenicol resistance marker. *J. Gen. Microbiol.* 139(10): 2485-2493.

Weyermann, M., Rothenbacher, D. and Brenner, H. (2009). Acquisition of *Helicobacter pylori infection* in early childhood: independent contributions of infected mothers, fathers, and siblings. *Am. J. Gastroenterol.* 104(1): 182-9.

Willhite, D.C. and Blanke, S.R. (2004). *Helicobacter pylori* vacuolating cytotoxin enters cells, localizes to the mitochondria, and induces mitochondrial membrane permeability changes correlated to toxin channel activity. *Cell Microbiol.* 6(2): 143-54.

Worku, M.L., Sidebotham, R.L., Baron, J.H., Misiewicz, J.J., Logan, R.P., Keshavarz, T. and Karim, Q.N. (1999). Motility of *Helicobacter pylori* in a viscous environment. *Eur. J. Gastroenterol. Hepatol.* 11(10): 1143-1150.

Wroblewski, L.E. and Peek, R.M. Jr. (2013). *Helicobacter pylori* in gastric carcinogenesis: mechanisms. *Gastroenterol. Clin. North Am.* 42(2): 285-298.

Yamaoka, Y., Ojo, O., Fujimoto, S., Odenbreit, S., Haas, R., Gutierrez, O., El-Zimaity, H.M., Reddy, R., Arnqvist, A. and Graham, D.Y. (2006). *Helicobacter pylori* outer membrane proteins and gastroduodenal disease. *Gut* 55(6): 775–781.

Yeung, A.T., Parayno, A. and Hancock, R.E. (2012). Mucin promotes rapid surface motility in *Pseudomonas aeruginosa*. *MBio* 3(3). pii: e00073-12.

Yokota, K., Kurebayashi, Y., Takayama, Y., Hayashi, S., Isogai, H., Isogai, E., Imai, K., Yabana, T., Yachi, A. and Oguma, K. (1991). Colonization of *Helicobacter pylori* in the gastric tissue of Mongolian gerbils. *Microbiol. Immunol.* 35(6): 475–480.

Yoshiyama, H. and Nakazawa, T. (2000). Unique mechanism of *Helicobacter pylori* for colonizing the gastric mucus. *Microbes Infect.* 2(1): 55-60.

Yücel, O., Sayan, A. and Yildiz, M. (2009). The factors associated with asymptomatic carriage of *Helicobacter pylori* in children and their mothers living in three socio-economic settings. *Jpn. J. Infect. Dis.* 62(2): 120-4.

Zheng, Q., Chen, X.Y., Shi, Y. *et al*. (2004). Development of gastric adenocarcinoma in Mongolian gerbils after long-term infection with *Helicobacter pylori. J. Gastroenterol. Hepatol.* 19(10): 1192–1198.

ACKNOWLEDGEMENTS II

I would like to thank Dr. Rama Bansil and Joseph H. Hardcastle for collaboration on the dissertation work that investigated the effect of cell shape and flagella number variation on *H. pylori's* motility, summarized in Chapters 2 and 3, and for the modeling work summarized in Chapter 4; Prof. Jonathan P. Celli for helpful discussions regarding his work on *H. pylori* motility in PGM; Dr. Bradley Turner for very helpful discussions regarding mucin and providing purified porcine gastric mucin; Drs. Timothy Hoover and Jennifer Tsang for providing the flagellar mutants and for helpful discussions on the studies presented in Chapters 2-4; Jeffrey Wang for help with bacterial tracking analysis; Dr. Zachary Pincus for helpful discussions on CellTool-based morphology analysis; Dr. Julio Vasquez, Dave McDonald, and Sharmon Knecht for help with bacterial tracking analysis, training on acquiring 3D-confocal images, and for discussions on Volocity 3D-image analysis at the FHCRC Scientific Imaging Core (Cancer Center Support Grant P30 CA015704-40); Sharmon Knecht, Bobbie Schneider, and Stephen MacFarlane (FHCRC Electron Microscopy Shared Resource) for assistance with TEM and SEM; Dr. Julie Randolph-Habecker, Sharon R. McLaughlin, Elizabeth Benitez-Martinez, Tracy A. Goodpaster, and Kimberley R. Melton at the FHCRC Experimental Histopathology Shared Resources for help with sample preparation for histology; Dr. Sue Knoblaugh, DVM, for help with pathologic evaluation (College of Veterinary Medicine at The Ohio State University and Cancer Support Grant – P30 CA016058); and Dr. Manuel R. Amieva and Julie Huang at Stanford University for advice and reagents for immunofluorescence of thick gastric sections, and bacterial quantitation analysis.

This project was supported by US National Institute of Health Grants RO1 AI094834 (N.R.S) and F31 AI098424 (L.E.M). The funders have no role in study design, data collection and interpretation, or the decision to submit the work for publication. The contents are solely the responsibilities of the authors and do not necessarily represent the official views of these funding agencies.

VITA

Laura Elizabeth Martínez was born in Compton and grew up in Boyle Heights, Los Angeles, California. In 1998, she graduated from Theodore Roosevelt Senior High School in Los Angeles. She received her Bachelor of Science in Organismic, Ecology, and Evolutionary Biology (OBEE) from the University of California, Los Angeles in 2003. Following her undergraduate studies, she received a post-baccalaureate fellowship from the San Diego State University and the University of California, San Diego. She conducted HIV-1 research at UC San Diego under the supervision of Drs. Douglas Richman and Celsa A. Spina. After her fellowship, she decided to pursue an advanced education and in 2006 she began a master's degree program at the California State University, Los Angeles. Laura's research was conducted in the laboratory of Dr. Sandra B. Sharp, where she specialized in Molecular Cell and Developmental Biology. In 2009, she began her graduate work at the University of Washington in the Pathobiology Graduate Program. Laura's dissertation research was conducted in the laboratory of Dr. Nina R. Salama at the Fred Hutchinson Cancer Research Center. She investigated how helical cell shape impacts *Helicobacter pylori's* motility and niche acquisition in the stomach. Laura received her Doctor of Philosophy in Pathobiology in 2016.